Simulation of Magnetic Phenomena at Realistic Interfaces

Dissertation by

Sergiy Grytsyuk

In Partial Fulfillment of the Requirements

For the Degree of

Doctor of Philosophy

King Abdullah University of Science and Technology, Thuwal,

Kingdom of Saudi Arabia

(January, 2016)

The dissertation of Sergiy Grytsyuk is approved by the examination committee

Committee Chairperson: Prof. Udo Schwingenschlögl

Committee Member: Prof. Aurelien Manchon

Committee Member: Prof. Jörg Eppinger

Committee Member: Prof. Alexander Chroneos

King Abdullah University of Science and Technology

2016

ABSTRACT

Simulation of Magnetic Phenomena at Realistic Interfaces

Sergiy Grytsyuk

In modern technology exciting developments are related to the ability to understand and control interfaces. Particularly, magnetic interfaces revealing spin-dependent electron transport are of great interest for modern spintronic devices, such as random access memories and logic devices. From the technological point of view, spintronic devices based on magnetic interfaces enable manipulation of the magnetism via an electric field. Such ability is a result of the different quantum effects arising from the magnetic interfaces (for example, spin transfer torque or spin-orbit torque) and it can reduce the energy consumption as compared to the traditional semiconductor electronic devices. Despite many appealing characteristics of these materials, fundamental understanding of their microscopic properties and related phenomena needs to be established by thorough investigation. In this work we implement first-principles calculations in order to study the structural, electric, and magnetic properties as well as related phenomena of two types of interfaces with large potential in spintronic applications: 1) interfaces between antiferromagnetic 3d-metal-oxides and ferromagnetic 3d-metals and 2) interfaces between non-magnetic 5d(4d)- and ferromagnetic 3d-metals. A major difficulty in studying such interfaces theoretically is the typically large lattice mismatch. By employing supercells with Moiré patterns, we

eliminate the artificial strain that leads to doubtful results and are able to describe the dependence of the atomic density at the interfaces on the component materials and their thicknesses.

After establishing understanding about the interface structures, we investigate the electronic and magnetic properties. A Moiré supercell with transition layer is found to reproduce the main experimental findings and thus turns out to be the appropriate model for simulating magnetic misfit interfaces. In addition, we systematically study the magnetic anisotropy and Rashba band splitting at non-magnetic 5d(4d)- and ferromagnetic 3d-metal interfaces and their dependences on aspects such as interdiffusion, surface oxidation, thin film thickness and lattice mismatch. We find that changes of structural details strongly alter the electronic states, which in turn influences the magnetic properties and phenomena related to spin-orbit coupling. Since the interfaces studied in this work have complex electronic structures, a computational approach has been developed in order to estimate the strength of the Rashba band splitting below and at the Fermi level. We apply this approach to the interfaces between a Co monolayer and 4d (Tc, Ru, Rh, Pd, and Ag) or 5d (Re, Os, Ir, Pt, and Au) transition metals and find a clear correlation between the overall size of the band splitting and the charge transfer between the d-orbitals at the interface. Furthermore, we show that the spin splitting at the Fermi surface scales with the induced orbital moment weighted by the strength of the spin-orbit coupling.

ACKNOWLEDGMENT

The accomplishment of this dissertation thesis would not be possible without assistance and support of so many people whose names may not all be enumerated. It is a genuine pleasure to express my deep sense of thanks and gratitude to my supervisor, Prof. Udo Schwingenschlogl, for his understanding, generous guidance and precious advices regarding the topic of my research. His scientific approach and meticulous scrutiny have always been crucial to accomplish this work. His discipline and good time management helped me to be more productive. It was a great pleasure working with him.

I would like to acknowledge Prof. Aurelien Manchon for his overwhelming attitude to help, keen interest in my research, recommended literature and many fruitful discussions that made it possible for me to work on spintronics. I owe a deep sense of gratitude to Prof. Jorg Eppinger and Prof. Alexander Chroneos for being the committee members of my thesis dissertation and for their time and all efforts that they put to make my work better.

Also, I am extremely thankful to Joshua Tobechukwu Obodo, Altynbek Murat and Elvis Shoko for the time they spend to read my dissertation thesis and to make corrections. I am hugely indebted to Abderrezak Belabbes, whose expertise in computational physics helped me to learn a new computational code very quickly and to be able to use it efficiently in my research. Also, I am highly grateful to Maxim Peskov and Fabrizio Cossu for the projects we have done together. I am grateful to Joshua Tobechukwu Obodoand for the great time we spend playing football, going regularly to gym and to "Italian" restaurant. I am thankful to Altynbek Murat for informing

us about interesting seminars and presentations that usually were supplemented with free food. I am thankful to Enrique Montes for nice scuba diving experience in Red Sea that gave me great inspiration to do my research harder.

I owe a deep sense of gratitude to Sumit Ghosh for many fruitful discussions related to theoretical physics that not only helped me to understand my research better but also very often confused me pushing to think more about nature of different phenomena. I would like to thank to Amir Hanna for his shared knowledge about future perspective of semiconductor electronics convincing that this field has some future and urging to be more realistic regarding spintronics. I am thankful to Chris Ortiz for his explanations of physical phenomena related to spintronics during our amazing adventures in Saudi Arabia and outside the Kingdom, in desert and in different cities. I am thankful to Hamed Saidaoui for many hours we spend together in library preparing for our qualifier exam and discussing about the science.

I am indebted to Shoikot Iftekharul Alam, for being my close friend for many years, for food that we have cooked and movies that we have watched together and for many discussions. Also, I am thankful to Lina Abdul Halim for giving the right advice at the right time and for being a source of motivation. I am extremely thankful to my friends Volodymyr Taranovych and Natalia Lashchyk for their constant encouragement through my research period. I am particularly indebted to my parents and my brother who put their faith in me and urged me to do better.

And finally, I would like to acknowledge the King Abdullah University of Science and Technology for funding my work and supercomputer "Shaheen" and "Noor" teams for providing all technical support during my research pursuit.

TABLE OF CONTENTS

LIST OF FIGURES

LIST OF TABLES

Chapter 1

Introduction

Interfaces play a key role in todays world of nanotechnology that constantly demands higher speed (in data recording and transmission, for example), lower energy consumption, and reduced size, heating, and material degradation. These demands make it more and more important to account for quantum effects, which show up regularly at surfaces and interfaces, giving rise to an incredible variety of novel physical phenomena. An illustrative example are magnetic interfaces revealing spin-dependent electron transport phenomena in solid-state devices and enables the use of the electron spin, as well as its charge, for carrying information. As an example, ferromagnetic metallic films separated by nonmagnetic metallic spacer layer show significant change in the electrical resistance depending on relative alignment of magnetization in adjacent ferromagnetic layers. This effect is known as giant magnetoresistance (GMR) [1, 2] and has been used in modern hard-drive read heads and magnetic random access memories. Another example is tunneling magnetoresistance (TMR) [3] in ferromagnetic metallic films separated by insulator. This effect is similar to GMR, however it is much stronger and now is being used for nonvolatile random access memory.

Magnetic interfaces due to the reduced dimensionality and different type of magnetic interactions enables the manipulation of electron spin by either magnetic or electrical field. This new paradigm has been called spintronics and it receives a lot

of attention for the information processing because manipulation of the spin density by either magnetic or electrical field consumes much less energy compare to the manipulation of moving electrons in traditional semiconductor electronic devices usually associated with large ohmic energy dissipation. In addition, since the information in such devices is stored in the form of magnetic states it is preserved even at zero bias voltage.

The most prominent feature of the magnetic interfaces is the magnetic anisotropy. Depending on application, different types of magnetic anisotropy are used. In particular, for the magneto-electronics sensing devices it is exchange bias that stems from the exchange coupling between ferromagnet and antiferromagnet [4]. In magnetoresistive random access memories have been using materials displaying the in-plane shape anisotropy [5] that is common for many thin films. And finally, of great interest for modern spintronic devices, such as magnetic memory and logic devices, are magnetic systems displaying large interfacial-induced perpendicular magnetic anisotropy. This anisotropy is a result of the symmetry breaking and spin-orbit coupling that was observed at the interfaces between transition metal ferromagnets and noble metals [6] or metal oxides [7–9]. This combination has proven successful in reducing the critical current density needed to achieve current-driven magnetic excitations and switching within a reasonable range.

Even if the physical and chemical properties of the involved solids in their bulk form are known, investigation of the interface is very challenging for experiments due to the small dimensions. An effective way to explore many aspects of such interfaces in atomic level is opened by ab initio calculations. Two types of magnetic interfaces, with large capacity for spintronics applications are studied in this work by first principle calculations:

1. interfaces between transition metal ferromagnets and nonmagnetic heavy metals (FM/NM), and

2. interfaces between antiferromagnet and ferromagnet (AFM/FM).

In addition to the magnetic anisotropy, numerous quantum effects show up at those interfaces giving rise to an incredible variety of novel physical phenomena. For example, magnetic switching in $5d/3d$ multilayer structures (used for GMR) can be achieved by spin transfer torque [10, 11]. Also, an electric current at such interfaces can induce a spin current [12] due to the spin Hall effect [13] and can generate a spin density [14] as a result of Rashba effect [15]. Those effects, respectively, generate spin transfer [10, 11] and spin orbit [8] torques that leads to either magnetization reversal [16] or magnetization auto-oscillations [17]. For example, magnetic switching based on spin orbit torque has been observed in ultrathin Co layers interfaced with Pt [18, 19]. Large antisymmetric exchange (interfacial Dzyaloshinskii-Moriya interaction) obtained at the interfaces between heavy metals and transition metal ferromagnets, results in skyrmion lattices [20–23] or spin helices and spiral [24, 25]. When antisymmetric exchange is present at the $5d/3d$ interfaces, spin transfer torque can move domain walls very efficiently [19, 26]. This effect could reduce the energy needed to store and retrieve one bit of data by a factor of 10,000 and thus it enables new concepts for memory and logic devices [27, 28]. From the technological point of view the $5d/3d$ interfaces enable manipulation of the magnetism via an electric field [29], and thus they require small charge transfer, provide high speed data transmission in miniature components, and solve problems of overheating and material degradation in traditional devices [30, 31].

Another type of interfaces studied in this work, the AFM/FM systems recently attract attention due to their potential applications in high density magnetic recording media [32], domain stabilizers in recording heads [33], and spin-valve devices [34]. A key property at such interfaces is exchange bias [35]. It stems from the interaction between FM and AFM layers and is characterized by enhanced coercivity and shifted FM hysteresis loop, see Fig. 1.1. Systems exhibiting exchange bias have been stud-

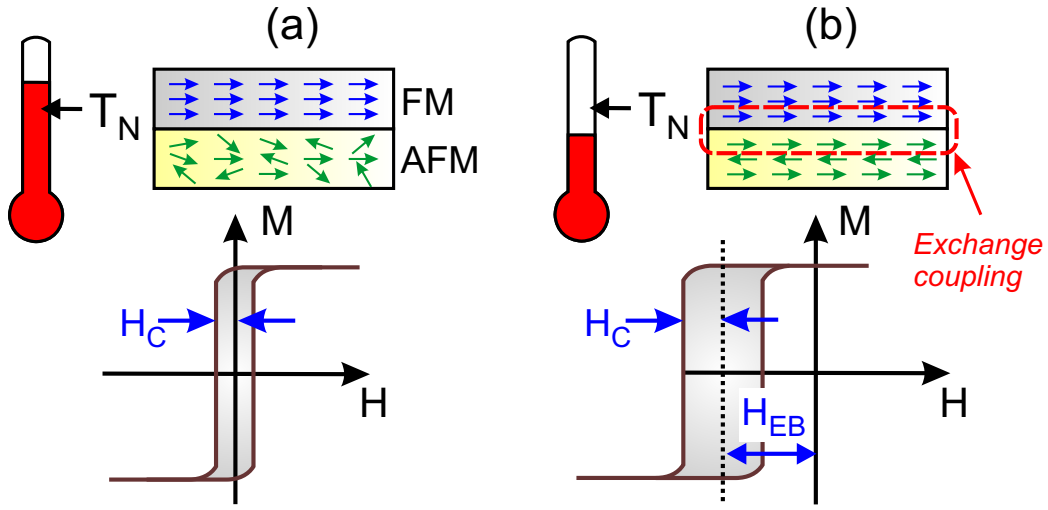

Figure 1.1: A schematic picture of the exchange-bias phenomena. (a) When temperature is above the Néel temperature of the AFM T_N spins of AFM are disordered. b) When temperature is below T_N spins of AFM are ordered and the exchange coupling between FM and AFM shifts the hysteresis loop by H_{EB} and can enhance the coercivity H_C.

ied experimentally [36–38]; among them CoO/Ni and CoO/Py (where Py stands for permalloy, an alloy of Fe and Ni), are very attractive because of the out-of-plane magnetic anisotropy [39, 40] which enables the production of high-density and low-power consumption devices [41, 42]. Also, the Néel temperature (the lowest temperature of the AFM phase) of CoO is higher than room temperature and magnetization in soft-magnetic materials, such as Permalloy, is easier to switch.

Despite potential for applications, the physical properties of magnetic interfaces, such as the origin of the perpendicular magnetic anisotropy, are not well understood, mainly because they depend on external factors such as the interface quality, the film thickness, atomic inter-diffusion, surface oxidation, segregation, and various defects arising from lattice mismatch. Such changes of structural details can strongly alter the electronic states, which in turn influences the magnetic properties and is a main reason for many discrepancies between experiment and theory [43–45]. For this reason, knowledge about the structure on an atomic level is key for understanding such interfaces.

First principles techniques based on density functional theory nowadays are widely used for investigating interfaces. It is often assumed that the lattice parameters of the component materials are the same (coherent model). However, this approach is valid only for small lattice mismatch, whereas for the Au/Co and Pt/Co interfaces, for instance, the lattice mismatch amounts to 16.5% and 12.7%, respectively, which results in such a strong strain that unphysical results have to be expected. For example, the theoretical study in Ref. [46] is based on ab-initio calculations using a coherent model of the Pt/Co interface. The authors find for the Co atoms a magnetization of 2.1 μ_B, while the experimental value is 1.8 μ_B [47].

A possible way to avoid the problem of lattice mismatch is the application of supercells such that the two component materials form a Moiré pattern. In fact, such patterns have been observed experimentally in a wide range of interfaces, such as Graphene/Ir [48], Graphene/Co/Ir(111) [49], Au/Co [50, 51], Pt/Co [52], FeO/Pd [53], FeO/Pt [54], and Fe/MgO [55]. By means of Moiré supercells the strain on the component materials can be reduced significantly. For example, in (5×5)Au/(6×6)Co and (7×7)Pt/(8×8)Co supercells the lattice mismatch is reduced to 0.2%. Using even larger supercells could further reduce it, but with the increased number of atoms the computational demand of first principles calculations grows dramatically. While the supercell approach enables us to describe the physical properties in the bulk-like regions properly, the interface itself remains an issue. This leads to the question, does the structure really resemble the bulk-like regions, as assumed by standard Moiré supercells? To answer this question we study in details the structures and resulting magnetism of AFM/FM (CoO/Ni and CoO/$Ni_{80}Fe_{20}$) and NM/FM (Au/Co and Pt/Co) interfaces, see Chapter 3.

In addition, the magnetic properties of such interfaces are very sensitive to internal and external factors. Surface oxidation, film and substrate thickness variations, surface strain and roughness, atomic inter-diffusion, segregation, and various defects

arising from lattice mismatch are common phenomena. This is also another reason for many discrepancies between experiment and theory [43–45]. For example, first principles calculations for a defect-free Au/Co interface with the Co in-plane lattice parameter adjusted to the Au substrate (coherent model) result in an in-plane magnetization [56, 57], while experimental findings point to out-of-plane magnetization [50, 51, 58]. Bruno and Renard have demonstrated using phenomenological models that the strain due to lattice mismatch induces an effective anisotropy [59]. It also has been shown in Ref. [60] that deposition of Co atoms on Au results in a surface alloy by Co-Au intermixing, which can modify the magnetic properties of the interface dramatically. Therefore, in Chapter 4 we study the magnetic anisotropy of the Au/Co interface on atomic level and its dependence on structural details such as surface oxidation, film and substrate thickness variations, and atomic inter-diffusion.

Sharp interface between the ferromagnets and the noble metals breaks the inversion symmetry along the normal to the interface, $\mathbf{z}$ that in combination with the large spin-orbit coupling of the noble metals results in spin splitting of an electron gas, a phenomenon called Rashba effect [15, 61]. Such spin splitting enables the accumulation and therefore manipulation of the electron spins in ferromagnets via small electric fields, which has great potential in logic [62] and memory [27] devices. In a simplistic picture, spin-orbit coupling Hamiltonian in presence of the broken inversion symmetry has a form

$$H_R \approx -\alpha_R \boldsymbol{\sigma} \cdot (\boldsymbol{z} \times \mathbf{k}) \tag{1.1}$$

where α_R is Rashba parameter (describing the magnitude of the spin-orbit splitting), $\boldsymbol{\sigma}$ and $\mathbf{k}$ are electron spin and wavevector, respectively, and $\boldsymbol{z}$ points out the direction normal to the surface [15, 63]. Such $\mathbf{k}$-linear spin-orbit coupling has been observed at the surface of various metals such as Au [64, 65], Gd [66], or Bi compounds [67–69] and more recently at the surface of three dimensional topological insulators [70, 71]. Notice

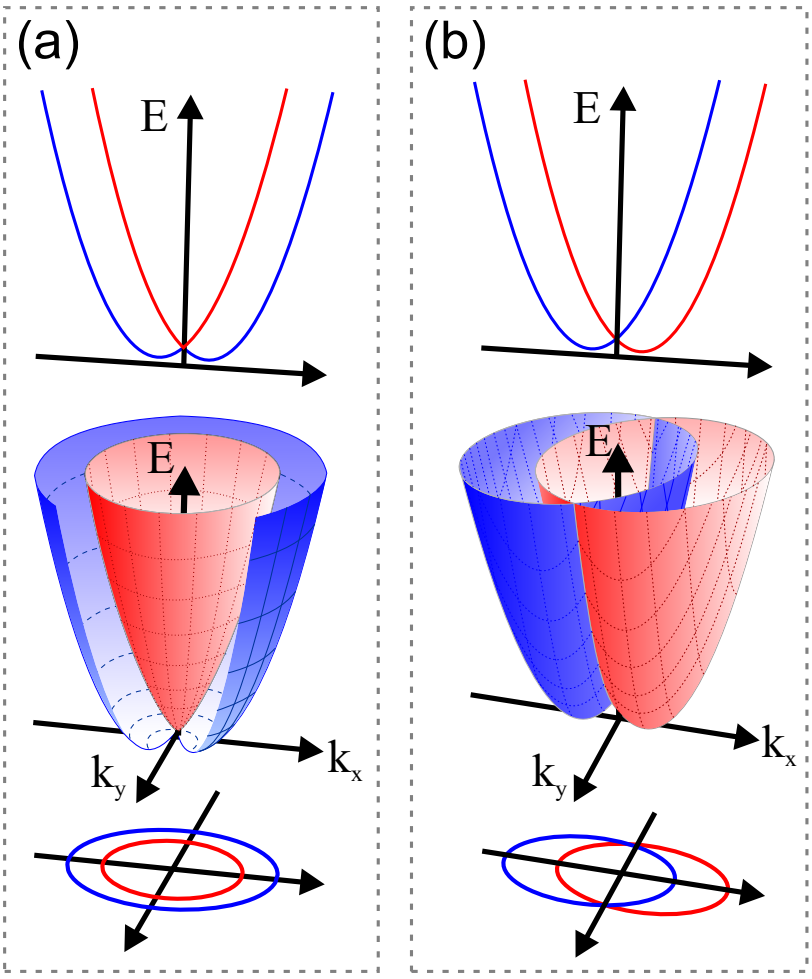

Figure 1.2: Shift of the parabolic band due to Rashba spin-orbit coupling at (a) non-magnetic and (b) magnetic surface or interface. Red (blue) color stands for spin-up (spin-down) states. On (b) magnetization is along k_y. On top band structure along k_x and on bottom its cross-section with the Fermi surface.

that in general, spatial inversion symmetry breaking imposes the spin-orbit coupling term to be *odd* in momentum $\mathbf{k}$, but not necessarily linear. Indeed, such odd-in-k spin-orbit coupling is well known in bulk non-centrosymmetric semiconductors [72] and has been detected recently at oxide heterointerfaces [73].

Traditionally, the Rashba effect is attributed to materials with free electrons, being characterised by a linear shift of the energy bands in k space [15], see Fig. 1.2,

$$E^{\pm} = \frac{\hbar^2 k^2}{2m} \pm \alpha_R k, \tag{1.2}$$

where ± denotes the spin direction. The Rashba parameter is given by

$$\alpha_R = \frac{\Delta E}{2k} = \frac{\hbar^2}{2m^*}\Delta k, \tag{1.3}$$

where $\Delta E = E^+ - E^-$ and m^* is an effective mass. For parabolic bands with $m^* = \hbar^2(\frac{d^2E}{dk^2})^{-1}$ the band shift is $\Delta k = k^+ - k^- = 2m^*\alpha_R = constant$. Such a splitting has been confirmed experimentally for semiconductors [74–78] and a number of metallic surfaces [64, 66, 67, 79–84].

Significant insights in the Rashba effect have been obtained by first principles calculations. For instance, it has been shown that α_R is proportional simultaneously to the spin-orbit coupling and gradient of the surface potential [63]. The electric field normal to the surface interacts with the electric dipole created by the orbital moment, to yield Rashba band splitting [85]. The role of the asymmetry of the wavefunction has been highlighted in Ref. [86]. While first principles calculations do provide insight in materials with largely free electrons and well isolated surface/interface states (such as the Au(111) [64] and Ir(111) [84] surfaces and the Bi/Ag(111) interface [80]), many metallic surfaces and interfaces have non-parabolic bands and their states hybridize with bulk states, see for example Ref. [81, 87]. In addition, the value and sign of the Rashba parameter can vary from band to band due to band-specific chiral ordering of the orbital moment [87, 88]. Since the bands are not parabolic Eq. 1.3 can not be used to calculate Rashba parameter. Thus in chapter 5 we develop a computational approach in order to estimate the magnitude of the band splitting below and at the Fermi level for materials with complex electronic structure. With this approach we systematically investigate the band splitting at the interface between a Co monolayer and 4*d* (Tc, Ru, Rh, Pd, and Ag) or 5*d* (Re, Os, Ir, Pt, and Au) transition metals and analyze its dependence on magnetic properties, electronic configuration and strength of the spin-orbit coupling. A serious issue for computational studies of

the Rashba effect at metallic interfaces is the typically large lattice mismatch. Nevertheless, the state-of-the-art methodology is the coherent model that neglects the lattice mismatch [63, 85–88]. Therefore, to quantify the Rashba band splitting at the NM/FM interfaces we use supercell approach in chapter 6.

Chapter 2

Theoretical Methodology

2.1 The Schrödinger Equation for many interacting particles

A system containing M nuclei and N electrons can be described by many body wave function $\Psi(\{R_A\},\{r_i,\sigma_i\})$, where R_A $(A = 1,...,M)$ and r_i $(i = 1,...,N)$ are their spatial coordinates, respectively, and σ_i is electron spin. The ground state energy of such a system of electrons and nuclei interacting with each other may be computed by solving the time independent Schrödinger equation

$$\hat{H}\Psi(\{R_A\},\{r_i,\sigma_i\}) = E\Psi(\{R_A\},\{r_i,\sigma_i\}) \quad , \tag{2.1}$$

where the Hamiltonian operator, $\hat{H}$, consists of the kinetic energies of electrons (T_e) and nuclei (T_p) and the potential energies of electron-electron (V_{e-e}), electron-nuclei (V_{e-p}), and nuclei-nuclei (V_{p-p}) interactions. The fact that nuclei are much heavier than the electrons allows to separate their motions (Born-Oppenheimer Approximation [89]) and as a result, the kinetic energy of nuclei T_p can be neglected and the repulsion between nuclei, can be treated as a constant for a fixed configuration of the nuclei. Thus the Hamiltonian in Eq. 2.1 can be simplified by considering only electron

kinetic energy, electron-nuclear attraction, and interelectronic repulsion terms

$$\hat{H}_e = -\frac{1}{2}\sum_{i=1}^{N}\nabla_i^2 + \sum_{i=1}^{N}\sum_{A=1}^{M}\frac{Z_A}{|\mathbf{R}_A - \mathbf{r}_i|} + \sum_{i=1}^{N}\sum_{j>i}^{N}\frac{1}{|\mathbf{r}_i - \mathbf{r}_j|} \quad , \tag{2.2}$$

where Z_A is the charge of nucleus A. Notice that we use atomic units that implies $m = \hbar = e^2/(4\pi\epsilon_0) = 1$. Since $\psi_e(\{\boldsymbol{R}_A\}, \{\boldsymbol{r}_i, \boldsymbol{\sigma}_i\})$ depends on nuclear coordinates (R_A) only parametrically, for a given nuclear configuration, Eq. 2.1 can be rewritten

$$\hat{H}\Psi(\{\boldsymbol{x}_i\}) = E\Psi(\{\boldsymbol{x}_i\}) \quad , \tag{2.3}$$

where for simplicity notations $\hat{H}_e = \hat{H}$, $\psi_e = \Psi$, and $\{\boldsymbol{x}_i\} = \{\boldsymbol{r}_i, \boldsymbol{\sigma}_i\}$ are used.

The major difficulty in solving Eq. 2.3 is the electron-electron interaction (third term in Eq. 2.2), that couples all electrons in the system due to the long range electrostatic potential. As a result electron motion is correlated and implies the treatment of 3N variables for an N-electron system. In practice, such a many-body problem cannot be solved without employment of approximations. All known approximation schemes can be divided in to two major categories: (i) the wave function based methods, where the many-electron wave function is the key (Tight-binding model and Hartree-Fock method, for example); and (ii) density-functional theory (DFT), in which electron density is the central quantity.

2.1.1 Hartree-Fock Approximation

The Pauli exclusion principle results in an antisymmetric wave function. For example, for a system with two electrons which occupy the spin orbitals ϕ_1 and ϕ_2 a total wavefunction has the form

$$\Psi(\boldsymbol{x}_1, \boldsymbol{x}_2) = \frac{1}{\sqrt{2}}[\phi_1(\boldsymbol{x}_1)\phi_2(\boldsymbol{x}_2) - \phi_1(\boldsymbol{x}_2)\phi_2(\boldsymbol{x}_1)] \tag{2.4}$$

that can be represented in matrix form

$$\Psi(\boldsymbol{x}_1, \boldsymbol{x}_2) = \frac{1}{\sqrt{2}} \begin{vmatrix} \phi_1(\boldsymbol{x}_1) & \phi_2(\boldsymbol{x}_1) \\ \phi_1(\boldsymbol{x}_2) & \phi_2(\boldsymbol{x}_2) \end{vmatrix} \tag{2.5}$$

In case of N electrons the ground state wave function is approximated by a Slater determinant (linear combination of the product of independent electron wave functions, known as spin orbitals):

$$\Psi(\boldsymbol{x}_1, \boldsymbol{x}_2, \cdots, \boldsymbol{x}_N) = \frac{1}{\sqrt{N!}} \begin{vmatrix} \phi_1(\boldsymbol{x}_1) & \phi_2(\boldsymbol{x}_1) & \cdots & \phi_N(\boldsymbol{x}_1) \\ \phi_1(\boldsymbol{x}_2) & \phi_2(\boldsymbol{x}_2) & \cdots & \phi_N(\boldsymbol{x}_2) \\ \vdots & \vdots & \ddots & \vdots \\ \phi_1(\boldsymbol{x}_N) & \phi_2(\boldsymbol{x}_N) & \cdots & \phi_N(\boldsymbol{x}_N) \end{vmatrix} \tag{2.6}$$

Note that interchanging the coordinates of two electrons will change sign of Ψ and thus the requirement of antisymmetry is preserved. Also, the Pauli exclusion principle holds since an attempt to place two electrons in the same spin orbital ($\boldsymbol{x}_i = \boldsymbol{x}_j = \boldsymbol{x}'$) gives zero probability because $\Psi(\boldsymbol{x}_1, ..., \boldsymbol{x}', ..., \boldsymbol{x}', ...\boldsymbol{x}_N) = 0$.

The energy of the system is the expectation value of $\hat{H}$

$$\begin{aligned} E[\Psi] &= \left\langle \Psi | \hat{H} | \Psi \right\rangle \\ &= \sum_{i=1}^{N} \int \phi_i^*(x_i)[-\frac{\nabla_i^2}{2} + V^{ext}(x_i)]\phi_i(x_i)dx_i \\ &+ \frac{1}{2}\sum_{i=1}^{N}\sum_{j=1}^{N} \iint \phi_i^*(x_i)\phi_j^*(x_j)\frac{1}{|r_i - r_j|}\phi_j(x_j)\phi_i(x_i)dx_i dx_j \\ &- \frac{1}{2}\sum_{i=1}^{N}\sum_{j=1}^{N} \iint \phi_i^*(x_i)\phi_j^*(x_j)\frac{1}{|r_i - r_j|}\phi_j(x_i)\phi_i(x_j)dx_i dx_j \quad . \end{aligned} \tag{2.7}$$

The notation $[\Psi]$ emphasises the fact that the energy is a functional of the wavefunction. The ground state energy can be calculated by applying the variational principle

to Eq. 2.3:

$$E_0 = \min_{\Psi} \; E[\Psi] \tag{2.8}$$

Since the independent electron wave functions $\phi_i(x_i)$ are orthonormal, a complex N-electron Schrödinger equation can be reduced to an effective one-electron Schrödinger-like equations

$$\hat{F}_i \phi_i(x_i) = \epsilon_i \phi_i(x_i), \tag{2.9}$$

where

$$\hat{F}_i = -\frac{\nabla^2}{2} + V^{ext}(x_i) + V^H(x_i) + V_i^{Exchange}(x_i) \tag{2.10}$$

is a one-electron Hamiltonian, ϕ_i and ϵ_i are the eigenvectors and eigenvalues, respectively. The terms in the above Hamiltonian stand for: 1) the kinetic energy of N independent electrons, 2) the Coulomb attraction on i^{th} electron due to all the nuclei, 3) the Coulomb repulsion between i^{th} electron and the electron density produced by all electrons (Hartree potential)

$$V^H(x_i) = \int \frac{n(x_j)}{|r_i - r_j|} dx_j, \quad n(x_j) = \sum_{j=1}^{N} |\phi_j(x_j)|^2 \quad , \tag{2.11}$$

and 4) exchange potential that appears from the antisymmetric nature of the wave function and does not have any classical analogy.

The beauty of this method is that it treats the exchange interaction between electrons with the same spin exactly. However a major drawback of it is that it implies independent electron motion, while in reality motion of electrons is correlated.

2.2 Density-Functional Theory (DFT)

Density functional theory has become the most widely used computational quantum mechanical approach today in physics, chemistry and materials science in investiga-

tions of the electronic structure of atoms, molecules and solids. In this section, the basic concepts underlying density functional theory (DFT) will be given outlining the main features of spin-orbit coupling and interfaces. More extensive discussions of DFT can be found in several excellent review articles [90–92] and textbooks [93–95].

The central quantity in DFT is electron density

$$n(\boldsymbol{r}) = N \int \cdots \int |\Psi(\boldsymbol{x}, \boldsymbol{x}_2, ..., \boldsymbol{x}_N)|^2 d\boldsymbol{x}_2 \ldots d\boldsymbol{x}_N \quad , \tag{2.12}$$

where $\{\boldsymbol{x}_i\}$ represents both spatial $\{\boldsymbol{r}_i\}$ and spin $\{\boldsymbol{\sigma}_i\}$ coordinates. In contrast to wave-function methods that depend on $3N$ variables, electron density is always 3-dimensional quantity. Such reduction of dimensionality enables DFT to be applied to much larger systems as compared to the wave-function methods.

DFT takes its origin from the Thomas-Fermi model [96, 97] developed in 1927, and demonstrated semiclassically that the energy can be determined using the electron density. Fully quantum mechanical approach which allows to express the electronic Hamiltonian as a functional of electron density was made in 1964 by Hohenberg and Kohn [98]. Their work is based on two theorems which are the pillars of DFT.

Theorem 2.2.1. *For any system of interacting particles in an external potential $v(r)$ there exists a one-to-one correspondence between external potential $v(r)$ and electron density $n(r)$.*

Theorem 2.2.2. *The total energy functional $E[n(r)]$ has a minimum at the correct ground state electron density $n_0(r)$,*

$$E[n_0(r)] \leqslant E[n(r)] \quad .$$

The first theorem states that the electron density $n(r)$ uniquely determines external potential $v(r)$, or that no two different external potentials can give the same $n(r)$.

The second Hohenberg-Kohn theorem demonstrates that the ground state electron density and the ground state energy can be found by using a variational principle. The energy E as a function of the electron density n is

$$\begin{aligned} E[n] &= T[n] + V_{ep}[n] + V_{ee}[n] \\ &= \int n(r)v(r)dr + V_{HF}[n] \quad , \end{aligned} \tag{2.13}$$

where

$$V_{HF} = T[n] + V_{ee}[n] \quad , \tag{2.14}$$

depends only on electron density n (is independent from external potential v) and, thus, it is a universal functional of n.

2.2.1 The Kohn-Sham Equations

Hohenberg-Kohn theorems show that there is one-to-one correspondence between the total energy of interacting particles in a system and their ground state density. However, they do not say how to obtain the $n(r)$ and $F_{HF}(r)$. Thomas-Fermi theory was the first attempt to calculate the total energy from the ground state density, however, it fails to obtain correct results due to an improper description of the kinetic energy.

Practical use of DFT was achieved in 1965 when Kohn and Sham introduced a mean field theory for non-interacting electrons in an effective potential [99]. In this model the kinetic energy of interacting electrons is approximated by the kinetic energy of non-interacting electrons T_s and the the external field is replaced by an effective external field V_{eff} (called the Kohn-Sham potential). All missing quantum effects including contributions to the kinetic energy due to electron correlation are included in a term called the exchange-correlation energy (E_{xc}). In such a case the energy

functional has a form,

$$E[n(r)] = T_s[n(r)] + \underbrace{\int n(r)v(r)dr + V_H[n(r)] + E_{xc}[n(r)]}_{V_{eff}} \tag{2.15}$$

and an effective potential can be presented as

$$\begin{aligned} v_{eff} = \frac{V_{eff}}{\delta n} &= v(r) + \frac{V_H[n]}{\delta n} + \frac{E_{xc}[n]}{\delta n} \\ &= v(r) + \int \frac{n(r')}{|r - r'|} dr' + v_{xc}(r) \quad . \end{aligned} \tag{2.16}$$

This leads to the Kohn-Sham (KH) equations which are similar to the Hartree-Fock solution (see Eq. 2.9) are effective one-electron equations:

$$\left[-\frac{1}{2}\nabla^2 + v_{eff} \right] \phi_i = \epsilon_i \phi_i \quad , \tag{2.17}$$

where ϵ_i are the energies of the one-electron orbitals ϕ_i. These Kohn-Sham equations have the same structure as the Hartree-Fock equations (Eq. 2.9) with the exchange potential $V^{Exchange}$ (Eq. 2.10) replaced by the exchange-correlation potential E_{xc}. Thus Kohn-Sham wavefunction of the system can be defined as a single Slater determinant constructed from a set of orbitals ϕ_i (see Eq. 2.6) that are the lowest energy solutions to Eq. 2.17. Note that the Kohn-Sham equations must be solved self-consistently because v_{eff} depends on electron density n (Eq. 2.16) that is defined through the one-electron orbitals ϕ_i:

$$n(r) = \sum_{i=1}^{N} |\phi_i|^2 \quad . \tag{2.18}$$

Finally, note that the total energy is not the sum of the orbital energies $E \neq \sum_i^N \epsilon_i$ however it can be calculated from the resulting density through

$$E = \sum_{i=1}^{N} \epsilon_i - \frac{1}{2} \int \int \frac{n(r)n(r')}{|r - r'|} dr dr' + E_{xc}[n] - \int v_{xc}(r)n(r)dr \tag{2.19}$$

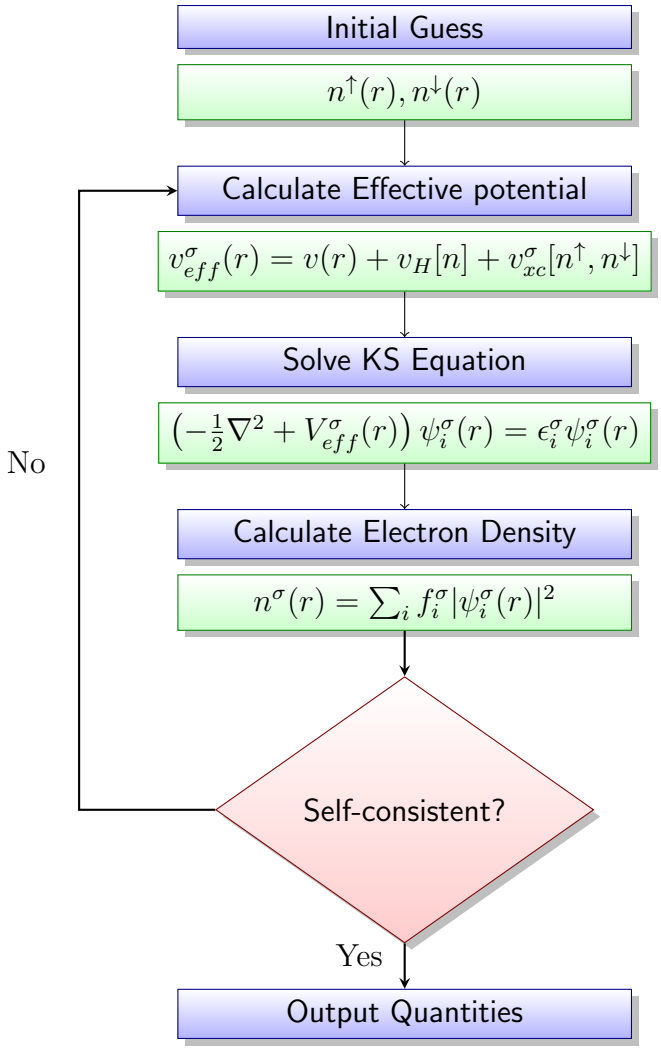

Figure 2.1: Major steps in DFT electronic structure calculations: self-consistent (SCF) cycle.

The general algorithm of solving KS equation is shown on Fig. 2.1. It starts with an initial guess of the electron density n', V'_{eff} is obtained from Eq. 2.16, Kohn-Sham orbitals ϕ'_i are calculated from Eq. 2.17, energy E' is calculated from Eq. 2.19 and a new density n'' is obtained from Eq. 2.18. This process, $n' \rightarrow V'_{eff} \rightarrow \phi'_i \rightarrow n'' \rightarrow \ldots n^{(p)}$, is repeated p-times until convergence is achieved: $E[n^{(p)}] - E[n^{(p-1)}] < E_{convergance}$. Remarkably, the Kohn-Sham approach applied to the "not realistic" system consisting of non-interacting electrons gives the same electron density and ground state energy as it is in "real" system described by the Schrödinger equation,

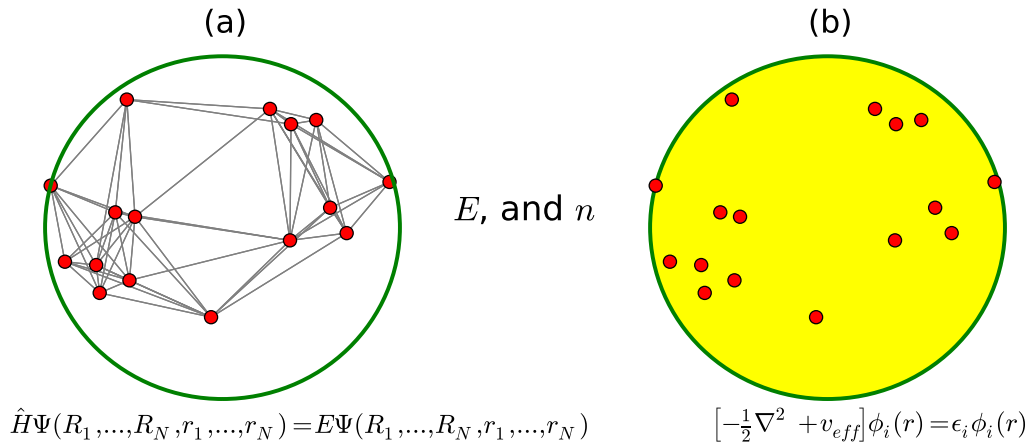

Figure 2.2: Schematic picture illustrating (a) system of $N-$ interacting particles and (b) system of $N-$ non-interacting particles (particles interact only with a background potential v_{eff}, see Eq. 2.17, due to all other electrons moving in a potential of fixed nuclei). Yellow cloud represents an effective external potential v_{eff}. Ground state energy E and electron density n are the same in (a) and (b).

as it is demonstrated on schematic Figure 2.2.

2.2.2 Exchange-Correlation Functionals

All quantum effects due to electron-electron interaction are hidden in the exchange-correlation energy, see Eq. 2.15. However, the explicit form of the exchange correlation is unknown and thus it is necessary to approximate it. In this section two of the most common types of exchange-correlation functionals are briefly discussed: Local-Density Approximation (LDA) and Generalised Gradient Approximation (GGA).

The local-density approximation (LDA)

In many cases solids can often be considered as a homogeneous or almost homogeneous electron gas. In such systems both the external potential and electron density have local character. Even if the electron density is inhomogeneous the electron gas can be divided into small regions containing a homogeneous electron gas with some average density. Since the functional $E_{xc}[n]$ is universal, it can be approximated as a local

or nearly local functional of the density. Assuming the exchange-correlation energy density $\epsilon_{xc}(n)$ to be the same at each point as in a homogeneous electron gas with that density n the exchange-correlation energy E_{xc} for a spin-unpolarized system in the local-density approximation (LDA) can be written as

$$E_{xc}^{LDA}[n] = \int d^3r \epsilon_{xc}(n(r)) \tag{2.20}$$

Within the LDA $\epsilon_{xc}(r)$ is a function of only the local value of the density n and it can be decomposed into exchange and correlation terms linearly,

$$\epsilon_{xc} = \epsilon_x + \epsilon_c \tag{2.21}$$

The exchange energy density ϵ_x, for a homogeneous electron gas, is known analytically [100]

$$\epsilon_x = -0.74\ n^{1/3} \tag{2.22}$$

However, the correlation energy density ϵ_c, is unknown and has been calculated for the homogeneous electron gas to great accuracy with Monte Carlo methods [101].

The LDA approximation is very accurate for systems with slowly varying electron density (like a nearly-free-electron metal) and worst for very inhomogeneous systems like single atoms where electron density must go to zero outside of the atom.

The Generalised gradient Approximation (GGA)

In contrast to the LDA the GGA takes into account the gradient of the density, $\nabla n(r)$, at each coordinate:

$$E_{xc}^{GGA}[n] = \int d^3r \epsilon_{xc}(n(r), |\nabla n(r)|) \tag{2.23}$$

This approach yields better results than the LDA for many properties such as ground state energies of molecules or electronic properties of semiconductors. However, in case of metals and their surfaces, GGA is not necessarily better than LDA. Depending on system different GGA functionals were developed. For example, the most widely used GGA in surface physics are Perdew-Wang (PW91) [102] and Perdew-Burke,-Enzerhof (PBE) [103] functionals.

Strongly correlated systems: LDA+U

One of the most serious problems for LDA or GGA approaches occurs for materials in which electrons are localised and strongly interacting, such as transition metal oxides and rare earth elements. For example, DFT calculations of transition metal oxides (NiO and CoO) based on GGA approach reveal too small band gap (0.5 eV and 0.8 eV, respectively) compared to experimental data (3.8 eV and 2.6 eV) [104]. Also, magnetic moments of those metals in their oxides calculated with GGA are much smaller compared to experiment [104]. This problem arises from a very large Coulomb repulsion of the strongly localized electrons on $3d$-orbitals. The energy of the band gap and magnetic properties can be corrected by adding to LDA or GGA calculations an additional orbital-dependent repulsion term "U" that increases gap between the filled and empty 3d states [105]. In this way LDA+U shifts the localised orbitals (usually, d or f) relative to the other orbitals and thus describes correctly the electronic and magnetic properties of the strongly correlated systems using the Hubbard model [106], while the rest of valence electrons are treated at the level of standard DFT functionals.

2.2.3 Spin-polarized Density Functional Theory

Up to now we have assumed that the electron gas is unpolarized, however, in reality spin-density functional theory [107] is needed for the investigation of the magnetic

systems. This can be achieved by generalizing the Hohenberg-Kohn-Sham scheme to Spin Density Functional formalism [108]. Though the Kohn-Sham approach with LDA or GGA functionals achieves remarkable results for many systems without consideration of the electron spin, for the systems with open shell atoms (for example, transition metals and rare-earth metals, in which the conduction electrons are spin polarized by exchange interaction with the localized magnetic moments) the spin properties of the electronic structure must be accounted for.

Considering that spin can vary continuously from $-\frac{1}{2}$ to $\frac{1}{2}$ the density of spin-up and spin-down electrons, respectively, in general can be defined as:

$$n^{\uparrow}(r) = N \int |\Psi([r,+1/2],[r_2,s_2],\ldots,[r_N,s_N])|^2 dr_2 ds_2 \ldots dr_N ds_N \quad , \tag{2.24}$$

$$n^{\downarrow}(r) = N \int |\Psi([r,-1/2],[r_2,s_2],\ldots,[r_N,s_N])|^2 dr_2 ds_2 \ldots dr_N ds_N \quad , \tag{2.25}$$

and total spin density is

$$n(r) = n^{\uparrow}(r) + n^{\downarrow}(r) \quad . \tag{2.26}$$

In accordance to the Hohenberg-Kohn theorem only total electron density is required for obtaining the exact ground-state energy and electron density. However, since Kohn-Sham equation (Eq. 2.17) is an effective one-electron equation, it can be applied separately for spin-up and spin-down electron densities. The non-interacting kinetic energy in such a case is the sum of the separate kinetic energies of the spin-up and spin-down electrons:

$$T_S[n^{\uparrow}, n^{\downarrow}] = T_S[n^{\uparrow}] + T_S[n^{\downarrow}] \quad . \tag{2.27}$$

Such noninteracting kinetic energy results in a spin-state specific exchange-correlation functional [109] that can be similarly split for spin up and spin down electron densities:

$$E_{xc}[n^{\uparrow}, n^{\downarrow}] = E_{xc}[n^{\uparrow}] + E_{xc}[n^{\downarrow}] \quad . \tag{2.28}$$

In such a case, the total energy E for a system comprised of two well-separated subsystems with energies $E[n^{\uparrow}]$ and $E[n^{\downarrow}]$ must be

$$E[n] = E[n^{\uparrow}] + E[n^{\downarrow}] \quad . \tag{2.29}$$

Minimizing the total energy functional $E[n]$ only yields the ground-state energy and spin density, however, it does not count the lowest state of a particular spin symmetry [108]. Since $\hat{H}$ and $\hat{\mathbf{S}}^2$ commute, the ground-state energy can be corrected by considering the lowest state with a eigenvalue of $\hat{\mathbf{S}}^2$.

$$\hat{\mathbf{S}}^2 \Psi^S = S(S+1)\Psi^S \tag{2.30}$$

where $\hat{\mathbf{S}}$ is a total spin operator, that can be defined as summation of the spins of the individual electrons $\hat{\mathbf{S}} = \sum_i^N \hat{\mathbf{s}}_i(s_i)$. Thus for the square of the total spin we get

$$\hat{\mathbf{S}}^2 = \sum_{i=1}^{N}\sum_{j=1}^{N} \hat{\mathbf{s}}(s_i)\cdot\hat{\mathbf{s}}(s_j) = \frac{3}{4}N + 2\sum_{i=1}^{N}\sum_{j=i+1}^{N} \hat{\mathbf{s}}(s_i)\cdot\hat{\mathbf{s}}(s_j) \tag{2.31}$$

As we can see operator $\hat{\mathbf{S}}^2$ couples different electrons, i.e., it is a two-electron operator.

Non-collinear spin density

In collinear case of spin polarised system, there are only two densities $[n^{\uparrow}(r), n^{\downarrow}(r)]$ and exchange-correlation potentials $[E_{xc}^{\uparrow}(r), E_{xc}^{\downarrow}(r)]$ for spin-up and spin-down states, respectively. However, in "non-collinear spin" case [107, 108] the spin axis vary in

space and spin density has a matrix form

$$n^{\alpha,\beta}(r) = \sum_i \frac{\psi^*_{i,\alpha}(r)\psi_{i,\beta}(r)}{e^{(\epsilon_i-\mu)/kT}+1} \quad , \tag{2.32}$$

where indices α and β denote a Pauli 2×2-matrix, ϵ_i and $\psi_{i,\alpha}(r)$ are the solutions of the correspondent Kohn-Sham equation

$$\sum_\beta \left[\left(-\frac{1}{2}\nabla + \int \frac{n(r)}{|r-r'|} \right) \delta_{\alpha\beta} + v_{ext}(r) + v^{xc}_{\alpha\beta}(r) \right] \psi_{i,\beta}(r) = \epsilon_{i,\alpha}(r)\psi_{i,\alpha}(r) \quad , \tag{2.33}$$

where $v^{xc}_{\alpha\beta}(r) = \delta E_{xc}[n]/\delta n_{\alpha\beta}(\mathrm{r})$.

Spin-orbit coupling

The energy of the spin-orbit interaction of a many-electron system is commonly written [110]

$$E_{LS} = \sum_{i=1}^{N} \xi(\mathbf{r}_i)\mathbf{l}_i \cdot \mathbf{s}_i \quad , \tag{2.34}$$

where $\mathbf{l}_i$ and $\mathbf{s}_i$ are the orbital and spin angular moments, respectively, of the ith electron and $\xi(\mathbf{r}_i)$ is a spin-orbit coupling constant related to the radial derivative of the potential of the electron i. Adding H_{LS} term to the Eqs. 2.15 and 2.17 gives

$$\left[-\frac{1}{2}\nabla^2 + v_{eff} + \xi(\mathbf{r}_i)\mathbf{l}_i \cdot \mathbf{s}_i \right] \phi_i = \epsilon_i \phi_i \quad , \tag{2.35}$$

and applying the variational principle of Eq. 2.19 gives the spin density and ground state energy. Because $\hat{l}_i \cdot \hat{s}_i = \frac{1}{2}(\hat{j}_i^2 - \hat{l}_i^2 - \hat{s}_i^2)$, where $\hat{j}_i = \hat{l}_i + \hat{s}_i$ and operators $\hat{j}_i^2$, $\hat{l}_i^2$, $\hat{s}_i^2$, $\hat{H}$, and $\hat{l}_i\hat{s}_i$, commute with each other, electronic orbitals ϕ_i must be simultaneously the eigen functions of these five operators.

2.3 Numerical solutions of the Kohn-Sham equations

In order to solve Kohn-Sham equations (2.17) the electron orbitals $\phi_i(\mathbf{r})$ must be represented numerically. There are few methods allowing to do that:

- Basis set methods,
- Finite difference methods, and
- Hybrid methods

The advantage of the basis set method among others is that it is simple, integrals and derivatives may be computed exactly, all matrix elements can be efficiently computed, and it does not prefer one location over another. In this method the Kohn-Sham orbitals $\phi_i(\mathbf{r})$ are expanded in linear combination of some basis functions $u_{ni}(\mathbf{r})$:

$$\phi_i = \sum_n c_n u_{ni} \tag{2.36}$$

where c_n are some coefficients. Two types of basis sets that are the most popular in DFT are:

- Gaussian and
- Plane wave.

The difference between them is that the plane wave basis is combined with the pseudopotential approach (core region is not included) while Gaussian deals with all electrons. In this work for our first principles calculations we use plane wave basis which will be discussed next.

2.3.1 Plane waves

Realistic systems have 10^{20} atoms per cubic millimetre that is unaffordable to treat by any numerical method. However, at this scale the crystal lattices are repeating, thus electrons are in a periodic potential $V(\mathbf{r})$, where $V(\mathbf{r}+\mathbf{R}) = V(\mathbf{r})$ and $\mathbf{R}$ is the Bravais lattice vector. Wavefunctions (Kohn-Sham orbitals) are periodic as well and in accordance to Bloch's theorem it can be expanded in the complete set of Fourier components using plane wave basis $e^{i\mathbf{k}\cdot\mathbf{r}}$,

$$\phi_i(\mathbf{r}) = \sum_n C_n(\mathbf{k}) e^{i\mathbf{k}\cdot\mathbf{r}} \quad , \tag{2.37}$$

where $\mathbf{k}$ is a vector of the reciprocal lattice and $C_n(\mathbf{k})$ are the coefficients of the wavefunctions. Due to the periodicity the summation over infinite number of translations in Eq. 2.37 becomes an integral over the first Brillouin zone

$$\sum_n \Rightarrow \int_{k\in BZ} dk \quad , \tag{2.38}$$

which can be replaced by a weighted sum of discrete points

$$\int_{k\in BZ} dk \approx \sum_k^{BZ} w_k \quad , \tag{2.39}$$

where $w_k = (\phi_k \Delta k)/(\sum_k \phi_k \Delta k) = \phi_k / \sum_k \phi_k$. Thus electron density can be calculated in Brillouin zone as

$$n(\mathbf{r}) = \sum_k^{BZ} w_k \sum_n f_{i,k} |C_n(\mathbf{k})|^2 \quad , \tag{2.40}$$

where $f_{i,k}$ is the occupation of orbitals.

If the atoms are related by symmetry the integration over the whole 1st Brillouin

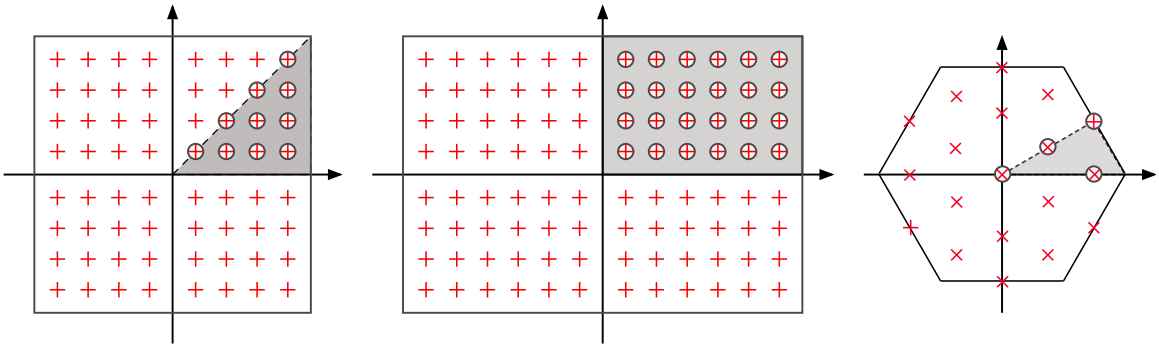

Figure 2.3: Examples of Irreducible Brillouin zones (grey area).

zone can be reduced into the irreducible Brillouin zone (IBZ), see Fig. 2.3,

$$\int_{k\in BZ} dk \approx \sum_{k}^{BZ} w_k = \sum_{k}^{IBZ}\sum_{S} w'_{Sk} \tag{2.41}$$

Unfortunately, a plane-wave basis set is not suitable for the all-electron plane-wave calculations because of the extremely large number of plane waves required to describe accurately the oscillations of the wavefunctions in the core regions, see Fig. 2.4. However, by realising that core electrons do not affect the chemical, mechanical or electronic properties of materials, this problem can be overcome by use of the pseudopotential approximation, that is presented in the next section.

2.3.2 Pseudopotentials

The wavefunctions near the nuclei do not affect the chemical, mechanical or electronic properties very much. Thus to make calculations less costly the strong Coulomb potential of the nucleus and tightly bond core electrons can be replaced by an weaker effective ionic potential (pseudopotential) acting on valance electrons, see Fig. 2.4. The pseudopotential is the result of the screening of the nuclear potential by the core electrons. In such case variation of the wavefunctions near the nucleus is smaller, thus smaller plane-wave cut-off energy can be used in order to reduce the computational time. Within the pseudopotential approach the potential and wave function

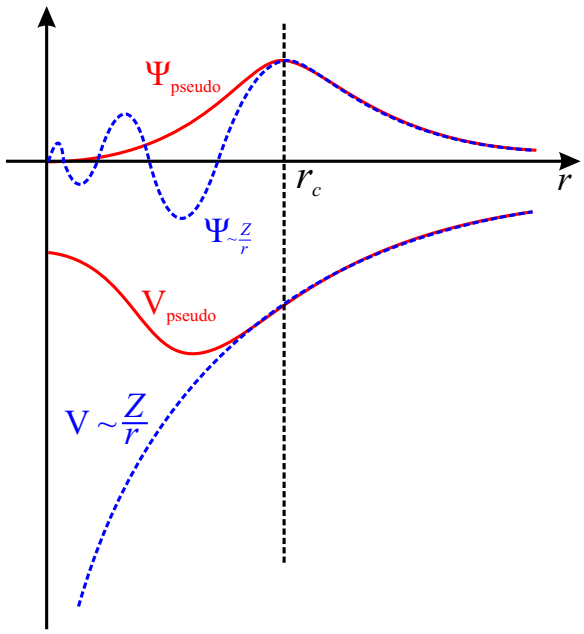

Figure 2.4: Comparison of the all-electron (blue) and pseudo- (red) wavefunctions in the Coulomb potential of the nucleus (blue) and in pseudopotential (red), respectively. The all-electron and the pseudo wavefunction and their potentials match above a certain cutoff radius r_c.

outside the core region match those of the all-electron approach, see Fig. 2.4. More details about pseudopotentials can be found from any DFT textbook, see for example Ref. [111, 112]. In this work we use pseudopotential provided in the VASP package. Also, in order to study magnetic phenomena at some interfaces with strong SOC a full potential FLEUR code was used as well.

2.4 The spin-orbit interaction and crystal field.

In the solid state, there are two important factors effecting the magnetic properties of the individual atoms or ions:

- spin-orbit interaction (SOC) and
- crystal field.

SOC was discussed in a previous section. Before we proceed to the effect of the

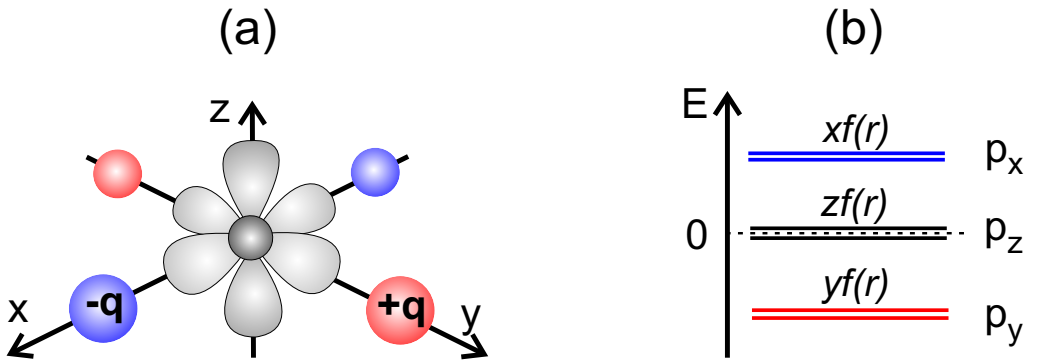

Figure 2.5: (a) Charges along $\pm x$, $\pm y$ create the crystal field for the electron in the p-orbitals. (b) The resulting energy level structure of the p-orbitals.

crystal field on magnetic properties of materials let us first discuss its effect on orbital splitting. As an example consider p-orbitals surrounded by charged ions, see Fig. 2.5. In this case the p_y orbital will be lowered in energy, due to the vicinity of the positive charges $+q$ along the $\pm y$ axes while the p_x orbital will be shifted up in energy, due to the vicinity of the negative charges $-q$ along the $\pm x$ axes. The p_z orbital will be unaffected in energy.

2.4.1 Crystal field and magnetism

Two Hund's rules explain how the electrons have to fill the orbitals and thus determines the total values of their spin and orbital moments. However, they say nothing about the effect of binding environment (crystal field) on total spin and orbital moments.

Effect of the crystal field on a total spin

The crystal field describes the influence of the surrounding atoms and ions on the electron occupation of atomic orbitals. Because magnetism comes from the electronic spin, the number of unpaired electrons in a specific compound indicates how magnetic the compound is. For instance, first Hund's rule states that electrons first fill

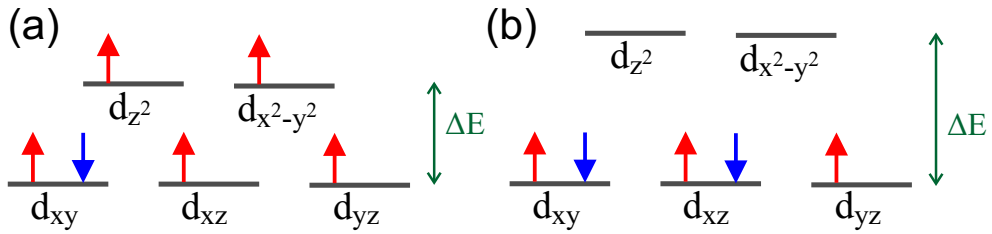

Figure 2.6: Schematic examples of the orbitals fillings in octahedral crystal field depending on a value of the energy splitting ΔE: (a) small ΔE and (b) large ΔE.

all available orbitals with single electrons before pairing up. However, this is only a case when atomic orbitals are degenerate (have equal energies due to homogenous environment). In some complex structures the orbitals are not degenerate and depending on the value of the splitting energy ΔE, Hund's rule might be broken, see Fig. 2.6. For small splittings Hund's rule have place and materials are more magnetic, see Fig. 2.6(a). A large splitting ΔE requires higher energy to place single electrons into the orbitals with higher energy, thus electrons pair first in lower energy orbitals keeping higher energy orbitals empty, see Fig. 2.6(b). In this case structure is less magnetic.

Effect of the crystal field on a total orbital moment

Second Hund's rule says that for a given multiplicity, the term with the largest value of the total orbital angular momentum L has the lowest energy. However, this rule do not explain the dependance of the orbital moment on a magnetization direction in non-homogeneous environment (or in another words the magnetocrystalline anisotropy). To understand how environment effects the orbital moment lets consider two dimensional structure (surface, for example) with the atom bonded to four other atoms with a negative charge as shown in Fig. 2.7. The orbiting electrons in the in-plane orbitals experience a Coulomb repulsion from the negative neighboring ions, Fig. 2.7(a). Therefore, the corresponding out-of-plane orbital momentum is quenched. However, the orbital motions perpendicular to the bonding plane are less disturbed due to the

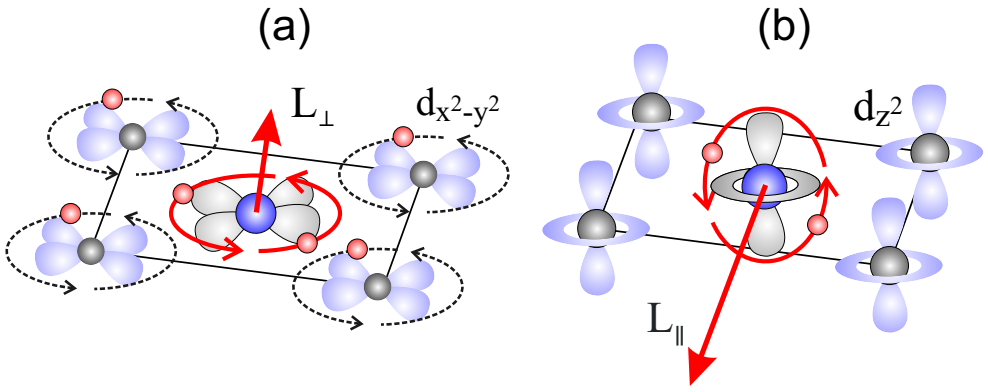

Figure 2.7: Schematic illustration of the directional quenching of the orbital momentum of an atom by crystal field in a thin film geometry for (a) the out-of-plane and (b) for the in-plane magnetization directions.

lack of neighboring ions in out-of-plane direction, see Fig. 2.7(b), and therefore, the corresponding in-plane orbital momentum remains largely unquenched.

2.4.2 SOC vs Crystal field

The Hamilton operator of an electron with orbital momentum L and spin momentum S in a magnetic field B_0 is:

$$\hat{H}_e = \underbrace{-\frac{1}{2}\nabla^2}_{\substack{\text{Kinetic}\\ \text{energy}}} + \underbrace{V_0(r)}_{\substack{\text{Potential}\\ \text{energy}}} + \underbrace{V_c(r)}_{\substack{\text{Crystal}\\ \text{field}}} + \underbrace{\xi \hat{L}\cdot\hat{S}}_{\text{SOC}} + \underbrace{g_L\mu_B B_0\cdot\hat{L}}_{\substack{\text{Orbital Zeeman}\\ \text{interaction}}} + \underbrace{g_S\mu_B B_0\cdot\hat{S}}_{\substack{\text{Spin Zeeman}\\ \text{interaction}}} \tag{2.42}$$

To find the ground state of the system described by this hamiltonian the perturbation theory is needed. In Table 2.1 are shown the relevant energy scales for the hamiltonian in Eq. 2.42. As we can see from the Table 2.1 the magnetic moment is always a small perturbation on the electronic problem. Thus the magnetic properties have to be studied by perturbation methods after the solution of the electronic structure. This technique is implemented in density functional perturbation theory (DFPT) [113, 114].

Depending on the influence of the crystal field $V(r)$ and the spin orbit interaction

Table 2.1: Energy scales for the electron in magnetic system

Energy type	Energy scale, meV
Kinetic Energy	$1,000$ – $10,000$
Potential energy	$1,000$ – $10,000$
Crystal field	12.5 – 1.25
Spin orbit interaction	1.25 – 250
Zeeman interaction	< 1.25

$\xi L \cdot \hat{S}$, the next cases can be distinguished:

A. Strong crystal field

$$\xi L \cdot \hat{S} << V_c(r)$$

This is a case for light elements such as $3d$-transition metals. In such case the crystal field problem is solved first, and SOC term is treated as a perturbation.

B. Strong spin orbit interaction

$$\xi L \cdot \hat{S} >> V_c(r)$$

This is a case for heavy $4f$- and $5f$-band metals. For such elements, the strength of the SOC ξ is large because inner-electrons are very close to the nucleus, have large kinetic energy and relativistic effects are very important. In such a case total angular momentum $\hat{J} = \hat{L} + \hat{S}$ are taken as basis states and the crystal field $V_c(r)$ is treated as a perturbation.

C. Spin orbit interaction and crystal field are comparable

$$\xi L \cdot \hat{S} \approx \ V_c(r)$$

In this case crystal field $V_c(r)$ and SOC $\xi L \cdot \hat{S}$ terms must be diagonalised

simultaneously.

Chapter 3

First Principles Modelling of Interfaces between Solids with Large Lattice Mismatch

3.1 CoO(111)/Ni(111) interface

In this section we investigate the CoO(111)/Ni(111) interface by first principles calculations, focusing on its structure and stability. To satisfy the approximate 5:6 ration of the CoO and Ni lattice constants, we construct a supercell with 5×5 Co (O) and 6×6 Ni atoms per layer in the bulk regions. For the interface Ni layer and the adjacent Ni layer we consider different configurations and study the binding energy and work of adhesion. We show for an ideal CoO interface terminated by 5×5 O atoms that the structure is more stable if there are 5×5 Ni atoms next to it instead of 6×6 as in the bulk. In addition, we observe that a transition layer with 31 Ni atoms located between the interface 5×5 Ni and bulk 6×6 Ni layers (which partially reflects the structures of both these layers) enhances the stability of the CoO/Ni interface. The electronic and magnetic modifications induced by the interface formation are discussed.

3.1.1 Introduction

The development of magnetic devices based on coupling between a ferromagnet and an antiferromagnet (such as spin-valves [115], metal-oxide-metal tunneling diodes [32], and magnetic recording media [116]) depends strongly on the interfacial magnetic structure. When approaching the nano- and atomic scale, the physical and chemical properties of such devices are strongly affected by the structure of the interface and can be significantly modified. Even if the physical and chemical properties of the involved solids in their bulk form are known, investigation of the interface between them is a real challenge for experiments due to the small dimensions. An effective way to explore many aspects of such interfaces is opened by ab-initio calculations.

Many reported ab-initio studies are related to interfaces with small lattice mismatch between the two solids [117]. Modeling interfaces between compounds with

significant lattice mismatch in first principle investigations simply by attaching the materials to each other would give wrong results because of the induced strain. A large mismatch of the unit cell parameters, for example at an interface between face centered cubic and hexagonal close packed structures, can be dealt with by constructing a supercell that includes different numbers of unit cells of the compounds in the interface plane [118–121]. A main feature of such models is that the structures of the interface layers are chosen to be the same as in the bulk. This means that most of the interface atoms are not located in stable sites, for example hollow sites of the opposite interface layer, but have unrealistic distances to atoms on the other side of the interface. Of course, such a configuration is not stable and the question about the atomic density at the interface becomes eminent.

For our present investigation we choose the prototypical CoO/Ni interface. This interface can be understood as a simplification of the CoO/permalloy interface, which is very attractive since the Neel temperature of CoO is close to room temperature and permalloy has a high permeability, low magnetostriction, and high anisotropic magnetoresistance. Extensive studies have been reported in the literature [39, 122–129]. From the theoretical point of view, the large lattice mismatch between CoO and Ni (about 21%) can be addressed by constructing a supercell with 5×5 CoO and 6×6 Ni unit cells in contact to each other. Going beyond this approximation, we consider in the present work that the structures of the atomic layers around the interface can differ from the respective structures in the bulk regions of the supercell. We construct various possible structures using the hard sphere model and calculate the binding energy and work of adhesion. Analyzing the distances between the atoms at the interface, we search for the most stable structure of the CoO/Ni interface for termination by O.

3.1.2 Computational details

Ab initio calculations are performed in the framework of density functional theory using the plane-wave approach [130–132] with the generalized gradient approximation (GGA) [103] and projector augmented wave pseudopotentials [132, 133] with the electronic configurations O $2s^2 2p^4$, Co $3d^8 4s^1$, and Ni $3d^9 4s^1$. We have verified that a plane-wave basis set with energies up to 400 eV is accurate. Because of the size of our supercells (14.96 Å × 34.44 Å) a Γ-point calculation is sufficent. The density of states (DOS) is calculated with a Gaussian smearing of 0.05 eV. To account for the localization of the $3d$ orbitals in CoO, we consider an onsite Coulomb interaction in the rotationally invariant Dudarev scheme (GGA+U) [134–136] with an effective value of U = 6.1 eV [104, 137]. The $3d$ orbitals of the Ni atoms at the interface are subject to strong Coulomb repulsion if they bond to O (similar to NiO), while towards the bulk Ni we rather have free carriers (similar to bulk Ni). While the GGA works reasonably well for metals, it is known to underestimate the magnetic moments and band gaps in transitional metal oxides. The GGA+U approach can overcome this problem for metal oxides, but is not appropriate for metals. To compensate for this inaccuracy in our calculations, we employ both the GGA and GGA+U methods for the interface Ni atoms and compare the results, whereas the other Ni atoms are always treated in the GGA. The effective interaction parameter for the interface Ni atoms is taken from bulk NiO (U = 7 eV [138]).

3.1.3 Interface models

CoO crystallizes in the NaCl structure type with the Co magnetic moments arranged antiferromagnetically (AFM-II order), while Ni follows the Cu structure type and shows ferromagnetism (FM order). To construct the CoO/Ni interface we choose a (111) orientation for both CoO and Ni, because this surface of CoO is not compensated and the exchange bias is maximal [122]. The lattice mismatch is reduced to less than

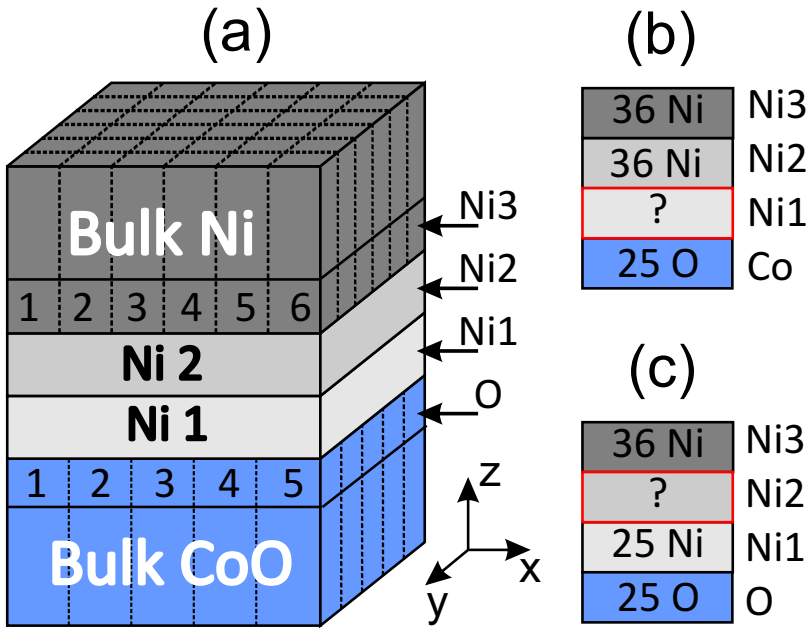

Figure 3.1: (a) (5×5)CoO/(6×6)Ni interface. The vertical lines highlight the Ni and CoO unit cells. The structures of layers 1 and 2 (frist two Ni layers) are unknown with x_1 and x_2 Ni atoms in these layers. (b) The atoms in layer Ni1 occupy hollow sites of the adjacent O layer. (c) The atoms in layer Ni2 occupy hollow sites of the adjacent Ni3 layer.

1% as 5×5 CoO and 6×6 Ni unit cells are put in contact to each other. Perpendicular to the interface (z direction of the supercell) we place 4 CoO layers cells and 5 Ni layers as well as a vacuum spacing of 15 Å thickness, which we find to be sufficient to avoid an interaction across the vacuum. After a volume relaxation of the CoO/Ni supercell, the lattice parameters in the CoO and Ni regions are found to be decreased and increased, respectively, by 0.4% with respect to their bulk values.

While in the bulk regions of our supercell the atoms build a close packed arrangement, the structure of the interface layers and the layers close to the interface may be different, see Fig. 3.1. We assume that the surface of CoO is terminated by a layer of O atoms that has no defects. We consider different atomic configurations for the first two layers of Ni atoms next to the interface (the numbers of Ni atoms in these layers are denoted by x_1 and x_2), focusing on the following two cases: (i) The atoms in the first Ni layer occupy hollow sites of the adjacent O layer, see Fig. 3.1(b). The

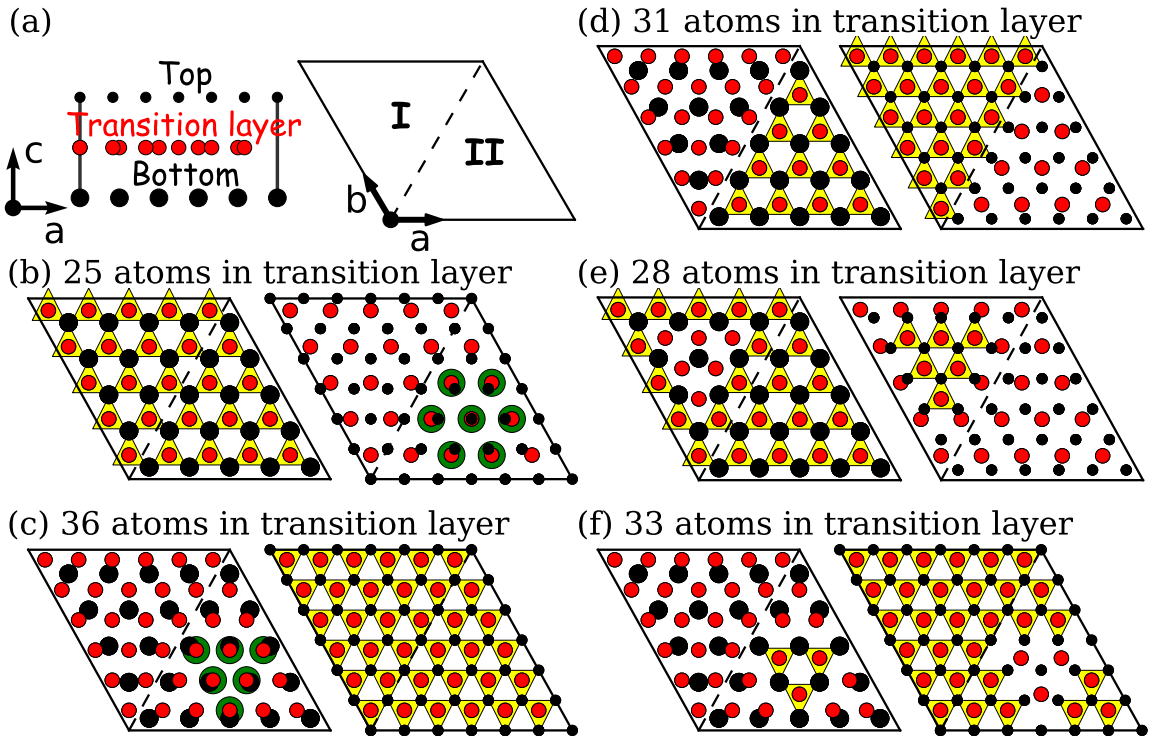

Figure 3.2: (a) The transition layer is located between a top layer with 25 and a bottom layer with 36 close packed atoms. (b)-(f) Possible structures of the transition layer. Yellow (green) background color indicates atoms on hollow (top) sites.

structure of the second Ni layer is not known, while the third Ni layer maintains a configuration of close packed 6×6 Ni atoms. (ii) The structure of the first Ni layer is not known, while the second Ni layer has the bulk structure, see Fig. 3.11(c). The layer with unknown structure located between layers of 25 and 36 close packed atoms is called transition layer. Cases (i) and (ii) describe the location of the transition layer, i.e., between 25 and 36 Ni atoms in case (i) and between 25 O and 36 Ni atoms in case (ii). These structures are justified by the hard sphere model, see Fig. 3.2(a). The bonding around the interface is maximal if the atoms have the same distance to three neighbors on the other side of the interface (threefold hollow sites). Twofold bridge sites are less favorable and top sites are least favorable [118]. We consider the possible structures of the transition layer for which each atom occupies at least one (face centered cubic) hollow site, as indicated in Fig. 3.2 by yellow triangles.

Table 3.1: Numbers of atoms in Ni layers 1 and 2, see Fig. 3.1, for the different models considered for the CoO/Ni interface.

Model	(1)	(2)	(3)	(4)	(5)	(6)	(7)
Layer 1	25	25	25	25	31	33	36
Layer 2	28	31	33	36	36	36	36

For a better understanding, let us divide the interface area of the supercell into the regions I and II as indicated in Fig. 3.2(a). We first consider the case that all atoms in the transition layer occupy hollow sites of one of the surrounding layers, see Figs. 3.2(b) and 3.2(c). In this case the transition layer contains 25 or 36 close packed atoms. Such interfaces are expected to suffer from the non-uniform environments of the interface atoms, which are shifted from the energetically most favorable positions (bridge sites in region I and top sites in region II). The transition layer in Fig. 3.2(d) comprises 31 atoms. In region I they occupy hollow sites of the top layer and in region II hollow sites of the bottom layer. In contrast to the previous two models, here no top sites are occupied, which stabilizes this structure. In Fig. 3.2(e) the transition layer (containing 33 atoms) has more atoms on the hollow sites of the top layer than of the bottom layer, while in Fig. 3.2(f) the majority of the atoms in the transition layer (containing 28 atoms) occupies hollow sites of the bottom layer. We see that top sites can be completely avoided. Applying the introduced configurations of the transition layer and having two possibilities to locate it, we obtain seven structures with different numbers of Ni atoms in the first two layers, see Table 3.1.3. It turns out that the Ni and Co atoms at the interface couple antiferromagnetically and the Ni atoms in the first two layers ferromagnetically for all structures under consideration.

3.1.4 Stable structure. Transition layer

To find the most stable structure among the models in Table I, we calculate the average binding energy for the Ni atoms in the first two layers (which contain $x_1 + x_2$ atoms in total) as

$$E_b = \frac{E_{CoO/Ni} - E_{CoO} - E_{Ni,bulk-like}}{x_1 + x_2} - E_{Ni,atom}$$

where $E_{CoO/Ni}$, E_{CoO}, $E_{Ni,bulk-like}$, and $E_{Ni,atom}$ denote the energies of the full supercell, a supercell with only the CoO region, a supercell with only the bulk-like Ni region, and one Ni atom, respectively. All these supercells have the same lattice parameters. Figure 3(a) shows that configurations (2) and (3) are most stable when we apply the GGA and GGA+U methods for the Ni atoms at the interface, respectively. However, both these methods favor 25 atoms in the first Ni layer, i.e., the second Ni layer is the transition layer; compare Fig. 3.1(b). We observe that the structure of this transition layer is different for the GGA and GGA+U approaches: In the GGA the lowest energy is obtained when there are 31 atoms in the transition layer, see Fig. 3.2(c), while the GGA+U favors 33 atoms, see Fig. 3.2(d).

To understand which of the two methods describes the structural properties of the interface Ni atoms better, we have performed test calculations for bulk Ni and bulk NiO using different values of U (0, 3, 5, and 7 eV). We find that the lattice parameter of NiO does not vary significantly with U, see Fig. 3.3(a). The obtained value of about 2.08 Å is close to the experimental value [138, 139]. On the contrary, the lattice parameter of bulk Ni decreases with increasing U remarkably from 2.49 to 2.43 Å, see Fig. 3.3(b). Therefore, we conclude that the GGA describes the structural properties of the interface Ni atoms better than the GGA+U. Accordingly, the transition layer is predicted to contain 31 atoms.

The tendency of CoO and Ni to contact to each other can be described by the

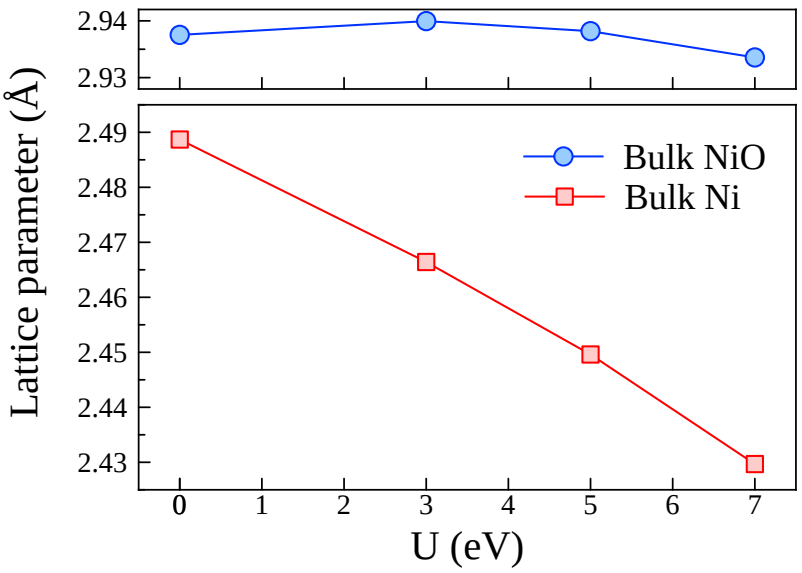

Figure 3.3: Variation of the lattice parameters as a function of U for (a) bulk NiO and (b) bulk Ni.

work of adhesion

$$W_{ad} = \frac{E_{CoO} + E_{Ni} - E_{CoO/Ni}}{A},$$

where E_{Ni} is the energy of a supercell with only the Ni region and A is the area of the interface. The work of adhesion multiplied by the area of the interface is shown in Fig. 3.4(b) for the different models. The highest value is obtained for $x_1 = 25$ and $x_2 = 31$ (using GGA) or $x_2 = 33$ (using GGA+U). These findings coincide with the results deduced from the binding energies. To understand why the (5×5)CoO/(6×6)Ni interface is most stable when there are 25 and 31 Ni atoms in the first two layers, we analyze the Ni-O and Ni-Ni distances. The further an atom is located away from the hollow site of the three atoms in the adjacent layer the smaller is the binding energy. For this reason, we calculate the average deviations of the Ni-O and Ni-Ni distances from the values in bulk NiO and bulk Ni, respectively. We have

$$\Delta = \frac{\sum_{n=1}^{N} \sum_{i=1}^{3} |r_{bulk} - r_i^n|}{3N},$$

where N is the total number of O or Ni atoms in the interface. The results are

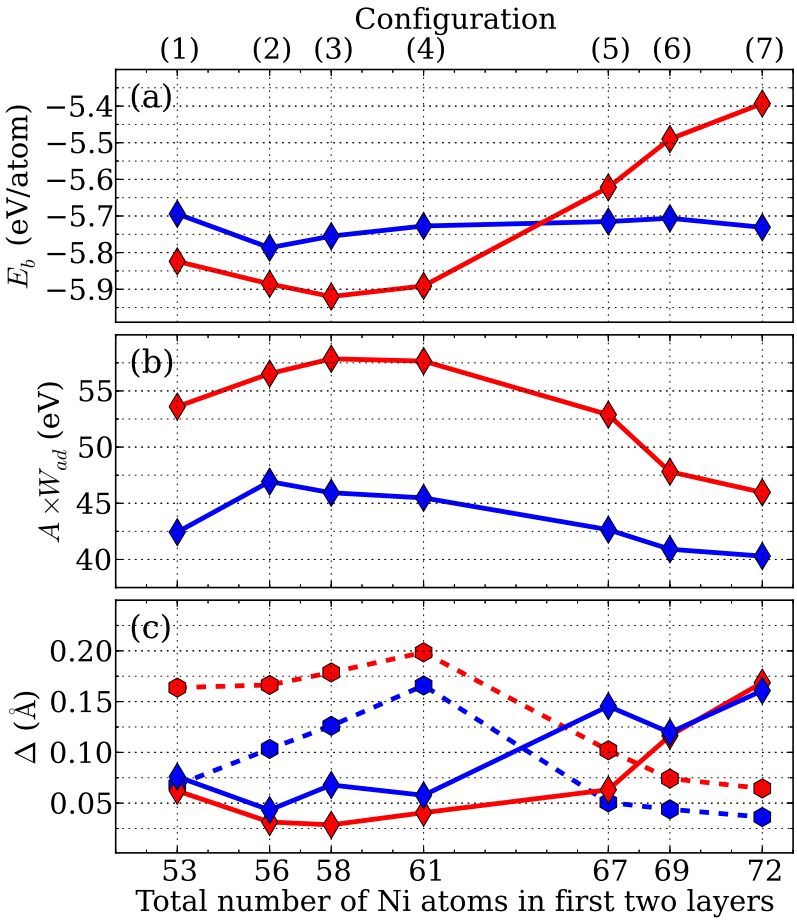

Figure 3.4: (a) Average binding energy per atom in layer 1 or 2 as calculated for the models of Table I. Blue (red) color represents GGA (GGA+U) results. (b) Work of adhesion multiplied by the area of the interface. (c) Average deviations from the bulk values of Ni-O distances (solid) and of distances between Ni atoms in the two sublayers (dashed).

summarized in Fig. 3.4(c). We see that the lowest binding energy (the highest work of adhesion) appears for the structures with the smallest deviations of the Ni-O distances from the bulk value, i.e., for configurations (1) to (4) with 25 Ni atoms in the interface. In contrast, the influence of the Ni-Ni distances is small, which can be explained by the fact that metal-O bonds are stronger than metal-metal bonds. As a consequence, the Ni atoms at the interface replicate that structure of bulk NiO instead of that of bulk Ni. Another important detail that we can deduce from Fig. 3.4(c) is the following: While the number of Ni atoms in the first layer is the same for configurations (1)

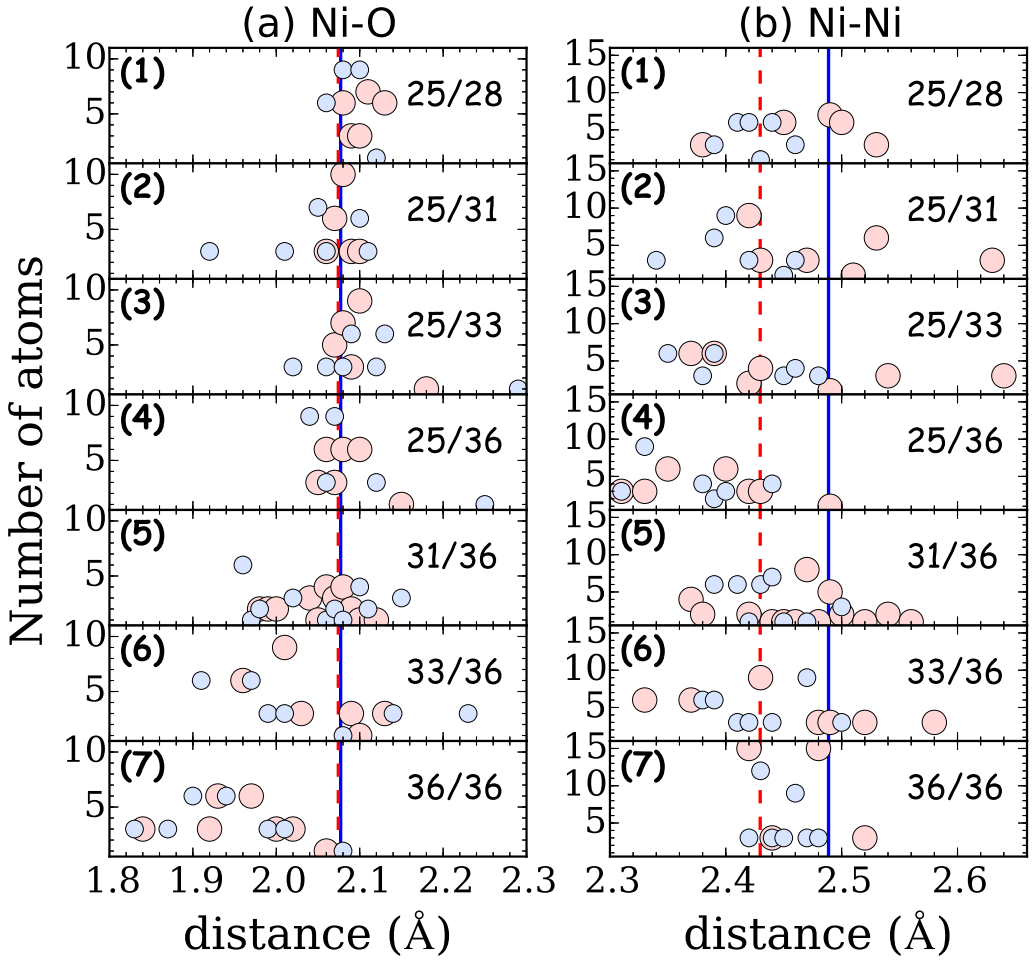

Figure 3.5: Distances between nearest neighbour atoms for models (1) to (7): (a) O and Ni, (b) Ni and Ni. Blue (red) color represents GGA (GGA+U) results. The vertical solid (dashed) lines give the bulk distances obtained for the GGA (GGA+U) method.

to (4), the stability of the interface (in terms of binding energy, work of adhesion, or distances) is determined by the structure of the transition layer. The structure is most stable when there are 31 atoms in the transition layer which occupy partially the hollow sites of both adjacent layers.

In Figs. 3.5(a) and (b) we summarize the obtained distances between nearest neighbour Ni and O atoms as well as between nearest neighbour Ni atoms within the first two layers. We find that the average deviation of the Ni-O (Ni-Ni) distance from the bulk value 2.08 Å (2.49 Å) is minimal when there are 25 (36) Ni atoms in

the interface. Because the binding energy depends strongly on the distance between the atoms, increasing the number of Ni atoms increases the binding energy for Ni-Ni interaction but decrease it for Ni-O interaction. If there are 36 Ni atoms in the interface as in model (7), there are few too short Ni-O distances (about 1.83 Å), which is not realistic. This means that the structure of the Ni layer at the interface cannot be that of the bulk. If there are 25 Ni atoms in the interface as in models (1) to (4), the structure of the transition layer has little influence on the Ni-O distances but results in significant deviations of the Ni-Ni distances: the more Ni atoms the bigger the deviations. For example, in model (4) we have a lot of short distances between Ni atoms (three times 2.31 Å and nine times 2.33 Å), while for model (2) there are only three short distances of 2.34 Å. We notice that the GGA+U method generally results in smaller variations of the Ni-O distances, whereas the GGA method gives better distances between the Ni atoms. Using this knowledge we can conclude on the properties of the CoO/Ni interface when the CoO region is terminated by Co atoms. As the structural properties of Ni and Co are very similar, the Co atoms at the interface will occupy O hollow sites and the adjacent Ni layer will be a transition layer with 31 atoms.

3.1.5 Impact of lattice mismatch on the electronic and magnetic properties

Our first principle calculations clearly show that Ni atoms at the O terminated CoO/Ni interface prefer the O hollow sites rather than the Ni hollow sites on the other side. How does this compare to experimental results? Experimentally, there is evidence for oxidation of the first metal layer [125]. For this reason, we compare the electronic structures of the interface Ni atoms of models (4) and (7), which have 25 and 36 atoms in the interface, with the Ni atoms in bulk Ni and bulk NiO, see Fig. 3.6. We find that the Ni electronic structure of model (4) is similar to that of bulk

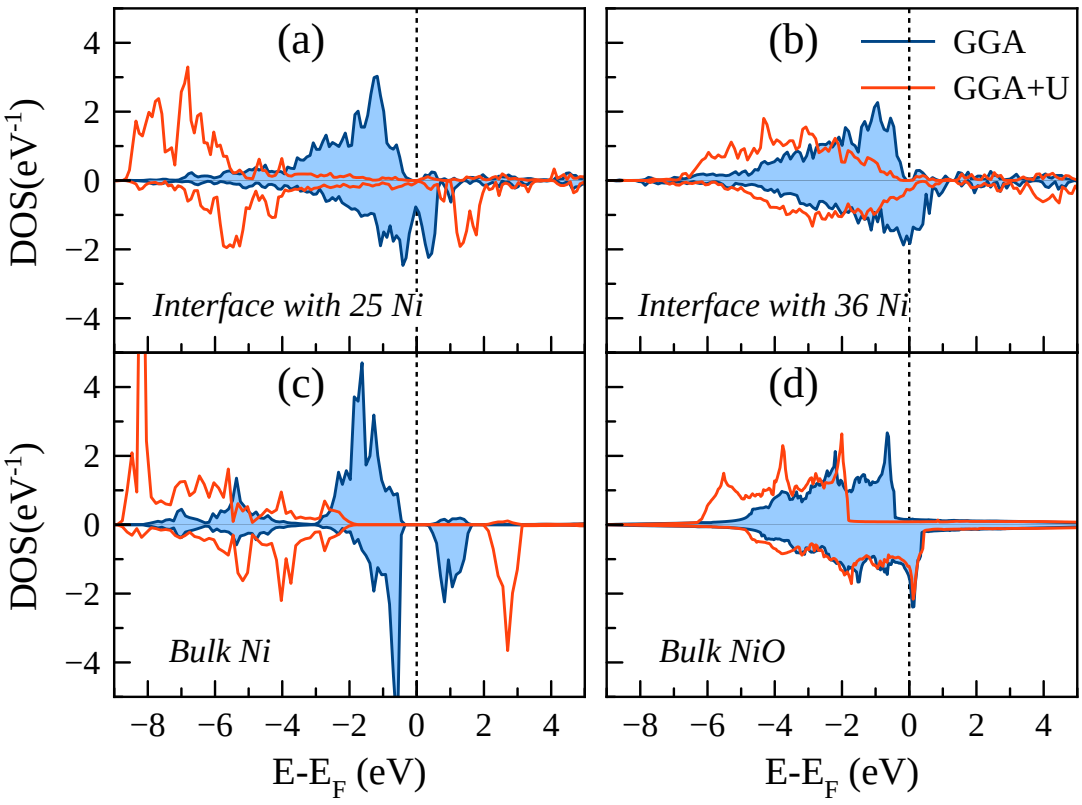

Figure 3.6: Ni DOS: (a) and (b) average over the Ni atoms in the interfaces with 25 and 36 atoms, respectively, (c) bulk NiO, and (d) bulk Ni. Blue (red) color represents GGA (GGA+U) results.

NiO. For 36 atoms each Ni is less oxidized than for 25 atoms, which leads to higher magnetic moments, see Fig. 3.7. According to this figure, the average Ni magnetic moment for the interface with 36 atoms is 0.76 μ_B (GGA) or 0.95 μ_B (GGA+U) and for the interface with 25 atoms 1.07 μ_B (GGA) or 1.62 μ_B (GGA+U). The observed oscillations of the magnetic moments are related to the different surroundings of the Ni atoms.

3.1.6 Summary

In this work we have dealt with the theoretical description of realistic CoO(111)/Ni(111) interfaces. The large lattice mismatch between CoO and Ni has been addressed by a supercell approach with an interface of 5×5 CoO and 6×6 Ni unit cells. Assuming

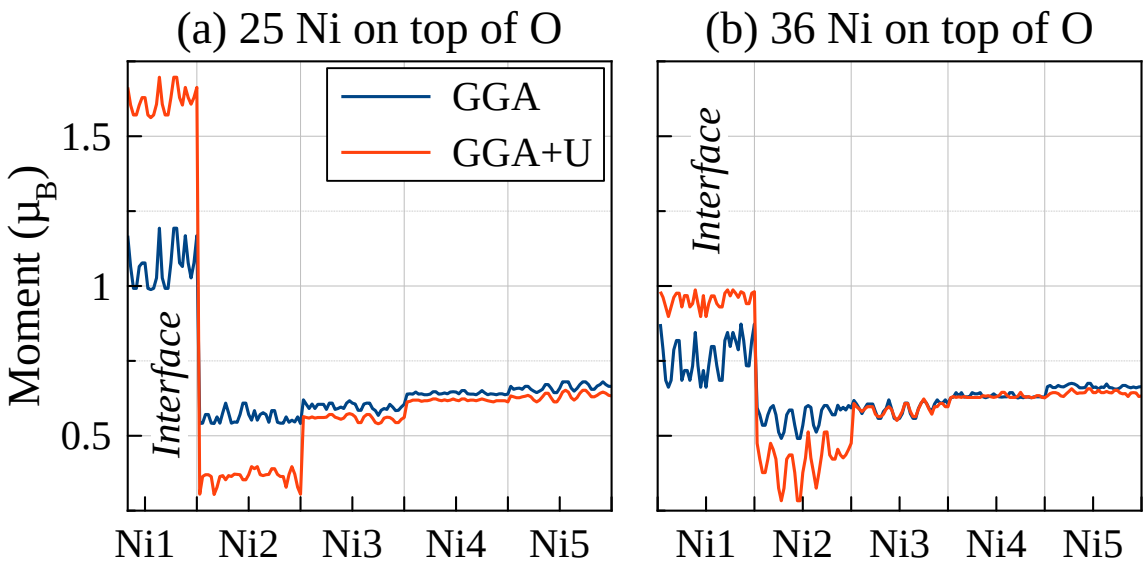

Figure 3.7: Magnetization profile of the Ni atoms for (a) 25 atoms (model (2)) and (b) 36 atoms (model (7)) in the interface. Blue (red) color represents GGA (GGA+U) results. The labels of the Ni layers refer to their distance to the interface.

that the interface Ni atoms and Ni atoms in the next layer occupy at least one hollow site, we have classified the possible configurations of the interface structure. The calculated values of the binding energy and the work of adhesion show that the interface is most stable if there are 5×5 Ni atoms in contact with 5×5 O atoms, instead of the 6×6 atoms as expected from the bulk. The next Ni layer is a transition layer which intrapolates between layers of 5×5 and 6×6 Ni atoms and enhances the stability of the interface if it partially reflects the structures of both these layers. The transition layer is found to optimally comprise 31 Ni atoms. The obtained electronic structures show that the interface Ni atoms become more and more metallic and their magnetic moments decrease when the number of Ni atoms at the interface grows from 25 to 36. The experimental evidence that the interface Ni atoms are oxidized is consistent with our result that there are only 25 Ni atoms in the interface. Moreover, if the CoO is terminated by Co instead of O, the next layer can be expected to be a transition layer with 31 Ni atoms. Our results for the prototypical CoO(111)/Ni(111) interface demonstrate the possible effects of a varying atomic density, i.e., of the optimization

of the chemical bonding, at interfaces between solids with significant lattice mismatch. In real interfaces there is in addition the possibility to have defects, which can modify the picture.

3.2 CoO/Py interfaces

In this section we investigate the magnetic properties of CoO(111)/Py(111) interfaces by first principles calculations. To satisfy the 5:6 ration of the CoO and Py lattice constants, we employ a supercell with 5×5 Co/O and 6×6 Py atoms per layer and optimize the atomic density at the interface. We find that the magnetization in the bulk-like region of the Py (848 emu/cm^3) is compatible with experiment (700 emu/cm^3). While experimentally the magnetization at the interface increases by 14%, we find for the O-terminated and Co-terminated interfaces, respectively, that it decreases by 140% and increases by 40%. This allows us to understand the structure of the real interface with intermixing and O vacancies. We show that the intermixing between the bulk Fe and interface Ni significantly decreases the energy of the interface, enhancing the Fe concentration at the interface. Also, since Co-O bonds are energetically favorable than Ni-O bonds, O diffusion into bulk Py is suppressed.

3.2.1 Introduction

Materials exhibing exchange bias [140] and perpendicular anisotropy are important for ultra-high density perpendicular recording media [4]. Among them the CoO/Py system is very attractive, since the Néel temperature of CoO is close to room temperature and the magnetocrystalline anisotropy is high. Although the physical properties of CoO/Py interfaces have been studied in various experimental works [39, 40], an adequate characterization of the structural, electronic, and magnetic properties on an atomic level is missing. Insight can be obtained from first principle calculations based on density functional theory. However, it is important to notice that a major difficulty in studying interfaces between metals and metal oxides theoretically is the typically large lattice mismatch. Therefore, any calculation employing a coherent model (i.e., assuming that the lattice parameters of the component materials are the

same) will give doubtful results, due to the induced strain.

The only way to avoid this problem is the construction of a large supercell that makes it possible to adjust the lattices of the two compounds [118, 119, 121, 141]. Also, one should take into account that even though the atomic distances in the bulk region of such a supercell should be close to the experimental bulk values the structure at the interface can be different. For example, in Ref. [141] first principles calculations have been employed to establish the variation of the Ni atomic density as compared to the bulk value when approaching the CoO/Ni interface. In addition, the density has been found to change significantly with the type of interface termination. In this context, we study the magnetic properties of the CoO/Py interface due to its technological importance. We particularly explain why experiments find an enhancement of the magnetization at the interface, employing a first principles approach that takes into account the variation of the atomic density in the vicin- ity of the interface. The established mechanism is of general validity for many exchange bias systems.

3.2.2 Interface models and computational details

To deal with the problem of 21% lattice mismatch between CoO and Py we build a supercell that comprises 25 unit cells of CoO and 36 unit cells of Py per layer (in the bulk-like regions) similar to the CoO/Ni interface in Ref. [121], see Fig. 3.8(a). This procedure reduces the lattice mismatch at the CoO/Py interface to less than 0.2%. Since the lattice parameters of Ni and Fe are similar, we can safely assume that the structure of the CoO/Py interface (here Py= Ni_80Fe_20) is similar to that of the CoO/Ni interface. For the latter it has been found that O-termination enforces the atomic density in the first Ni layer to be the same as in the O layer next to it, see Fig. 3.8(b). The reason is that these Ni atoms prefer to resemble the structure of NiO. The second Ni layer turns out to be a transition layer in which atoms occupy hollow

sites of the first Ni layer or of bulk Ni (3rd Ni layer). In the case of Co-termination the first Ni layer is in the contact with Co atoms, see Fig. 3.8(c). Since Co and Ni have similar lattice parameters we can assume that the structures of this layer is similar to that of the 2nd Ni (Py) layer in the O-terminated CoO/Ni interface (first Ni layer in Fig. 3.8(c) and second Ni layer in Fig. 3.8(b)). Moreover, the Ni second layer in the case of Co-termination resembles the structure of bulk Ni see Fig. 3.8(c).

The transition layer comprises 31 Ni atoms located between layers of 5×5 and 6×6 atoms. At the O-terminated interface between 25 and 36 Ni atoms and at the Co-terminated interface between 25 Co and 36 Ni atoms. The importance of the transition layer can be understood from the hard sphere model shown in Fig. 3.9. If the transition layer would have the same structure as either the top or the bottom layer then there would be on-top sites, see Figs. 3.9(b) and (c), with nonphysical (too short) atomic distances. In Fig. 3.9(c) the transition layer has partially the structure of the bottom layer (area II) and partially the structure of the top layer (area I). In fact there are many possible configurations of the transition layer where each atom occupies a hollow site of at least one adjacent layer. However, the most stable of these configurations is that shown in Fig. 3.9(d). To approximate Py = $Ni_{80}Fe_{20}$, we substitute 5, 6, and 7 Ni atoms by Fe in the layers with 25, 31, and 36 atoms, respectively. 5 Py and 4 CoO layers are sufficient to have both the bulk-like regions and the CoO/Ni interface well represented in the supercell. The substitution of Ni by Fe atoms is random and test calculations show that different configurations do not change the average value of the magnetization per layer.

For our first principles calculations we use the Vienna ab-initio simulation package, which is based on the plane wave approach [130, 132, 142]. For the exchange correlation potential we use the generalized gradient approximation (GGA) [103]. In addition, we employ projector augmented wave pseudopotentials [132, 133] with the electronic configurations O $2s^2 2p^4$, Co $3d^8 4s^1$, and Ni $3d^9 4s^1$. We have verified that

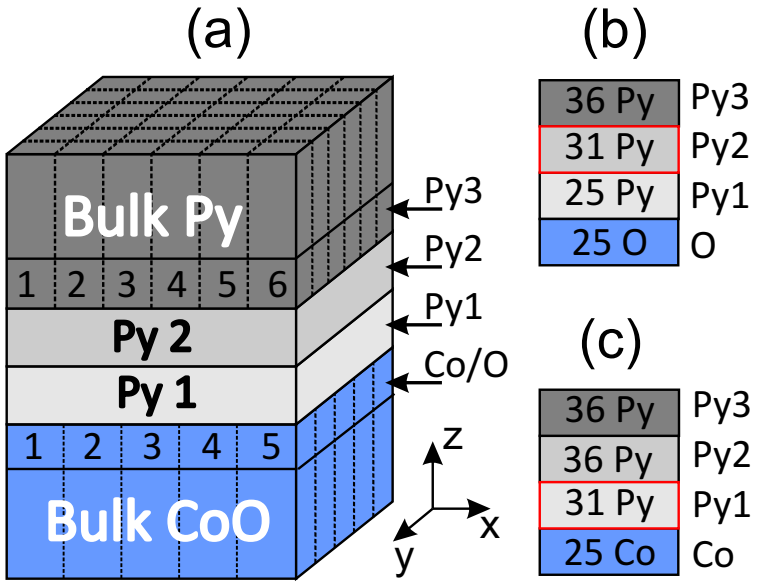

Figure 3.8: (a) (5×5)CoO/(6×6)Ni interface. The structure of the first two Ni layers (Ni1 and Ni2) depends on the termination of the interface: (b) O-terminated and (c) Co-terminated. In (b) the atoms of the first Ni layer occupy the hollow sites of the adjacent O layer. The second Ni layer is a transition layer. In (c) the atoms of the first Ni layer form the transition layer. Both CoO and Ni are [111] orientated.

15 Å of vacuum is sufficient to avoid artificial interaction through the vacuum slab and that a plane wave basis set with energies up to 400 eV is accurate. A Γ-point calculation is sufficient because of the large size of our supercells (14.96 Å × 34.44 Å). Moreover, density of states (DOS) is calculated with a Gaussian smearing of 0.05 eV. To account for the localization of the $3d$ orbitals in CoO, we consider an onsite Coulomb interaction in the rotationally invariant Dudarev scheme (GGA+U) [134–136] with an effective value of $U = 6.1$ eV [104, 137]. The $3d$ orbitals of the Ni and Fe atoms at the O-terminated interface are subject to strong Coulomb repulsion if they bond to O (similar to NiO, FeO), whereas towards the bulk Py rather free carriers dominate. While the GGA works reasonably well for metals, it is known to underestimate the magnetic moments and band gaps in transitional metal oxides. The GGA+U approach can overcome this problem for metal oxides, but is not appropriate for metals. To compensate for this inaccuracy in our calculations, we employ both the GGA and GGA+U methods for the interface Ni and Fe atoms and compare

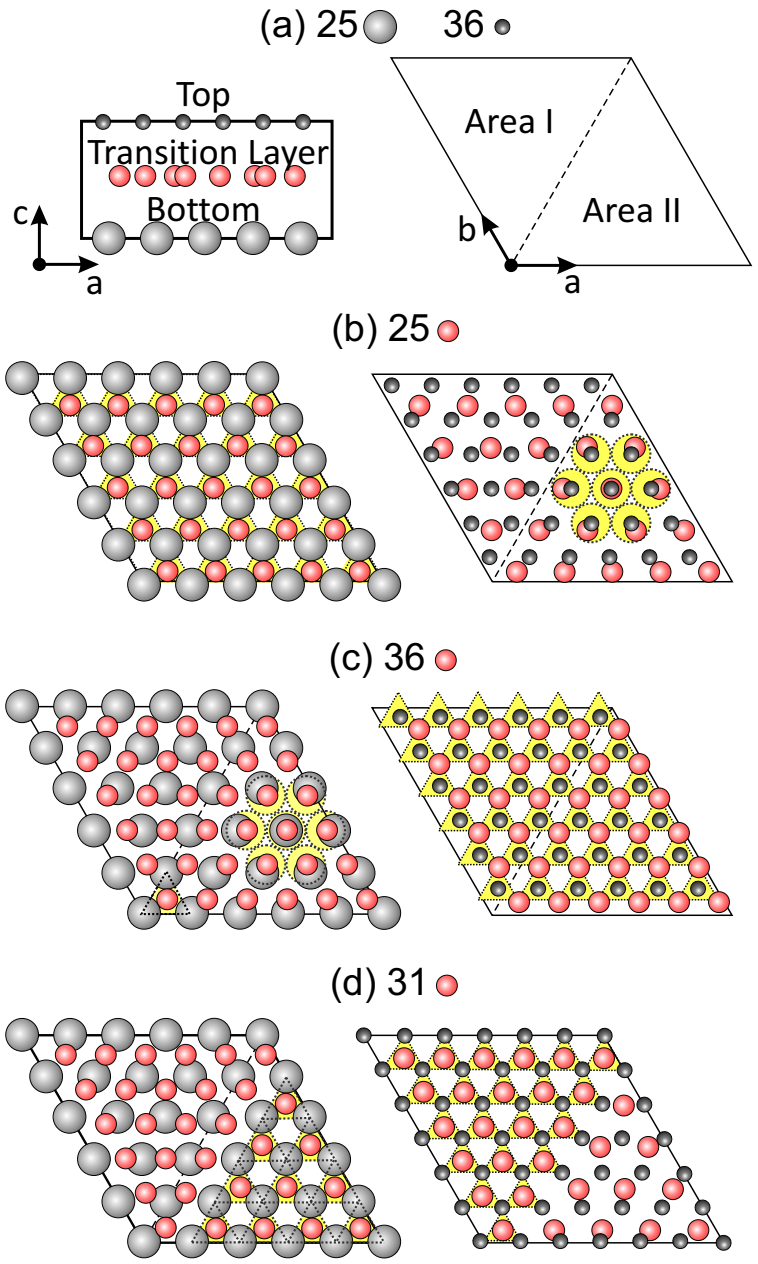

Figure 3.9: (a) The transition layer is located between a top layer of 25 and a bottom layer of 36 close packed atoms. (b)(d) Possible structures of the transition layer. Yellow triangles (circles) indicate atoms occupying hollow (top) sites.

the results, whereas the other Ni and Fe atoms are always treated without onsite interaction. The effective interaction parameter for the interface Ni and Fe atoms is taken from bulk NiO and FeO, respectively [143, 144].

3.2.3 Experimental observations and theoretical extrapolations

In Ref. [39] it has been shown that the magnetization at the CoO/Py interface is 14% higher (800 emu/cm^3) than it is in bulk Py (700 emu/cm^3). In accordance with the theory of magnetic interaction, presence of O at the CoO/Py interface should induce superexchange and thus antiferromagnetic coupling between the Co and Py atoms if the Co-O-Py angle is close to 180°. Large deviations from 180° due to atomic disorder or O vacancies can lead to FM coupling instead. This is the reason why a large lattice mismatch at a metal-oxide interface results in a complex magnetic behavior. Atomic disorder at the interface counteracts superexchange even when there is enough O available. For instance, in Ref. [40] it has been demonstrated that only 10% of the Co spins at the CoO/Py interface are antiferromagnetically coupled to the (ferromagnetic) Py and it has been argued that a significant amount of unpinned Co spins (follows an applied magnetic field) interacts ferromagnetically with the Py. This ferromagnetic contributions is a result of the interface disorder.

The optimised structures of the O- and Co-terminated CoO/Py interfaces are idealisations of a real interface with O vacancies or Co-Py intermixing. The reality thus lies somewhere in between the extremal cases. However having understood the behaviour of the ideal interfaces we can extrapolate our knowledge to the real interface. As mentioned before, a difficulty for first principles calculations arises for the interface atoms as they have bonds to the metal atoms on one side and to O atoms on the other side (for example Py at the O-terminated interface or Co at the Co-terminated interface). The repulsion parameter U cannot be defined unambiguously. We thus perform calculations applying both methods (GGA and GGA+U) for the interface atoms and evaluate the magnetic moment as the average value: $M = (M^{GGA} + M^{GGA+U})/2 \pm \triangle M$, with maximum error $\triangle M = |M - M^{GGA+U}|$

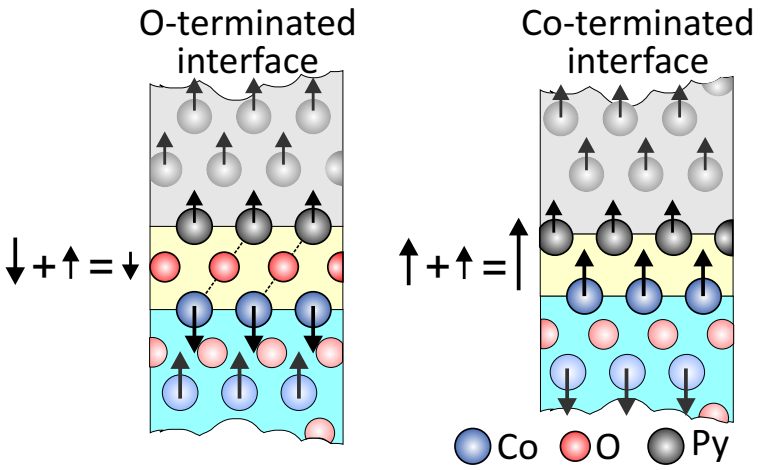

Figure 3.10: Schematic picture of the magnetization directions at the Co-terminated (left) and O-terminated (right) CoO/Py interfaces.

3.2.4 Magnetism at the O- and Co-terminated interfaces

Separating the supercell in interface and bulk-like regions, as shown in Fig. 3.10, it has been demonstrated in Ref. [121] by GGA+U calculations that the bulk Ni magnetization of 558 emu/cm^3 decreases by 36% at the O-terminated interface to -354 emu/cm^3, whereas at the Co-terminated interface it doubles to 1073 emu/cm^3, see Fig. 3.11. Here we substitute 20% of the Ni by Fe for both interface terminations. We find an increased magnetization in the bulk-like Py region of 848 emu/cm^3, see Fig. 3.11. This small discrepancy between theory and experiment (800 emu/cm^3) can be explained by a domain structure in the real system which lowers the overall magnetization with increasing temperature, while our first principle calculations assume a temperature of 0 K.

As compared to the bulk-like Py region the magnetization of Py at the O-terminated interface significantly increases to 1211 ± 142 emu/cm^3, due to the oxidation of the Fe/Ni atoms. Taking into account the magnetization of the uncompensated interface Co atoms (-2636 ± 38 emu/cm^3) we obtain a total magnetization at the interface of 320 ± 66 emu/cm^3, which is 62% smaller than in a bulk-like Py. As we can see from Fig. 3.11, the O-terminated interface shows an antiferromagnetic coupling between

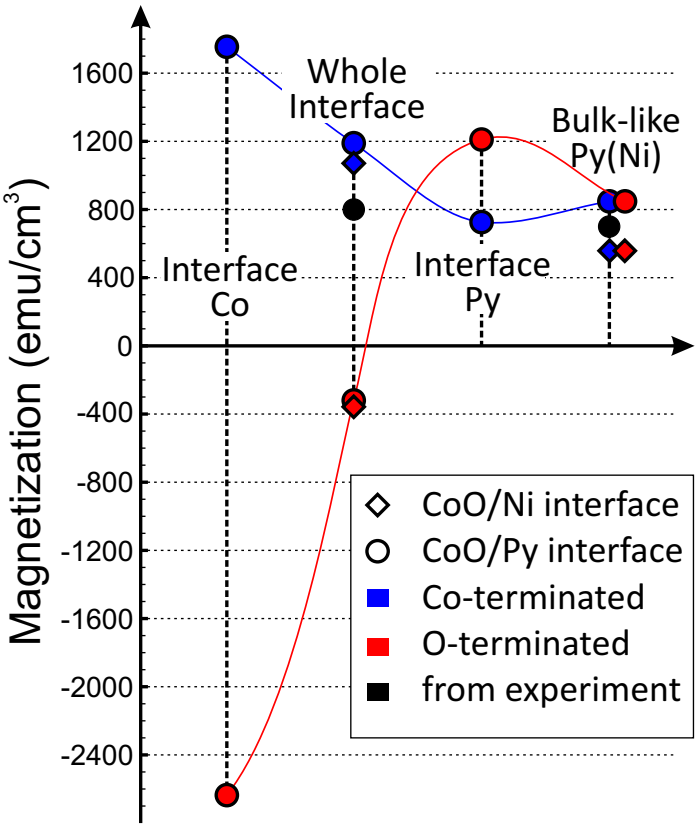

Figure 3.11: (a) Magnetization obtained for CoO/Py and CoO/Ni (Ref. [121]), and experimental value (Ref. [39]). Error comes from the interface atoms for which repulsion parameter is unknown.

the Co and Py atoms. The interface magnetization is oriented in opposite direction as compared to the bulk-like Py region, since the magnetic moments of the Co atoms directly at the interface are larger than those of the Py atoms.

At the Co-terminated interface the Co atoms are less oxidized (1755±171 emu/cm^3) as compared to the O-terminated interface, since O atoms are located only on one side. The magnetization of the interface Py layer is 726 emu/cm^3 and this is slightly smaller than in the bulk-like region, since the Py atomic density decreases towards the interface. The magnetization of the Co-terminated interface is 1189±31 emu/cm^3 and thus 40% higher than in the bulk-like Py region. The magnetization of bulk CoO is zero, as CoO is an antiferromagnet. If we use for the orbital moments of Co, Ni, and Fe the values for their oxides (1.24 μ_B for Co [145], 0.29 μ_B for Ni [146], and 0.88

μ_B for Fe [147]) the magnetization of the O-terminated interface decreases to 165 ± 64 emu/cm^3 and that of the Co-terminated interface increases to 1607 ± 21 emu/cm^3.

3.2.5 Realistic interface as mixture of O- and Co-terminated model interfaces. Intermixing

While the calculated magnetization of bulk Py is comparable to the experimental value, the magnetizations obtained for the two interfaces (O-terminated and Co-terminated) are very different. The O-terminated interface shows an antiferromagnetic coupling between the Co and Py atoms and the Co-terminated interface turns out to be ferromagnetic. This fact implies that a realistic interface is neither O-terminated nor Co-terminated but rather a mixture of those two extreme cases. For instance, the O vacancies in a real CoO/Py interface lead to both Py-Co and Py-O-Co bonding at the same time, where Py atoms in contact with Co or O will have opposite spin directions. Co atoms in contact with Py will have a slightly reduced magnetic moment ($2.66\mu_B$) than those in contact with O ($2.76\ \mu_B$) but with the same direction as Py atoms. Hence, the magnetization is expected to grow with the number of O vacancies.

Another reason for this discrepancy between experiment and model is the intermixing between interface atoms. Our calculations show that such an intermixing of the interface Fe and Co atoms lowers the total energy of the system by 0.14 eV/atom, while an intermixing of the interface Ni and Co atoms increases the energy by 0.33 eV/atom, see Fig. 3.12. Interestingly, we obtain a large reduction of the total energy (0.73 eV/atom) when there is an intermixing between the Fe atoms of bulk-like Py and the interface Ni atoms. Thus, there is an incentive to increase the Fe concentration at the CoO/Py interface. This observation can be explained in terms of the electronegativity, which is lowest for Fe (1.83 eV), medium for Co (1.88 eV), and highest for Ni (1.91 eV). As a consequence, the bonds between the Fe and O

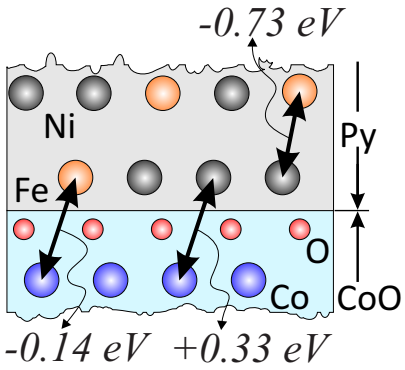

Figure 3.12: Changes of the CoO/Py interface energy by intermixing.

atoms are stronger than those between the O and Ni or Co atoms. We can conclude that at the CoO/Py interface those processes are energetically favorable that create additional Fe-O bonds: (1) Fe-Co intermixing and (2) intermixing of the interface Ni and bulk-like Fe atoms. Also, since bulk Co has a higher oxidation energy than bulk Ni and the amount of Fe atoms in Py is small as compared to Ni, diffusion of O atoms from CoO into the bulk-like Py region is less probable.

3.2.6 Summary

In conclusion, a supercell containing different numbers of CoO and Py unit cells (in order to reduce the lattice mismatch) and a transition layer of intermediate atomic density is reasonable to correctly describe the bulk-like regions of the CoO/Py interface. However, when one approaches the interface itself the experimental and calculated values of the magnetization deviate considerably. For instance, while experiment demonstrates the bulk-like Py region magnetization of 700 emu/cm^3 increases to 800 emu/cm^3 at the interface with CoO Ref. [39] and 90% of its Co atoms are coupled ferromagnetically to Py atoms, our calculations show that bulk-like Py region magnetization of 848 emu/cm^3 decreases to 320$\pm$66 emu/cm^3 at the O-terminated interface due to the AFM coupling, and increases to 1189 $\pm$31 emu/cm^3 due to ferromagnetic coupling at the Co-terminated interface. This discrepancy indicates the presence of

O-vacancies and interface intermixing as to be expected for finite temperature. The above mentioned magnetizations for two interfaces (O- and Co-terminated) clearly show that the increasing of the O-vacancies will increase interface magnetization from -320 to 1189 ± 31 emu/cm^3. At the same time, our result indicates a small probability of the O diffusion into bulk-like Py region, but high chances for the Fe atoms to be localized at the interface. Understanding of the thermal processes leading to the interface disorder would be welcome and could be realized by molecular dynamics simulations. However, this approach requires an enormous amount of computational resources due to the significant lattice mismatch that needs to be taken into account.

3.3 Au/Co and Pt/Co interfaces

In this section we investigate the structural and magnetic properties of the Pt/Co and Au/Co interfaces. For our first principles calculations we reduce the lattice mismatch to 0.2% by constructing Moiré supercells. Our results show that the roughness and atomic density, thus the magnetic properties, depend strongly on the substrate and thickness of the Co slab. An increasing thickness leads to the formation of a Co transition layer at the interface, especially for Pt/Co due to strong Pt-Co interaction. A Moiré supercell with transition layer is found to reproduce the main experimental findings and thus turns out to be the appropriate model for simulating magnetic misfit interfaces.

3.3.1 Introduction

Interfaces between $3d$ transition metals and noble metals have fruitful features for many technologically important applications. For example, the perpendicular magnetic anisotropy of Pt/Co and Au/Co interfaces has potential in logic [62, 148] and memory [27] devices. Exciting properties (e.g., optical, electrical, and catalytic) of systems built of magnetic and non-magnetic materials are well known from nanoparticles [149–152]. Despite their potential for applications, the physical properties of magnetic/non-magnetic interfaces, such as the origin of the perpendicular magnetic anisotropy, are not well understood, mainly because they depend on external factors such as the interface quality and the film thickness in thin film geometries. A change of structural details can strongly alter the electronic states, which in turn influences the magnetic properties. For this reason, knowledge about the structure on an atomic level is key for understanding such interfaces.

First principles techniques based on density functional theory nowadays are widely used for investigating interfaces. It is often assumed that the lattice parameters of the

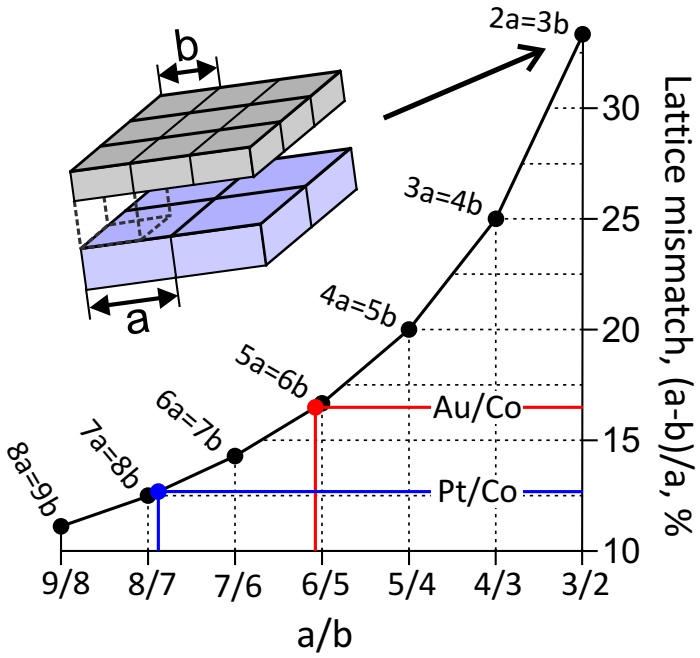

Figure 3.13: (Color online) Relationship between lattice mismatch and Moiré pattern. Red and blue circles indicate the lattice mismatch of the Au/Co and Pt/Co interfaces, respectively. Application of (5×5)Au/(6×6)Co and (7×7)Pt/(8×8)Co supercells reduces the lattice mismatch to 0.2%.

component materials are the same (coherent model). However, this approach is valid only for small lattice mismatch, whereas for the Au/Co and Pt/Co interfaces, for instance, the lattice mismatch amounts to 16.5% and 12.7%, respectively, which results in such a strong strain that unphysical results have to be expected. For example, the theoretical study in Ref. [46] is based on ab-initio calculations using a coherent model of the Pt/Co interface. The authors find for the Co atoms a magnetization of 2.08 μ_B, while the experimental value is 1.8 μ_B [47].

A possible way to avoid the problem is the application of supercells in that the two component materials form a Moiré pattern, see Fig. 3.13. In fact, such patterns have been observed experimentally in a wide range of interfaces, such as graphene/Ir [48, 49], Au/Co [50, 51], Pt/Co [52], FeO/Pd [53], FeO/Pt [54], and Fe/MgO [55]. By means of Moiré supercells the strain on the component materials can be reduced significantly. For example, in (5×5)Au/(6×6)Co and (7×7)Pt/(8×8)Co supercells

the lattice mismatch is reduced to 0.2%. It could be further reduced by using even larger supercells, but with the number of atoms the computational demand of first principles calculations grows dramatically.

While the supercell approach enables us to describe the physical properties in the bulk-like regions properly, the interface itself remains an issue. Does the structure really resemble the bulk-like regions, as assumed by standard Moiré supercells? For example, in Ref. [141] it has been demonstrated that the structure of the first two Ni layers at the CoO/Ni interface differs significantly from that of bulk Ni and that the electronic and magnetic properties are modified accordingly. The objective of the present work thus is to understand in detail the structures and resulting magnetism at Au/Co and Pt/Co interfaces as function of the thickness of the Co slab.

3.3.2 Interface models and computational details

The growth of a thin film on a substrate is determined by the interaction between the substrate and the adatoms. If this interaction is stronger than that between the adatoms themselves, the film will tend to resemble the substrate structure. In the opposite case if the adatom-adatom interaction dominates, the film will aim to maintain a bulk-like structure, which leads to the formation of islands (the size of which depends on the lattice mismatch). In the first case the atomic densities in the substrate and the film can be expected to be the same and the coherent model therefore can be applied. In the second case, in first approximation, an incoherent structure based on a Moiré pattern will be formed, such that a coherent model will not give correct results. In addition, one has to take into account that the strength of the adatom-adatom interaction can be different for single and few layer films due to the surface tension. Thus, the structure and atomic density at the interface in general can depend on the substrate (in our case Au or Pt) and the film thickness.

To investigate the dependencies for the Au/Co and Pt/Co interfaces we calculate

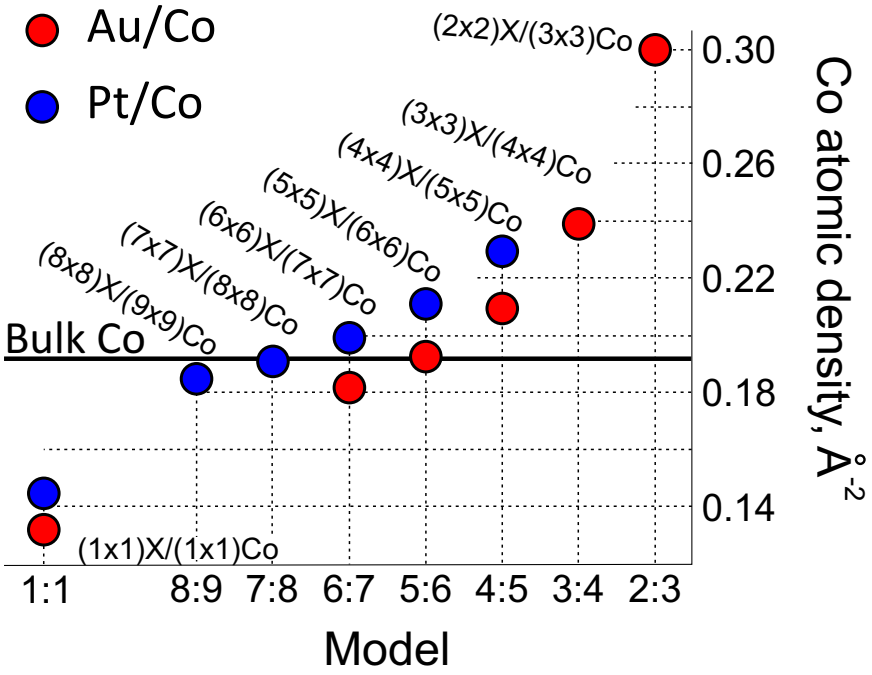

Figure 3.14: (Color online) Dependence of the Co atomic density on the size of the X/Co supercell (X = Au, Pt). The atomic density of X is fixed. A horizontal line indicates the atomic density in bulk Co.

binding energies for supercells with different Moiré patterns, see Fig. 3.14, allowing the Co atomic density to be different while the substrate atomic density is fixed to the bulk value. The figure shows that the 5:6 and 7:8 models for the Au/Co and Pt/Co interfaces, respectively, lead to a Co atomic density similar to the bulk. These models require 25 Au and 36 Co unit cells for Au/Co and 49 Pt and 64 Co unit cells for Pt/Co to reduce the lattice mismatch to 0.2%. In the coherent model the Co atomic density would be too small to derive realistic results. Since the incoherent models contain a huge number of atoms, we perform calculations for periodically repeated slabs of three substrate layers (Au or Pt) and one or four Co layers on top. The bottom of the substrate is terminated by H atoms and a vacuum layer of 10 Å width follows the Co film. In Figs. 3.15(a) and 3.15(b), respectively, the coherent model and an example of an incoherent model are presented. The other models used in our calculations have similar structures at the interface with on-top, hollow, and some intermediate Co sites, with respect to the substrate.

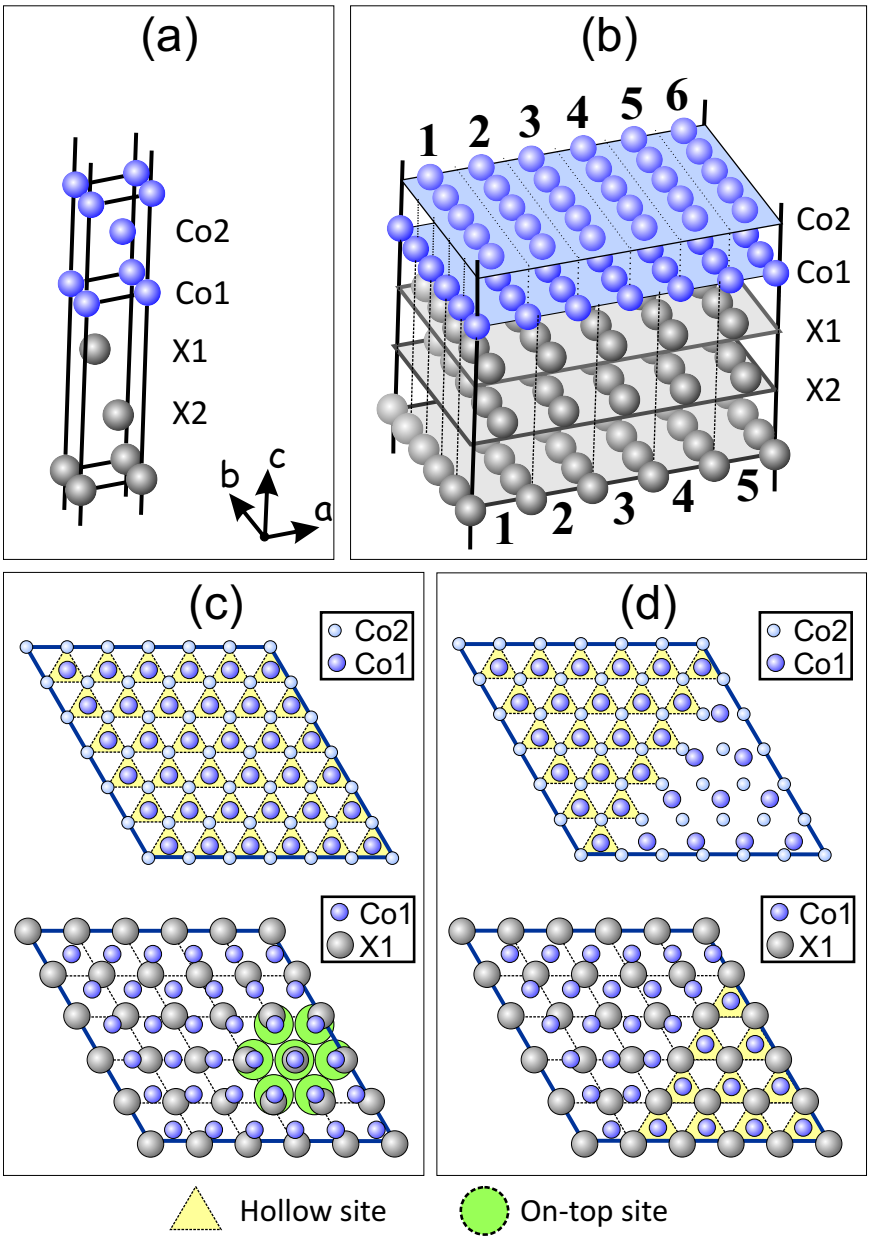

Figure 3.15: (Color online) X/Co interfaces (X = Pt, Au): (a) Coherent model. The atomic densities of X and Co are the same (atoms of the Co1 layer occupy hollow sites of the X1 layer). (b) Supercell containing 5×5 X and 6×6 Co unit cells per layer; top views are shown in (c) and (d). (c) The interface Co1 layer has the same structure as the bulk (atoms of the Co1 layer occupy hollow sites of the Co2 layer). (d) The interface Co1 layer constitutes a transition layer between the substrate X1 layer and next Co2 layer (atoms of the Co1 layer occupy partially hollow sites of the X1 layer and partially hollow sites of the Co2 layer).

If the adatom-adatom and adatom-substrate interactions are of similar strength, we expect the formation of a transition layer that partially reflects the structure of the substrate and partially that of bulk Co. It has been shown in Ref. [141] that shifting of Co atoms from on-top sites, see Fig. 3.15(c), to hollow sites, see Fig. 3.15(d), increases the binding energy (lowers the total energy) significantly. Such a layer is called transition layer and reduces the strain energy. To check this concept for the Au/Co and Pt/Co interfaces we modify the first Co layer in all the above mentioned models, as shown in Fig. 3.15(d) for the (5×5)X/(6×6)Co model. The Co atoms in the transition layer partially occupy the hollow sites of the substrate and partially occupy the hollow sites of the next Co layer, while without transition layer they would occupy only Co hollow sites.

We employ the plane wave pseudopotential VASP ((Vienna Ab initio Simulation Package) in which the Kohn-Sham equations are self-consistently solved by iterative diagonalization and density mixing. For the exchange correlation potential we use the generalized gradient approximation in the Perdew-Burke-Ernzerhof flavor. Tests have been performed for (3×3)Au/(4×4)Co and (5×5)Pt/(6×6)Co supercells with different k-meshes to certify that 6×6×1 and 3×3×1 k-meshes, respectively, are sufficient (differences of about 1 meV).

3.3.3 Stable structures of the interfaces as function of Co thickness

According to Figs. 3.14 and 3.16, the Co structure is very similar to the bulk in the (5×5)Au/(6×6)Co and (7×7)Pt/(8×8)Co interfaces (5:6 and 7:8 models). To address the stability as well as the modifications when more Co layers are added, we calculate the average binding energy of the Co atoms for all models:

$$E_b = \frac{E_{X/Co} - E_X}{N} - E_{Co}^{1atom} \tag{3.1}$$

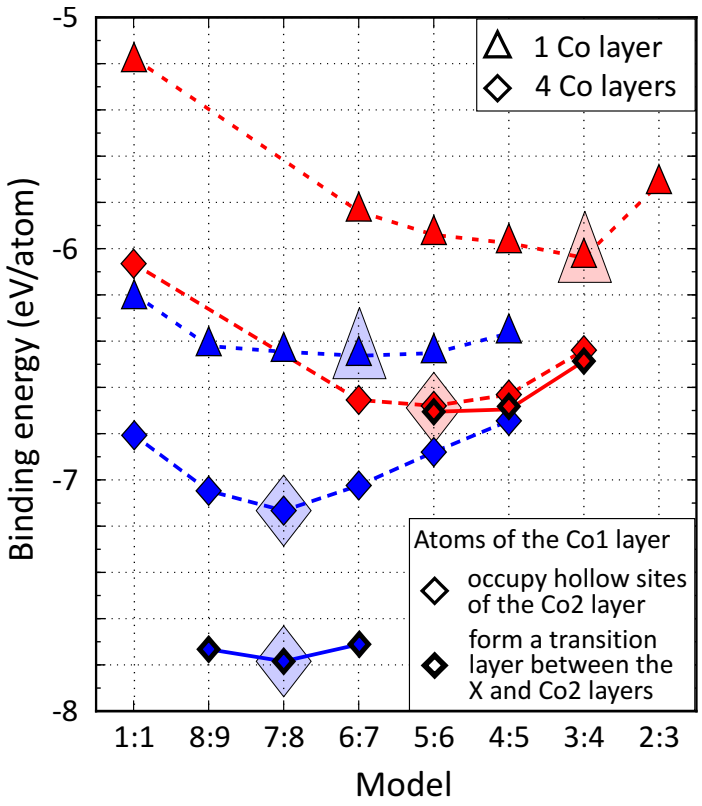

Figure 3.16: (Color online) Dependence of the average binding energy of the Co atoms on the size of the supercell. For more details about the models see Fig. 3.14. Big shaded triangles (diamonds) indicate the most stable models with one four Co layer(s).

where $E_{X/Co}$, E_X, and E_{Co}^{1atom} are the total energies of the full interface, the X substrate, and a single Co atom, respectively. Moreover, N is the number of Co atoms. The results are summarized in Fig. 3.16: Coherent models with one or four Co layers on top of the substrate are unstable due to the large induced strain in the Co region, especially for the Au/Co interface. The Co-Pt coupling is stronger than the Co-Au coupling and the structures are different for one and four Co layers. Adding Co layers modifies the optimal Moiré patterns from (3×3)Au/(4×4)Co to (5×5)Au/(6×6)Co and from (6×6)Pt/(7×7)Co to (7×7)Pt/(8×8)Co.

In the case of one Co layer, the Co atomic density is increased slightly for the Pt substrate (3%) and significantly for the Au substrate (23%). This strong compression is explained by the weak Au-Co coupling. In the case of four Co layers, the most

Table 3.2: Co atomic density at the interface (in $Å^{-2}$) and surface roughness (in 10^{-3} $Å^{-1}$). An asterisk indicates the presence of a transition layer.

Film thickness	Atomic density		Roughness	
	Au/Co	Pt/Co	Au/Co	Pt/Co
1 layer of Co	0.237	0.199	6.72	0.7
4 layers of Co	0.193	0.191	0.26	0.19
4 layers of Co*	0.160	0.167	0.11	0.05
Bulk Co	0.192			

stable models have Co atomic densities close to the bulk value. Moreover, a Co transition layer enhances the binding energy significantly for the Pt substrate due to strong Co-Co and Co-Pt coupling. Because of the latter, the interface Co atoms occupy energetically favorable sites with respect to both the neighbouring Pt and Co layers. For the Au substrate the Co-Au interaction is weak and the Co structure is optimized independently, such that only hollow sites of the adjacent Co layer are occupied. The dependence of the interface Co atomic density on the substrate and number of Co layers is addressed in Table 3.2. In the case of one Co layer, it is higher than in bulk Co, while adding three extra layers reduces it due to the formation of a transition layer.

3.3.4 Surface roughness

Our next goal is to understand how the Co surface roughness depends on the substrate and number of Co layers. The roughness can be estimated as average shift of the surface atoms in the vertical direction:

$$R = \frac{1}{nA} \sum |\Delta z|, \tag{3.2}$$

where Δz is the difference between the average of the vertical positions of all atoms and of the vertical position of a given adatom, n is the number of adatoms in the supercell, and A is the area of the basal plane of the supercell. Results are given for the most stable structures in Table 3.2, and graphical illustrations of the surface roughness are shown in Fig. 3.17. A huge surface roughness is present in the case of one Co layer attached to Au (almost 10 times higher than for one Co layer attached to Pt), because the Co atomic density is large (Table 3.2) due to the weak Au-Co interaction. Keeping the Co atoms in a plane thus would cost much in terms of energy. Increasing the number of Co layers for both substrates to four decreases the Co atomic density at the interface and the surface becomes smoother; compare Fig. 3.17. The roughness decreases dramatically by about 26 times in the Au/Co case, while in the Pt/Co case it decreases only by 4 times.

Moreover, the presence of a Co transition layer at the interface decreases not only the interface Co atomic density, but also the Co surface roughness (Table 3.2): For Pt/Co, the surface becomes smoother by 4 times and for Au/Co by 2 times, as compared to the situation without transition layer. This is another reason why the transition layer stabilizes the structure more in the former than in the latter case. In the experimental Refs. [50, 51], for Au/Co, it was shown that the Co corrugation ($z_{max} - z_{min}$) is 1.75 Å, which is close to our calculated value of 1.94 Å. In addition,the experiments in Ref. [52] for Pt/Co interface indicate that the periodicity of the Moiré pattern is 20 Å; we obtain 19.6 Å.

In Ref. [52, 153] it was shown that -layer-by-layer growth of Co on top of Pt(111) in order to relieve induced tensile strain creates partial dislocations (defects) in the first Co layer and a Moiré structure in the second layer with Co in-plane distance close to that of bulk Co. In our work we observe formation of a transition layer for the interface Co at the Pt/Co interface (that can be considered as defect as well) if there is more than 1 layer of Co. Also, we found that in the transition layer majority

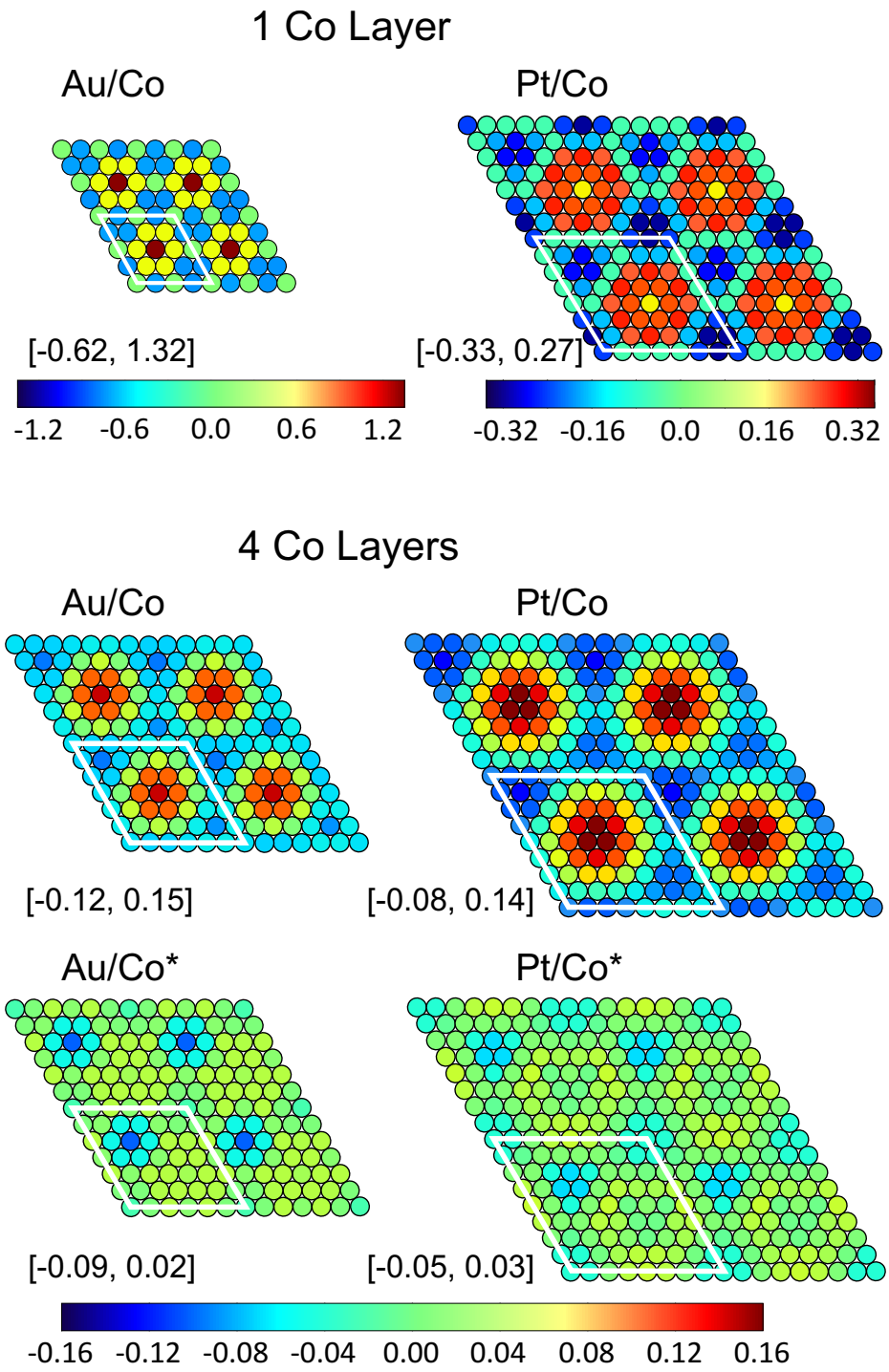

Figure 3.17: Roughness of the Co surface for 1 and 4 Co layers on Au or Pt. The numbers in brackets are the maximal deviations of Co atoms from the average z-value. An asterisk indicates the presence of a transition layer.

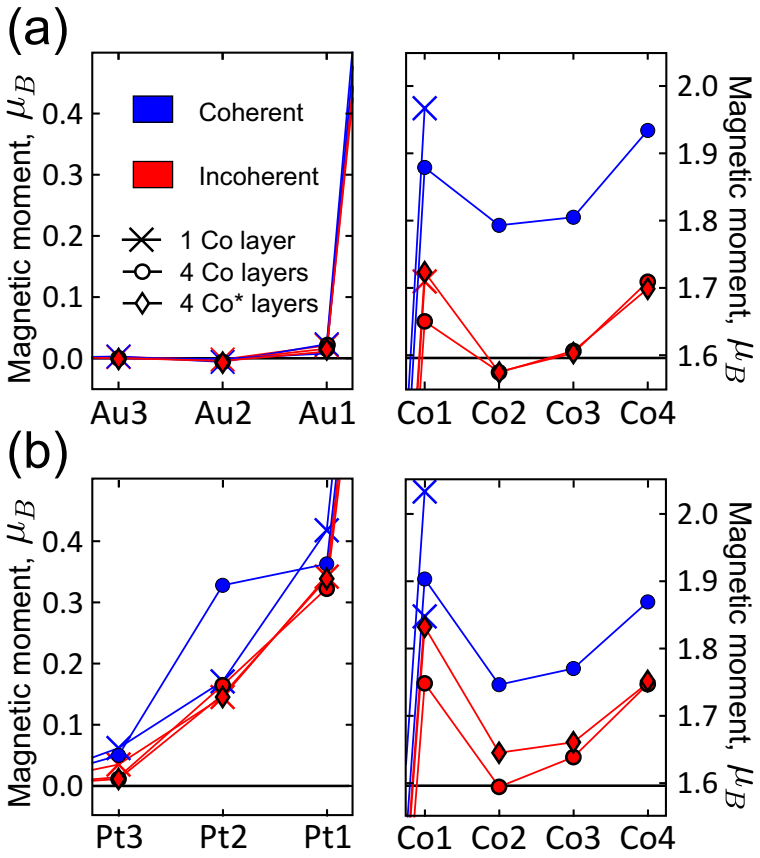

Figure 3.18: (Color online) Average magnetic moment per layer for the (a) Au/Co interface and (b) Pt/Co interface. Vertical black lines indicate the magnetization in the bulk compounds. An asterisk indicates the presence of a transition layer. Au1, Pt1, and Co1 are the interface layers.

of Co atoms occupy the Pt fcc lattice sites while only much smaller number of Co are located on hcp sites that is also in agreement with above mentioned experimental works and more resent one [154]. In the last work was shown that Moiré structure persists up to a coverage of at least 5 ML while in our work we observed it with very small corrugation about 0.1 Å after fourth layer.

3.3.5 Impact of lattice mismatch on magnetic properties of the interfaces

Since the structure depends on the substrate and number of Co layers, the magnetic properties are expected to be different as well. In Fig. 3.18 we present the average

magnetization per layer for the coherent and most stable incoherent models. While the magnetic properties of the noble metals expectedly are, as expected, hardly different, the behaviour of Co depends significantly on the atomic density. First, we notice that the coherent model in each case gives too high magnetic moments, by 0.26 (0.22) μ_B for Au/Co and by 0.19 (0.16) μ_B for Pt/Co in the case of one (four) Co layer(s). Our calculated average magnetic moments of 1.83 μ_B for the interface Co1 layer and of 1.64 μ_B for the bulk-like Co2 layer of the Pt/Co system are very close to the experimental values (1.8 μ_B and 1.58 μ_B, respectively [47]). Due to spin polarization of the interface Pt atoms, the interface Co atoms in Pt/Co have higher magnetic moments than in Au/Co. Adding Co layers decreases the magnetic moment at the interface if no transition layer is formed, while formation of such a layer decreases the Co atomic density and thus enhances the magnetization.

3.3.6 Summary

In conclusion, the lattice mismatch between Co and Au or Pt modifies the structure and magnetic properties of an interface significantly, demonstrating that the coherent model will not give valid results. The same applies to the standard supercell approach with constant atomic density in the Co slab. We therefore propose a model based on a Moiré pattern that includes a Co transition layer at the interface and demonstrate that it gives results very close to the experimental situation. Depending on the substrate and thickness of the Co film, the Co atomic density near the interface is different. While the atomic density and surface roughness for a single Co layer on top of Au are found to be large, due to the weak Au-Co and strong Co-Co interaction, additional Co layers result in lower atomic density and surface roughness. A very similar thickness dependence is observed for Pt/Co, for which an increasing thickness additionally causes the formation of a transition layer. In this layer the atoms partially occupy energetically favorable sites of both the neighboring Pt and Co layers. Formation

of a transition layer in Au/Co results only in a small stability gain, since the Au-Co interaction is weaker than the Co-Co interaction. As the interface magnetic properties depend substantially on the employed model, our result demonstrate that a careful selection is critical. The proposed Moiré supercell with transition layer turns out to give excellent results.

Chapter 4

Impact of the Lattice Mismatch, Atomic Intermixing, Surface Oxidation, and Thin Film Thickness an a Magnetic Anisotropy of the Au/Co Interface

In this section we use first principles calculations to study the effects of the 1) Co film thickness, 2) interface intermixing, and 3) surface oxidation on the electronic and magnetic properties of the Au/Co interface. We find in-plane magnetization for an interface with a single Co layer. Adding a second Co layer or including Au-Co intermixing switches the magnetization direction to out-of-plane. In addition, we construct a Moiré pattern to account for the large lattice mismatch between Au and Co. The corrected Co density results in a magnetic anisotropy energy that is about five times larger than that predicted by the popular coherent model. A strong dependence of the magnetic properties on the level of oxidation of the Co surface layer is demonstrated.

4.1 Introduction

The performance of magnetic memory and logic devices can be significantly improved by exploiting the perpendicular magnetic anisotropy [5]. For example, $3d$ transition metals deposited on non-magnetic $5d$ noble metals result in a very strong anisotropy [6]. Magnetic switching in $5d/3d$ multilayer structures used for GMR can be achieved by spin transfer torque [10, 11]. Also, an electric current at such interfaces can induce a spin current [12] due to the spin Hall effect [13] and can generate a spin density [14] as a result of Rashba effect [15]. Those effects, respectively, generate spin transfer [10, 11] and spin orbit [8] torques that leads to either magnetization reversal [16] or magnetization auto-oscillations [17]. For example, magnetic switching based on spin orbit torque has been observed in ultrathin Co layers interfaced with Pt [18, 19]. Large antisymmetric exchange (interfacial Dzyaloshinskii-Moriya interaction) obtained at the interfaces between heavy metals and transition metal ferromagnets, results in nanoskyrmion lattices [20–23] or helix spins [24, 25]. In addition, spin transfer torque induced by spin-polarised current at the $5d/3d$ interfaces can move domain walls [19, 26]. This effect could reduce the energy needed to store and retrieve one bit of data by a factor of 10,000 and thus it enables new concepts for memory and logic devices [27, 28].

$5d/3d$ interfaces also enable the manipulation of the magnetism via an electric field [29], require no charge transfer, provide high speed data transmission in miniature components, and solve problems of overheating and material degradation in traditional devices [30, 31]. However, the magnetic properties of such interfaces are very sensitive to internal and external factors. Surface oxidation, film and substrate thickness variations, surface strain and roughness, atomic inter-diffusion, segregation, and various defects arising from lattice mismatch are common phenomena. This is also the reason for many discrepancies between experiment and theory [43–45].

On the other hand, first principles calculations for a defect-free Au/Co interface

with the Co in-plane lattice parameter adjusted to the Au substrate (coherent model) result in in-plane magnetization [56, 57], while experiments point to out-of-plane magnetization [50, 51, 58]. The large lattice mismatch between Au and Co indeed gives rise to a Moiré pattern [50, 51], which is usually ignored in theoretical works due to the huge computational costs. If Co is strained in order to match the Au substrate, the theoretical orbital moments and spins of both components are significantly enhanced as compared to experimental results [155]. Bruno and Renard have demonstrated, using phenomenological models, that the strain due to lattice mismatch induces an effective anisotropy [59]. It also has been shown in Ref. [60] that deposition of Co atoms on Au results in a surface alloy by Co-Au intermixing, which can modifiy the magnetic properties of the interface dramatically. In this work, we therefore study the magnetic anisotropy of the Au/Co interface and determine its dependence on structural details.

4.2 Interface models and computational details

We study Au(111) and place Co atoms on top of face centered cubic (fcc) and hexagonal close-packed (hcp) sites. Specifically, 3 layers of 2×2 or 5×5 Au are covered by 1 to 3 layers of 2×2 or 6×6 Co, see the schematic pictures given in Fig. 4.1. Test calculations reveal that interfaces with 3 and 6 layers of Au result in the same magnetic anisotropy (differences $< 10^{-3}$ meV). Thus, the thinner substrate can be used to reduce the computational costs. To obtain a coherent model we extend the bulk Co lattice parameter by 15% to match the Au bulk value, yielding a (2×2)Au/(2×2)Co interface. This model is also used to study Au-Co intermixing and surface oxidation levels of 25%, 50%, 75%, and 100%. Figures 4.1(b) and (c), respectively, illustrate these cases. A (5×5)Au/(6×6)Co interface, as shown in Fig. 4.1(d), results in a minor compression of Co (0.2% as compared to the bulk value) and is very stable in

accordance with Ref. [155]. We add to our supercells vacuum slabs of at least 10 Å thickness in order to simulate surfaces.

The calculations use the linearized augmented plane wave pseudopotential method of density functional theory in the generalized gradient approximation [103, 132]. Scalar and fully relativistic calculations, respectively, are employed to optimize the interface structure and to determine (self-consistently) the magnetic anisotropy. Plane wave cutoff energies of 400 eV (with oxidation) and 350 eV (without oxidation) are chosen. Furthermore, k-meshes of $16 \times 16 \times 2$ and $2 \times 2 \times 2$ points are used for the structural optimization of the coherent and incoherent models, respectively, and are refined to $24 \times 24 \times 2$ and $4 \times 4 \times 2$ points for the relativistic calculations. The precision of our self-consistent calculations is characterised by the energy difference of successive electronic steps, which is set to 10^{-7} eV and 10^{-5} eV for the coherent and incoherent models, respectively.

4.3 Stability of the interfaces

Before we address the magnetic properties, we first compare the different models in terms of the Co binding energy,

$$E_{\mathrm{Co}}^{\mathrm{b}} = (E_{\mathrm{Au/Co}} - E_{\mathrm{Au}} - E_{\mathrm{O}})/N_{\mathrm{Co}} - E_{\mathrm{Co}}, \tag{4.1}$$

where $E_{\mathrm{Au/Co}}$ is the total energy of the supercell, E_{Au} and E_{O} are the total energies of the Au and O parts of the supercell (calculated by removing the respective other part), respectively, N_{Co} is the total number of Co atoms, and E_{Co} is the energy of an isolated Co atom. Because Au and Co favor different atomic packings, fcc and hcp, respectively, the structure of the Au/Co interface is not obvious. In Fig. 4.2 we show schematic structures with different choices of the Co, Au, and O sites. The Co binding energy is given in Fig. 4.3. Though the equilibrium structure of bulk Co

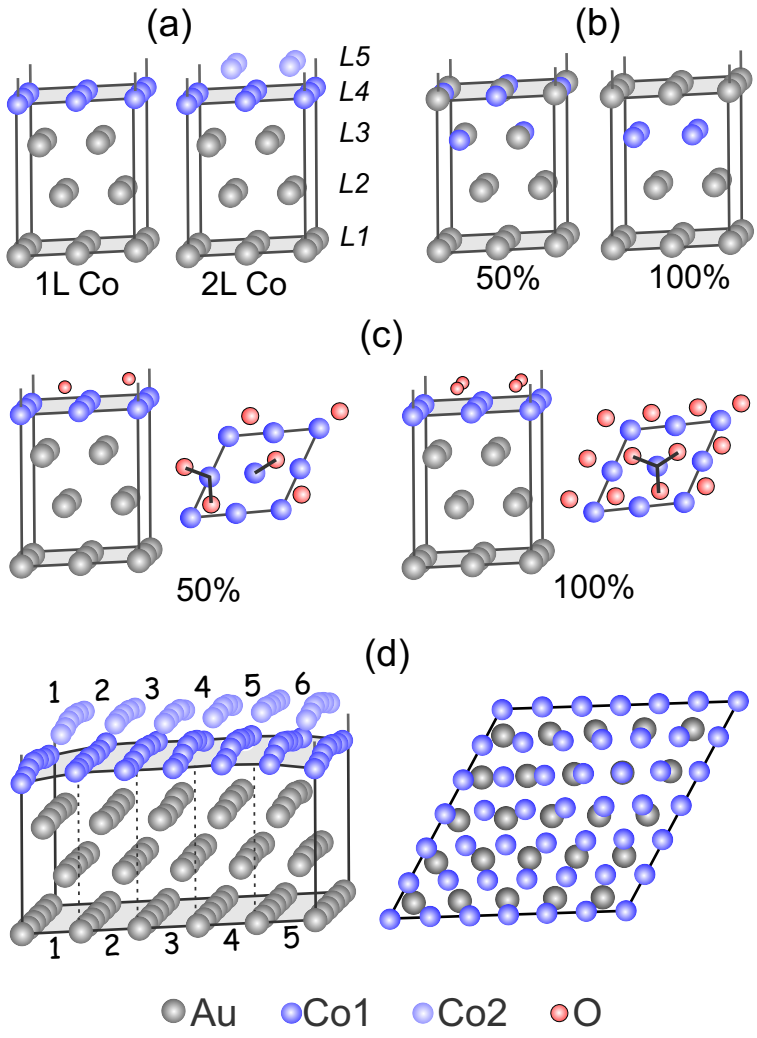

Figure 4.1: Au/Co interfaces: (a-c) coherent model (2×2)Au/(2×2)Co and (d) incoherent model (5×5)Au/(6×6)Co with Moiré pattern. Panel (b) refers to 50% and 100% Au-Co intermixing and panel (c) to 50% and 100% surface oxidation.

at room temperature is of hcp type, Fig. 4.3(a) shows that the interface Co atoms initially follow the fcc structure of Au. However, Co atoms in the second atomic layer occupy hcp hollow sites. Since the energy difference between the hcp and fcc structures is small, both configurations are frequently observed in Co thin films [156]. Also, according to Figs. 4.3(b) and (c), both Au-Co intermixing and surface oxidation cost only a small amount of energy, if the atoms in the uppermost layer occupy hcp instead of fcc hollow sites. Thus, occupation of hollow sites of the two packing types will appear with almost equal probability.

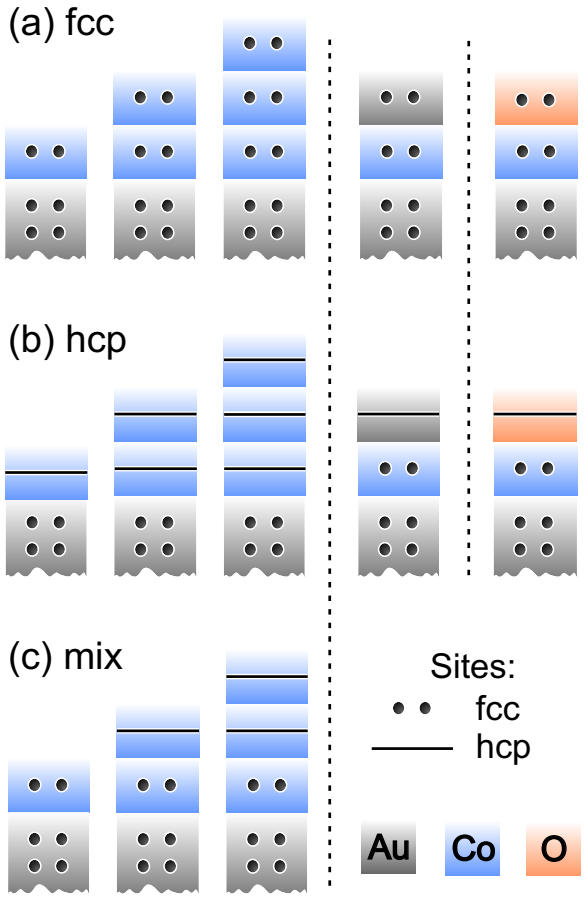

Figure 4.2: Illustrations of the occupied atomic sites at Au/Co interfaces with different numbers of Co layers (left), Au-Co intermixing (middle), and surface oxidation (right).

According to Fig. 4.3, the Co binding energy is higher when (1) a Moiré pattern is formed, (2) the number of Co layers increases, (3) there is Au-Co intermixing, and (4) the surface is oxidized. The Moiré pattern is favorable as the Co-Co distances are much closer to the respective bulk Co value. A thicker Co slab and the inclusion of Au-Co intermixing are favorable as more Co-Co and Au-Co bonds are formed, respectively. Even if elements are immiscible in the bulk they can mix at an interface due to differences in the preferred lattice parameters [157]. Moreover, the fact that a Co surface in atmosphere is subject to oxidation shows already that Co-O bonds are energetically stable.

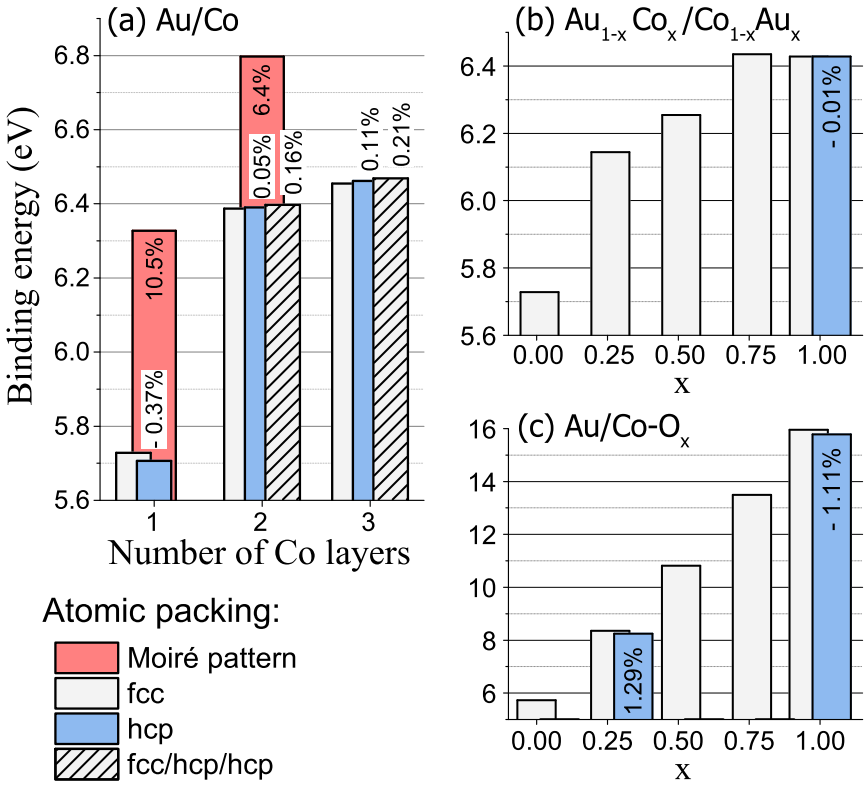

Figure 4.3: Average binding energy per Co atom at the Au/Co interface, depending on the (a) number of Co layers, (b) amount of Au-Co intermixing and (c) amount of surface oxidation. Percentages quantify the energy difference with respect to fcc packing.

4.4 Magnetic anisotropy energy (MAE)

4.4.1 Coupling of the electron orbital moment with spin and crystal field

The magnetic anisotropy energy (MAE) originates from a coupling of the electron orbital motion with spin and with the crystal field. If the crystal field is weak and the spin orbit coupling (SOC) is strong, as in the $5d$ noble metals, the orbital moment is large and rigidly coupled to the spin ($\vec{L}$ and $\vec{S}$ are collinear). In the $3d$ transition metals, on the other hand, the SOC is weak and the crystal field strong, so that $\vec{L}$ and $\vec{S}$ are not necessarily collinear. Since surfaces and interfaces modify the crystal field by the broken lattice periodicity, the interaction between $\vec{S}$ and $\vec{L}$ in $5d/3d$ interfaces

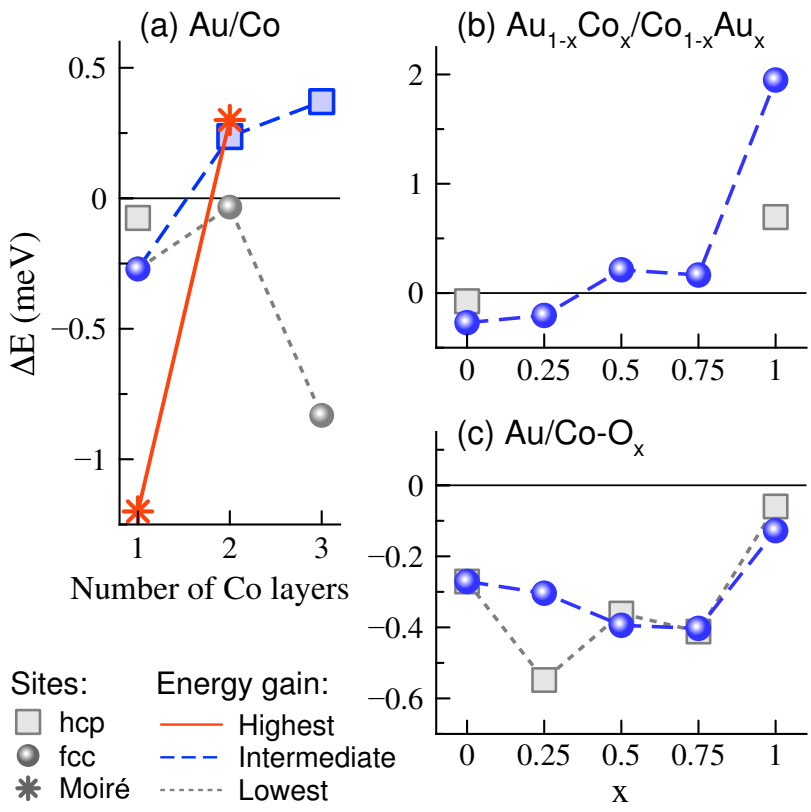

Figure 4.4: MAE (per Au unit cell) for different types of occupied hollow sites and dependence on the (a) number of Co layers, (b) amount of Au-Co intermixing, and (c) amount of surface oxidation. Red (solid), blue (dashed), and grey (dotted) lines, respectively, represent the highest, intermediate, and lowest energy gains. Positive and negative values, respectively, refer to out-of-plane and in-plane magnetic easy axes.

becomes a very complex problem. Additional difficulties arise when imperfections and lattice mismatch play a role.

4.4.2 Calculations of the MAE

We calculate the MAE (energy difference between systems with in-plane and out-of-plane magnetization) per Au unit cell,

$$\Delta E = (E_z - E_x)/N_{\mathrm{Au}}, \tag{4.2}$$

where $N_{\mathrm{Au}} = 4$ or 25, in order to compare the coherent (2×2)Au/(2×2)Co and incoherent (5×5)Au/(6×6)Co models. The energy change for different in-plane magnetization directions is found to be very small (for example, for the coherent model with 1 Co layer we find $|E_z - E_x| \approx 30|E_x - E_y|$), as to be expected, and thus is neglected in the present work. In Fig. 4.4(a) the MAE is depicted as a function of the number of Co layers for occupied fcc and hcp sites as well as for the formation of a Moiré pattern. Figures 4.4(b) and (c) address the effects of Au-Co intermixing and surface oxidation, respectively. In the case of 1 Co layer the MAE for the incoherent models is about 5 (10) times larger than for the respective coherent models with Co atoms at fcc (hcp) sites. We find always in-plane magnetization, as previously reported in Ref. [56]. Adding a second layer of hcp Co switches the system to out-of-plane magnetization, where the coherent and incoherent models show similar absolute MAE values. A third Co layer enhances the out-of-plane magnetization only for hcp stacking, while fcc stacking results again in in-plane magnetization. Incoherent models with 3 Co layers have not been studied due to the large computational costs.

According to Fig. 4.4(b), the system switches from in-plane to out-of-plane magnetization when the Au-Co intermixing reaches 50%. For 100% intermixing (corresponding to an Au/Co/Au structure) and fcc arrangement the absolute value of the MAE is about 5 times larger than without intermixing. In the hcp case the out-of-plane magnetization is maintained and the MAE is reduced to less than half. Moreover, if less than 75% of the fcc hollow sites are occupied by O atoms we have an in-plane magnetization, whereas if all fcc hollow sites are occupied the MAE becomes very small, see Fig. 4.4(c). This dependence will be explained in more detail in the next section.

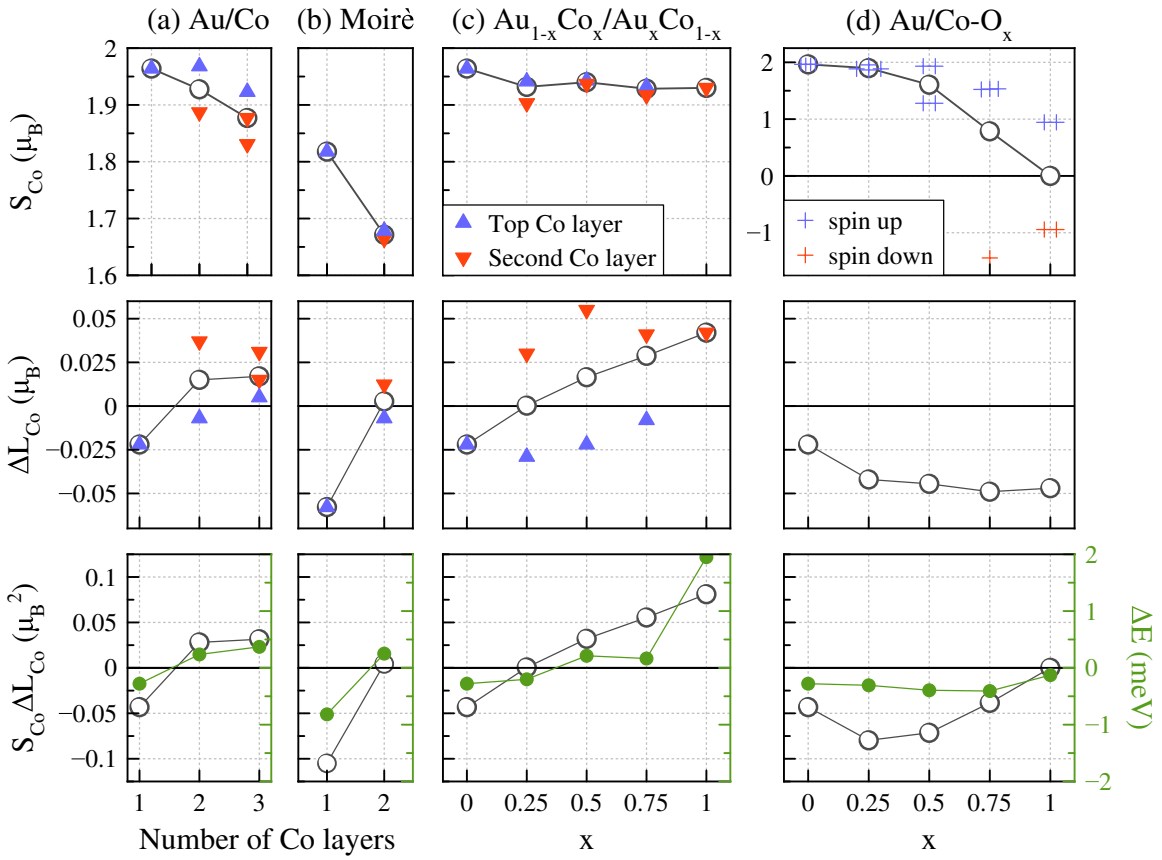

Figure 4.5: Co spin (top), Co orbital anisotropy (middle), and MAE (bottom) for Au/Co interfaces with different (a,b) numbers of Co layers (coherent/incoherent model), (c) amount of Au-Co intermixing, and (d) amount of surface oxidation. Black circles denote average values per atom. Positive (negative) values of ΔL_{Co} and ΔE represent out-of-plane (in-plane) magnetization.

4.4.3 Orbital anisotropy

A main contribution to the MAE is due to the SOC [110],

$$E^{\mathrm{SOC}} = -\xi \vec{S} \cdot \vec{L}, \tag{4.3}$$

where ξ is the SOC constant. Other contributions, such as dipole and anisotropic exchange interactions, usually play a negligible role in thin films [158]. From Eq. (2) we obtain

$$\Delta E^{\mathrm{SOC}} = E_z^{\mathrm{SOC}} - E_x^{\mathrm{SOC}} = \xi(S_z L_z - S_x L_x). \tag{4.4}$$

Since we have in good approximation $S_x = S_z = S$, using $\Delta L = L_z - L_x$, we arrive at the Bruno formula $\Delta E^{\mathrm{SOC}} = \xi S \Delta L$, which expresses the macroscopic MAE in terms of atomic parameters. Finally, since Au has a much smaller orbital anisotropy and spin than Co (for the coherent model with 1 Co layer we find $\Delta L_{\mathrm{Co}} \approx 11 \Delta L_{\mathrm{Au}} = -0.022$ μ_B and $S_{\mathrm{Co}} \approx 65 S_{\mathrm{Au}} = 1.97$ μ_B), the Au contribution to the MAE can be neglected and we obtain

$$\Delta E^{\mathrm{SOC}}_{\mathrm{Au/Co}} \approx \xi_{\mathrm{Co}} S_{\mathrm{Co}} \Delta L_{\mathrm{Co}}. \tag{4.5}$$

ΔL_{Co} and S_{Co} are shown in the top and middle rows of Fig. 4.5, respectively. The product $S_{\mathrm{Co}} \Delta L_{\mathrm{Co}}$ and its correlation with the MAE is addressed in the bottom row. We note that S_{Co} is hardly affected by Au-Co intermixing. It is smaller for the Moiré pattern (1.82 μ_B) than for the coherent model (1.96 μ_B). Yet, by the larger atomic density of the incoherent model, we obtain per Au unit cell a value of $36/25 \cdot 1.82$ $\mu_B = 2.62$ μ_B, which enhances the MAE. Surface oxidation facilitates superexchange between Co atoms through O atoms, which results in an antiferromagnetic spin alignment for some Co atoms starting at $x = 0.75$, see Fig. 4.5(d). For $x = 1$ the total spin becomes zero so that we expect zero MAE. The tiny value seen in Fig. 4.5(d) may originate from dipole-dipole interactions.

In contrast to S_{Co}, ΔL_{Co} changes dramatically when more Co layers are added or Co is intermixed with Au. Moreover, ΔL_{Co} and ΔE, see the bottom row of Fig. 4.5, are only qualitatively correlated, thus violating Eq. (5) to some extent [159]. We note that the formation of a Moiré pattern changes the absolute value but not the sign of the MAE, see Figs. 4.5(a) and (b). As compared to the coherent model, it is enhanced by a factor for 1 Co layer and reduced to half for 2 Co layers. Adding a second Co layer as well as Co-Au intermixing leads to in-plane magnetization for the top Co layer, while the second Co layer shows out-of-plane magnetization, see Figs. 4.5(a) to (c). This explains the discussed out-of-plane magnetization of the system, where the highest value (about eight times larger than without intermixing) is reached for

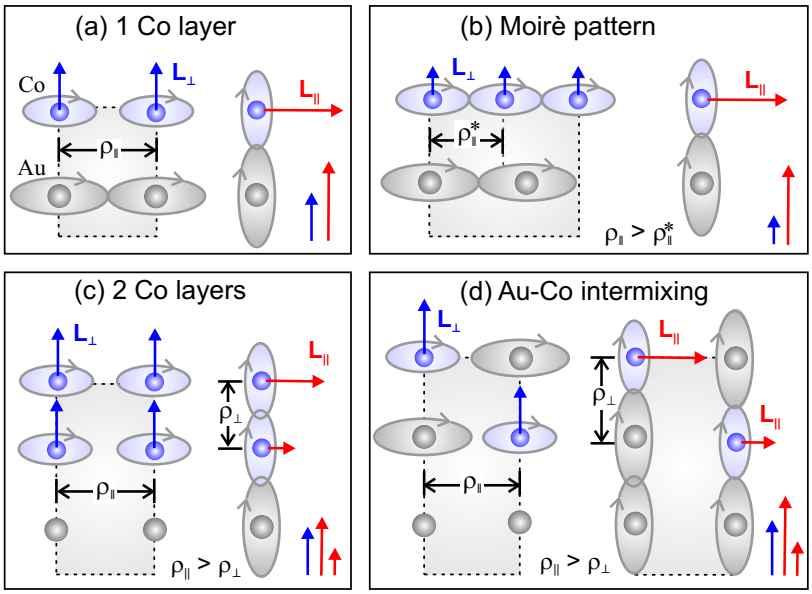

Figure 4.6: Orbital interactions of the atoms at the Au/Co interface in different cases.

$x = 1$. Under oxidation the Co orbital anisotropy changes only weakly, see Fig. 4.5(c), so that the MAE reflects essentially the changes of S_{Co}.

4.4.4 Bonding environment

The MAE is determined by the strength of the SOC and the anisotropy of the bonding environment, since the in-plane bonding environment determines the magnitude of the out-of-plane orbital moment and vice versa [160]. While ξ_{Co} is an atomic quantity and thus hardly depends on structural modifications, a change of ΔL_{Co} can be due to quenching of the anisotropy of the crystal field [161]. Thereby, it is assumed that the d orbitals at the interface can be grouped into in-plane (d_{xy} and $d_{x^2-y^2}$) and out-of-plane (d_{xz}, d_{yz} and d_{z^2}) orbitals, which host, respectively, out-of-plane and in-plane orbital moments.

In Fig. 4.6 we schematically demonstrate the bonding environment for the different models. The uppermost Co layer must have in-plane magnetization because it lacks neighboring atoms above, which explains the findings in Fig. 4.4(a). Because in the incoherent model the Co-Co in-plane distances are shorter than in the coherent model,

the out-of-plane orbital moment is smaller and, as a result, we observe a large in-plane magnetization, see Fig. 4.4(a). For 2 Co layers and Au-Co intermixing there are two types of Co atoms. The absolute value of the in-plane magnetization of the uppermost Co layer is a bit smaller than found for 1 Co layer, because Au-Co bonds are weaker than Co-Co bonds. The second Co layer misses no bonding partners and experiences strong surface tension that shortens the Co-Co and Au-Co bonds more in the out-of-plane than in the in-plane direction, resulting in out-of-plane magnetization that wins against the in-plane magnetization of the uppermost Co layer. It also wins for more than 25% Au-Co intermixing, see Fig. 4.4(b). For full intermixing ($x = 1$) there are no Co atoms left on top, see Fig. 4.6(d), so that we have a strong out-of-plane magnetisation. While adding a second Co layer and Co-Au intermixing supports out-of-plane magnetization, a Moiré pattern enhances the in-plane magnetization. If a second Co layer is added in the latter case then, due to the higher Co density, the overall out-of-plane character becomes less apparent.

4.5 Crystal field vs surface potential. Electronic structure.

It has been demonstrated in Refs. [56, 159–163] that the direction of the magnetization depends on the position of the d states with respect to the Fermi level. For example, the Fermi level of the Pd/Co interface is close to doubly degenerate states of mainly Co d_{xy} and $d_{x^2-y^2}$ character (in-plane orbitals) so that the out-of-plane magnetization dominates [160]. In Figs. 4.7(a) and (b) we plot densities of states without and with Au-Co intermixing assuming that the octahedral field is weak and the interface potential thus aligns the d orbitals as shown in Figs. 4.8(c) and (d). The fact that the $d_{3r^2-z^2}$ (out-of-plane) orbital appears at the Fermi level for the coherent models explains the in-plane magnetization. According to Stöhr [161], we should expect for

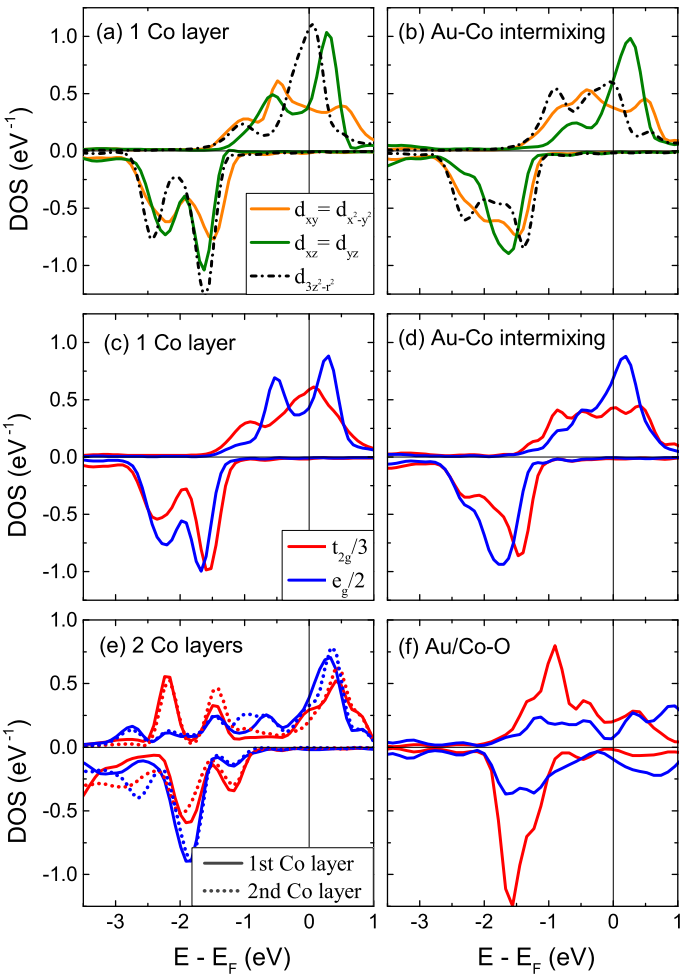

Figure 4.7: Projected Co densities of states: (a,c) 1 Co layer, (b,d) full Au-Co intermixing, (e) 2 Co layers, and (f) full surface oxidation. In (a,b) the surface potential is strong and in (c-f) the crystal field is strong ($t_{2g}/3 = d_{xy} = d_{yz} = d_{xz}$, $e_g/2 = d_{3z^2-r^2} = d_{x^2+y^2}$).

full Au-Co intermixing the $d_{x^2-y^2}$ and d_{xy} orbitals at the Fermi level, which is not the case. Indeed, the model of Stöhr ignores the fact that the out-of-plane orbitals also contribute to the out-of-plane magnetization, see Fig. 4.8(b). Similarly, the in-plane orbitals contribute to the in-plane magnetization. In addition, the bulk crystal field will not be completely suppressed by the surface and interface potentials.

If the crystal field is strong, which is the case in bulk fcc transition metals, the electronic structure can be understood in terms of t_{2g} and e_g orbitals, see Fig. 4.8(e). Projected densities of state for this case are shown in Figs. 4.7(c) to (f). We find for

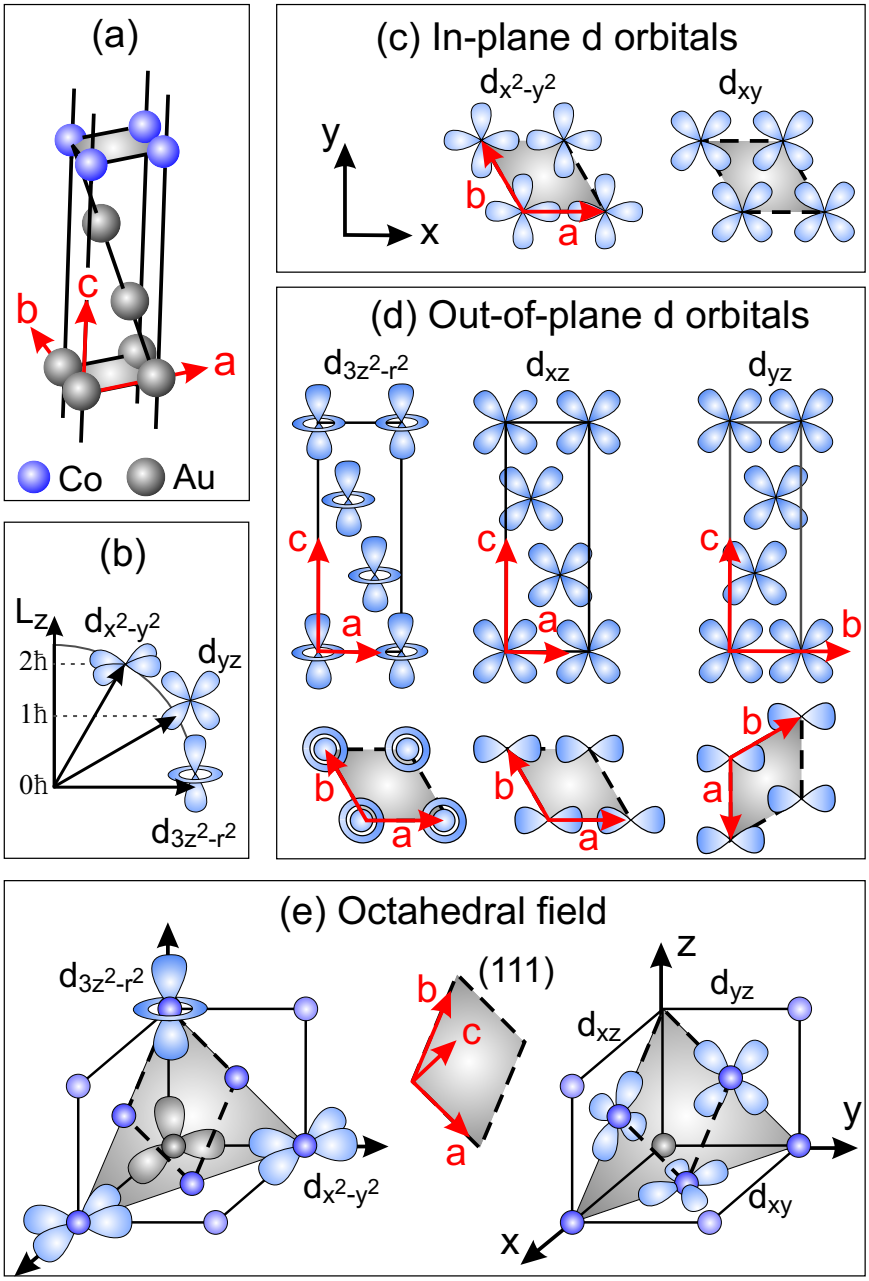

Figure 4.8: (a) Crystal axes and (b) L_z projection of the angular momentum. (c,d) If the surface potential dominates the crystal field, we have in-plane $d_{xy} = d_{x^2-y^2}$ and out-of-plane $d_{xz} = d_{yz}$, $d_{3z^2-r^2}$ orbitals. (e) If the crystal field dominates the surface potential, we have t_{2g} and e_g states.

the interfaces with in-plane magnetization more t_{2g} states and for those with out-of-plane magnetization more e_g states at the Fermi level. Indeed, the t_{2g} and e_g orbitals contribute more to the in-plane and out-of-plane magnetization, respectively, since the angle between the lobes of the d orbitals and the [111] direction, see Fig. 4.8(e), is larger for the former (54.7°) than for the latter (35.3°) case. For full surface oxidation ($x = 1$), see Fig. 4.7(f), the spin polarization at the Fermi level is strongly reduced, which agrees with the top panel of Fig. 4.5(c). Due to the antiferromagnetic coupling the magnetization vanishes. On the other hand, see the middle panel of Fig. 4.5(c), the in-plane orbital moment is reflected by the t_{2g} character at the Fermi level.

4.6 Summary

In conclusion, we have used first principles calculations to study that factors that determine the magnetization direction and absolute value at Au/Co interfaces. Coherent models ignoring the lattice mismatch between Au and Co are found to result in a too small MAE due to the reduced Co density, in contrast to a more realistic structure with Moiré pattern. Increasing the Co thickness from 1 to 2 layers switches the magnetization from in-plane to out-of-plane for both the coherent and incoherent models. Au-Co intermixing leads to out-of-plane orbital moments of the Co atoms in the mixed atomic layers, which start to dominate over the in-plane orbital moments at about 50% intermixing. When 75% of the Co hollow sites at the surface are occupied by O atoms, the magnetic anisotropy is maximal with in-plane easy axis. For further oxidation superexchange results in antiferromagnetic coupling that reduces the total spin, so that the MAE finally vanishes. In general, the magnetic anisotropy and even the magnetization direction depend strongly on structural details. For instance, if a second Co layer occupies fcc instead of hcp hollow sites (which is energetically only slightly less favorable) we obtain in-plane instead of out-of-plane magnetization.

Chapter 5

k-Asymmetric Spin-Splitting at the Interface between Transition Metal Ferromagnets and Heavy Metals

We systematically investigate the spin-orbit coupling-induced band splitting originating from inversion symmetry breaking at the interface between a Co monolayer and $4d$ (Tc, Ru, Rh, Pd, and Ag) or $5d$ (Re, Os, Ir, Pt, and Au) transition metals. In spite of the complex band structure of these systems, the odd-in-k spin splitting of the bands displays striking similarities with the much simpler Rashba spin-orbit coupling picture. We establish a clear connection between the overall strength of the odd-in-k spin-splitting of the bands and the charge transfer between the d-orbitals at the interface. Furthermore, we show that the spin splitting of the Fermi surface scales with the induced orbital moment, weighted by the spin-orbit coupling.

5.1 Introduction

The development of modern spintronic devices, such as magnetic random access memories and current-driven nano-oscillators, is currently relying on the exploitation of the mechanism of spin transfer torque [10, 11] in magnetic systems displaying per-

pendicular magnetic anisotropy [5]. Besides materials displaying bulk perpendicular magnetic anisotropy (such as ordered alloys [164]), the most promising devices involve multilayers accommodating large interfacial-induced perpendicular magnetic anisotropy, such as interfaces between transition metal ferromagnets and noble metals [6] or metal oxides [7, 9, 165] (see also Ref. [166]). This combination has proven successful in reducing the critical current density needed to achieve current-driven magnetic excitations and switching within a reasonable range (i.e. below 10^6 A/cm^2). However, the difficulty in reducing this critical current density further constitutes a major hurdle towards applications, calling for innovative mechanisms beyond spin transfer torque. As discussed below, the physics of spin-orbit coupling at the origin of the perpendicular magnetic anisotropy might hold the key to the next technological breakthrough [167].

Interfacial perpendicular magnetic anisotropy at X/F interfaces (X being a noble metal, F a transition metal ferromagnet) is a subtle phenomenon that arises from spin-orbit coupled orbital overlaps. Spin-orbit coupling, given by $H_{\rm so} = (\xi/\hbar)\boldsymbol{\sigma}\cdot(\boldsymbol{\nabla}V\times\mathbf{p})$ (ξ is the spin-orbit coupling strength in eV/m^2), couples the spin degree of freedom $\boldsymbol{\sigma}$ to the gradient of the crystal field $\boldsymbol{\nabla}V$. In the spherical atomic potential approximation, $\boldsymbol{\nabla}V = (\partial_r V/r)\mathbf{r}$ and the interfacial perpendicular magnetic anisotropy is conventionally associated with the orbital overlap leading to an enhanced interfacial orbital angular momentum $\mathbf{L} = \mathbf{r}\times\mathbf{p}$ [6, 160, 168]. In the independent ligand theory, its magnitude can be related to the anisotropy of the orbital angular momentum $\Delta E_{\rm so} = \xi/(4\mu_{\rm B})(m^{\parallel}_{\rm orb} - m^{\perp}_{\rm orb})$ [6, 59, 161], where $m^{\parallel(\perp)}_{\rm orb}$ is the orbital moment when the magnetization lies in (perpendicular to) the plane and $\mu_{\rm B}$ is the Bohr magnetron. In this simple scenario (which disregards the complexity of interfacial orbital overlaps), interfacial perpendicular magnetic anisotropy survives in symmetrically grown systems such as Pt/Co/Pt, for instance. However, when the two interfaces embedding the transition metal ferromagnet are not equivalent, such as in Pt/Co/AlOx or

Ta/CoFeB/MgO, the symmetry is broken and additional effects emerge.

In such systems, the sharp interface between the ferromagnet and the noble metal breaks the inversion symmetry along the normal to the interface, $\mathbf{z}$. In a simplistic picture, the gradient of potential becomes $\langle \xi \boldsymbol{\nabla} V \rangle \approx -\alpha \mathbf{z}$ and the spin-orbit coupling Hamiltonian reduces to $H_{\mathrm{R}} \approx -\alpha \boldsymbol{\sigma} \cdot (\mathbf{z} \times \mathbf{k})$, where α is the so-called Rashba parameter [15, 63]. Such $\mathbf{k}$-linear spin-orbit coupling has been observed at the surface of various metals such as Au [64, 65], Gd [66], or Bi compounds [67–69] and more recently at the surface of three dimensional topological insulators [70, 71]. Notice that in general, spatial inversion symmetry breaking imposes the spin-orbit coupling term to be *odd* in momentum $\mathbf{k}$, but not necessarily linear. Indeed, such odd-in-k spin-orbit coupling is well known in bulk non-centrosymmetric semiconductors [72] and has been detected recently at oxide heterointerfaces [73].

A direct consequence of this odd-in-k spin-orbit coupling on the local spin configuration is the emergence of an antisymmetric exchange interaction, the so-called Dzyaloshinskii-Moriya interaction [169, 170], on the form $\sum_{ij} \mathcal{D}_{ij} \mathbf{S}_i \times \mathbf{S}_j$ where $\mathbf{S}_{i(j)}$ is the direction of the spin angular momentum of the ion at position $\mathbf{r}_{i(j)}$. Under certain conditions (exchange, anisotropy, temperature etc.), this interaction produces chiral spin textures such as spin spirals, as observed at W/Mn and Ir/Fe interfaces [171–175], and skyrmions [20, 21, 176]. Very recently, it has also been shown that this interaction favors Néel over Bloch configuration of magnetic domain walls in Ni/Fe multilayers [177, 178]. Such a distortion is a key element to understand the observed anomalous domain wall motion in ultrathin perpendicularly magnetized multilayers [28, 179, 180].

Another important phenomenon that may play a role in materials lacking inversion symmetry is the current-driven spin-orbit torque [181, 182]. In non-centrosymmetric multilayers, the interfacial odd-in-k spin-orbit coupling enables the so-called inverse spin galvanic effect, i.e. the electrical generation of a non-equilibrium spin density

[14]. This spin density can be used to manipulate the magnetization of the adjacent ferromagnet. Spin-orbit torque has been theoretically predicted using model Hamiltonians with Rashba or Dresselhaus spin-orbit coupling [183–194] and first principle calculations on realistic interfaces have been achieved recently [88, 195, 196], confirming qualitatively the theoretical results. Its experimental identification in Pt/-Co/AlOx [16, 18, 19, 197–199] and other similar structures [76, 200–206] is currently a growing field in spin electronics and regarded as a possible way to complement or even replace spin transfer torque in devices possessing perpendicular magnetic anisotropy.

While these phenomena all arise from interfacial symmetry breaking in the presence of spin-orbit coupling, the details of these mechanisms remain quite complex and explicit connections have only been established within the framework of Rashba spin-orbit coupling [201]. Indeed, first principle calculations clearly revealed that this latter approximation is far from realistic [86, 88, 195, 196, 207, 208]: Breaking spatial inversion symmetry hardly affects the strength of the atomic spin-orbit coupling itself (in sharp contrast with the phenomenological picture developed by Bychkov and Rashba [15]), but it distorts the wave function close to the nuclei, where the spin-orbit coupling is stronger [86, 207, 208]. The interaction between atomic spin-orbit coupling and these distorted wave functions results in an effective odd-in-k spin-orbit coupling. In addition, in metallic systems the detail of the orbital hybridization at the interface between, say, a ferromagnet and a heavy metal is quite complex, resulting in an induced magnetic moment in the heavy metal and an enhancement of the orbital momentum in the ferromagnet. Providing a clear description of the interfacial spin-orbit coupling-induced band splitting and associated phenomena for a wide variety of materials could help designing interfaces with tunable properties.

In this article, in order to uncover the physics governing the interfacial spin-orbit coupling in such bilayers, we present a systematic investigation of the (spin-orbit coupling-induced) band splitting at X/Co interfaces, where X represents a $4d$ or $5d$

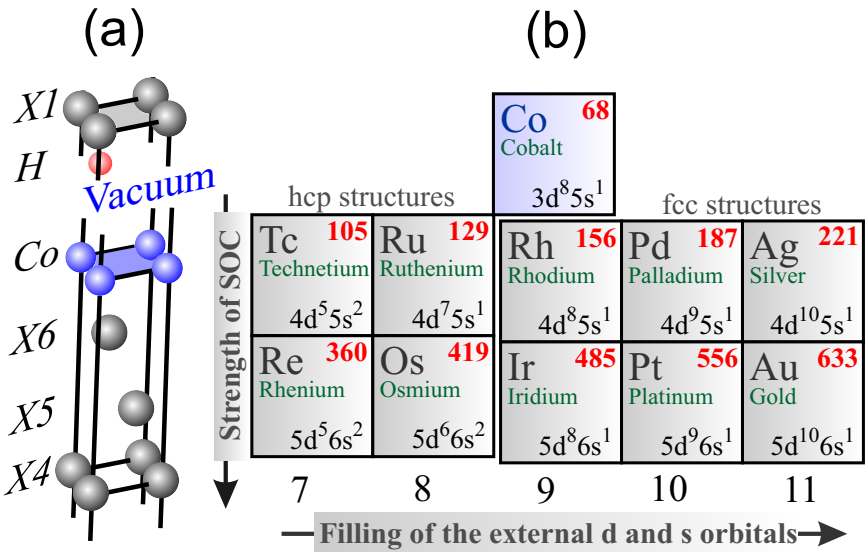

Figure 5.1: (a) Unit cell of the X/Co interfaces (X= 4*d*-metals = Tc, Ru, Rh, Pd, Ag and X = 5d-metals = Re, Os, Ir, Pt, Au) and (b) their electronic configurations used in this work[209]. Numbers in red stand for the strength of spin-orbit coupling in meV.

metal as depicted in Fig. 5.1. Using first principle methods, we establish clear connections between the odd-in-k spin splitting and the interfacial orbital angular momentum and related charge transfer. This article is organized as follows. Computational details are summarized in Section 5.2 and the results are reported in Section 5.3. Section 5.3.1 presents the electronic structure of these interfaces together with their magnetization profile, while Section 5.3.2 describes the spin-orbit coupling-induced band splitting properties. A summary is given in Section 5.4.

5.2 Computational details

In principle, the accurate description of the magnetic and electronic properties of X/Co interfaces (X = 4*d*- and X= 5*d*-metals) using first principles calculations necessitates the definition of a huge supercell in $\widehat{xy}$ plane with Moiré pattern [155] due to the large lattice mismatch between the two materials. However, the large size of the cell combined with the presence of spin-orbit coupling makes such calculations

computationally expensive. To avoid this hurdle, we imposed the lattice parameter of the free standing Co layer to match the lattice parameter of the substrate X. Due to the artificial strain, the computed electronic and magnetic properties of the X/Co system may be different from the ones of a realistic interface. Indeed, in Ref. [155] it was demonstrated that for a Co monolayer deposited on top of Pt (Au), the tensile stress results in an enhancement of the magnetic moments of Pt (Au) and Co layers by 22 % (10 %) and 10 % (15 %), respectively. The objective of the present work is not to match the experimental observations by modeling a realistically disordered interface but rather to describe the systematic modification of the band splitting and magnetic properties of such bilayers when changing the heavy metal substrate.

In this work, a monolayer of Co was placed on top of a 6-layer slab of a X(111) substrate that is either a $4d$ (Tc, Ru, Rh, Pd, and Ag) or a $5d$ metal (Re, Os, Ir, Pt, and Au), see Fig. 5.1(a). This allows us to study the dependence of the band splitting and its related properties as a function of the spin-orbit coupling strength and electronic configurations of the external ds-orbitals, as illustrated in Fig. 5.1(b). Moving from the left to the right side of the table, the number of electrons on the external ds-orbitals grows from 7 to 11. Structures with $[ds]^7$ and $[ds]^8$ electronic configurations have hcp packing while with $[ds]^9$, $[ds]^{10}$ and $[ds]^{11}$ electronic configurations adopt fcc packing. Our test calculations reveal that Co prefers hcp and fcc hollow sites on top of X in the first and second cases, respectively. In addition, a vacuum of 10 Å and one H atom on the bottom of the substrate were found as sufficient conditions to avoid charge accumulation. First principle calculations were performed in the generalized gradient approximation [103]. For the structure optimization we used the pseudopotential method that is implemented in VASP [132, 142] [1] while the magnetic properties were investigated within the full-potential code FLEUR. The

[1] Certain commercial products are identified in this paper in order to specify the computational procedures adequately. Such identification is not intended to imply recommendation or endorsement by the National Institute of Standards and Technology, nor is it intended to imply that the materials or equipment identified are necessarily the best available for the purpose.

magnetic properties were calculated using an increased number of k-points in the Brillouin zone until convergence which is achieved for 2304 k-points. To study the band splitting below and at the Fermi level we used 256 k-points for each radial direction and 4096 equally-distributed k-points in the irreducible Brillouin zone, respectively.

5.3 Results and discussion

5.3.1 Electronic structures

The magnetic properties of X/Co interfaces are direct outcomes of interfacial orbital overlap. Therefore, before entering in the detailed analysis of these properties, we turn our attention towards the nature of these hybridizations. The density of states and magnetic properties of the d-orbitals of X/Co bilayers are displayed in Figs. 5.2 and 5.3, respectively. The first remarkable feature is the distinct behavior between metals with partially filled d-shells (Tc, Ru, Re, Os, Ir, Pt, Rh and Pd) and metals with filled d-shells (Au and Ag). While the formers present a sizable density of states at the Fermi energy, this density of states is vanishingly small in the latter cases leading to a reduced d-orbital hybridization between Co and X. As a general rule, upon increasing the d-orbital filling the binding energy decreases due to (i) the enhancement of the "artificial" lattice distortion imposed by the lattice mismatch between Co and X and (ii) the reduction of the orbital hybridization. The latter results in a strong reduction of the Co-X binding in the case of Au and Ag.

The nature of the orbital hybridization between Co and X has important consequences on the magnetic properties at the interface. First, metals with partially filled d-shells acquire a large magnetic moment through proximity effect [46, 168, 210, 211], which vanishes in the case of metals with filled d-shells (Au and Ag), see Fig. 5.3(a). Notice that the magnetic proximity effect is very small in the case of Tc, Ru, Os and Re but does not vanish. Most importantly for the present study, the magnetic

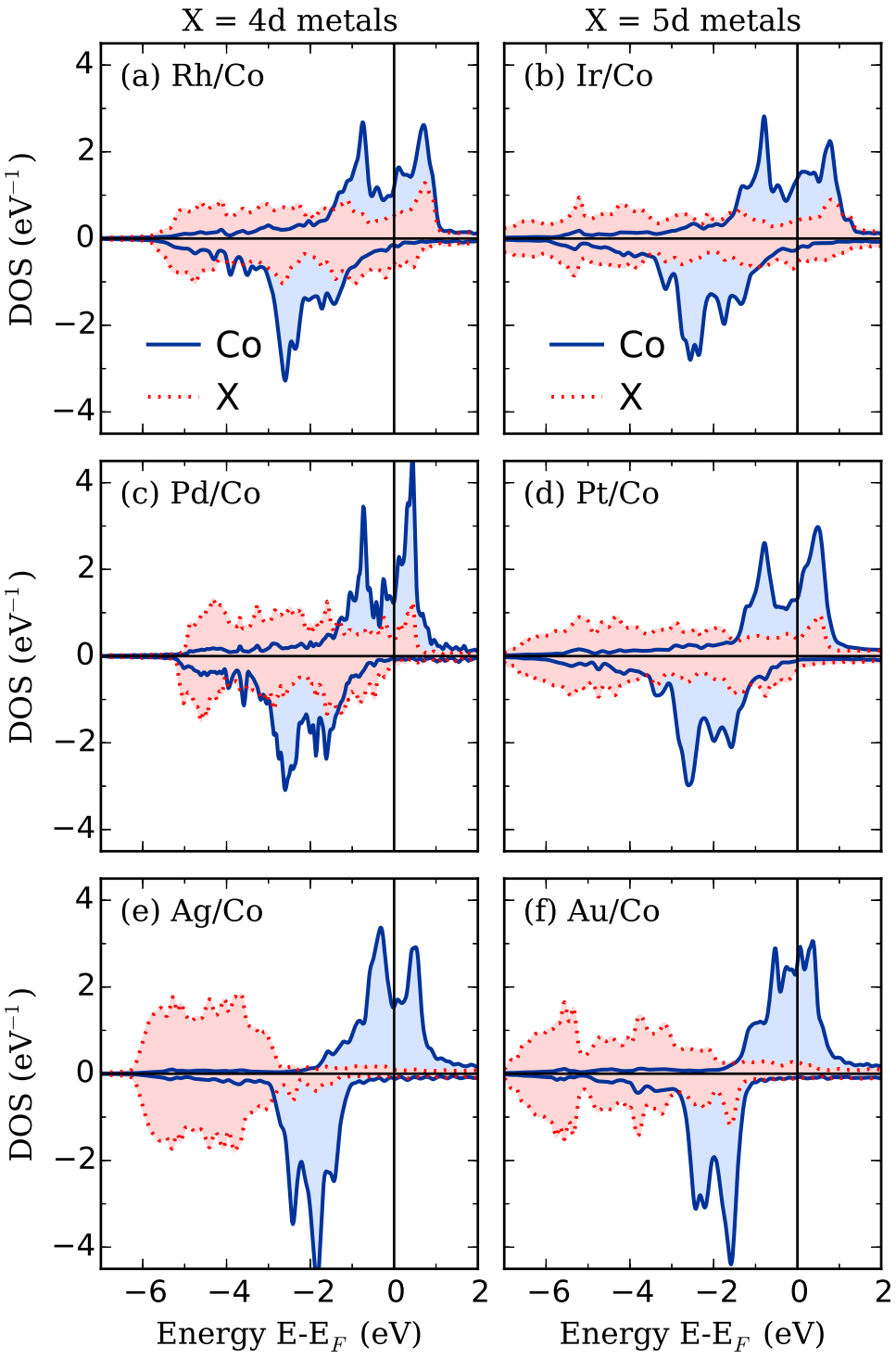

Figure 5.2: Projected density of states (DOS) for the X/Co interfaces, where X is a heavy metal as indicated on the figure. The amount of hybridization between the $3d$ orbitals of Co and $4(5)d$ orbitals of the heavy metal decreases when increasing the d-orbital filling of the heavy metal. The densities of states for X=Tc, Ru, Re and Os are not represented as they show a qualitatively similar behavior as heavy metals with partially filled d-shells.

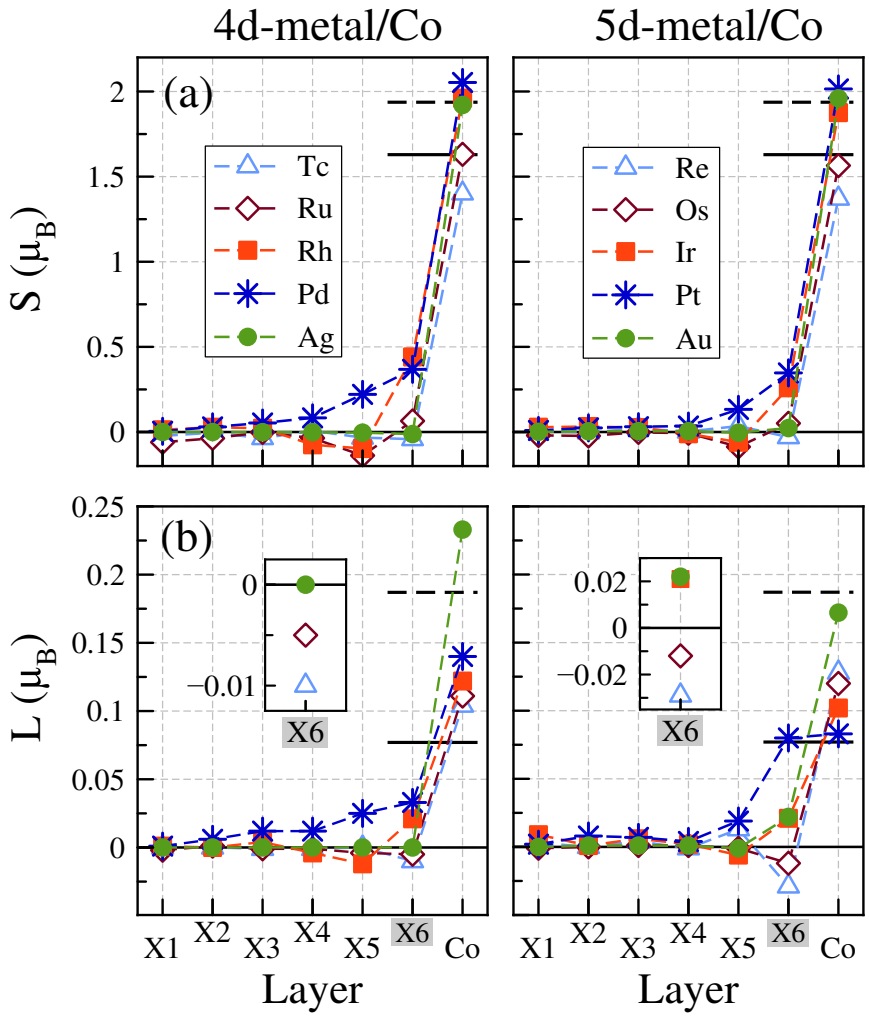

Figure 5.3: Layer resolved magnetic properties of the X/Co interfaces, where X is a heavy metal. (a) spin and (b) orbital contributions to the magnetic moment for a magnetization pointing along **x**. The left (right) panels represent the $4d$ ($5d$) metals, as indicated on the figure. Solid (dashed) line indicates the value for the bulk (free standing layer of) Co.

proximity effect is accompanied by an induced orbital moment that is negative for Tc, Ru, Re, and Os and positive at the interface with Rh, Pd, Ag, Ir, Pt, and Au, see Fig. 5.3(b). As discussed below, the sign and magnitude of the induced orbital moment has a dramatic impact on the spin-orbit-induced splitting of the band structure.

It is worth mentioning that all the structures discussed in this work and involving heavy metals with partially-filled d-shells present interfacial perpendicular magnetic

anisotropy, while the weak hybridization between Co and metal with filled d-orbitals (Ag and Au) results in large in-plane magnetic anisotropy (the latter being in contradiction with experimental observations but in agreement with other theoretical results due to artificial strain in our calculations [56, 210, 212]). However, since we could not find any robust correlation between the magnetic anisotropy and the strength of the band splitting, we choose not to further discuss magnetic anisotropy here.

5.3.2 k-asymmetric spin splitting

In the previous section, we have illustrated the complex hybridization scheme of heavy metal/ferromagnet interfaces through the onset of magnetic proximity effect as well as induced orbital moment. We now turn our attention towards the main topic of the present work, i.e. the nature of spin-orbit coupling-induced spin-splitting in asymmetric magnetic bilayers.

Spin-orbit induced band splitting

In inversion asymmetric systems, spin-orbit coupling induces a spin-splitting of the band structure on the form $H_{\text{so}} = \mathbf{w}(\mathbf{k})\cdot\boldsymbol{\sigma}$, where $\mathbf{w}(\mathbf{k}) = -\mathbf{w}(-\mathbf{k})$ is an odd function of $\mathbf{k}$. In order to visualize and analyze such a band splitting, we adopt the approach developed in Ref. [87]: The band structure is calculated for two opposite directions of the magnetization, say $\pm\mathbf{u}$, hence revealing the spin-orbit coupling-induced asymmetric spin-splitting. For instance, the Fermi surface and band structures of the Ir/Co interface along the x- and y-directions in Brillouin zone is reported on Fig. 5.4, central, top, and right panels, respectively, when imposing the magnetization to lie along $+\mathbf{x}$ (red lines) and -$\mathbf{x}$ (blue lines). Similar electronic structures for another X/Co interface are are shown on Fig. 5.5. The band structures obtained for opposite magnetization directions are mirror symmetric with respect to $k_y = 0$, as expected, ensuring that the band structure remains time-reversal symmetric, i.e. $\delta E(m_x, k_y) = \delta E(-m_x, -k_y)$.

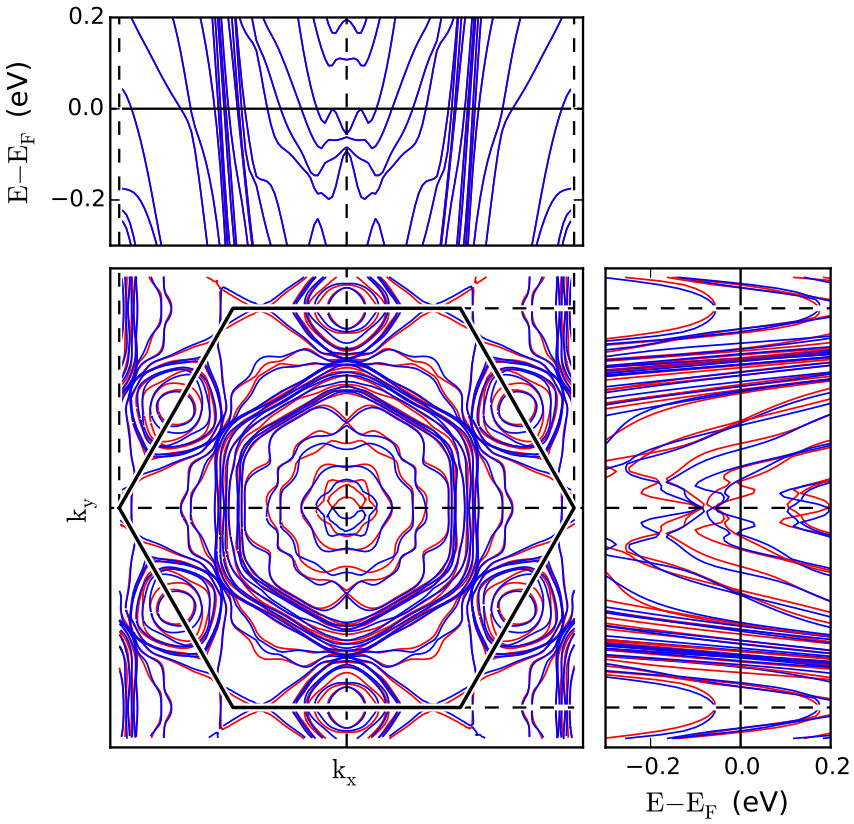

Figure 5.4: (Color online) Central panel: two-dimensional Fermi surface of Ir/Co interface in (k_x, k_y) plane, when the magnetization direction is along $+\mathbf{x}$ (red lines) or $-\mathbf{x}$ (blue lines). Right panel: Band structure of Ir/Co interfaces calculated along the y-direction in Brillouin zone; Top panel: Band structure of Ir/Co interfaces calculated along the x-direction in Brillouin zone. A clear splitting of the band structure is observed when the band structure is projected perpendicular to the magnetization direction (Right panel), while no splitting appears when the band structure is projected along the magnetization direction (Top panel).

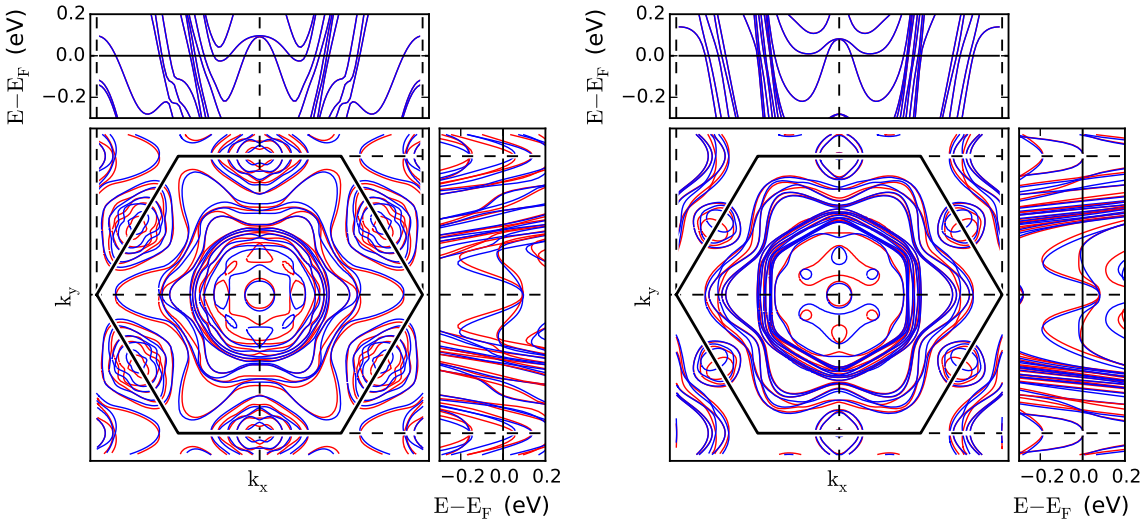

(a) Re/Co

(b) Os/Co

(c) Pt/Co

(d) Au/Co

Figure 5.5: Electronic structures of some X/Co interfaces. For more details see Fig 5.4.

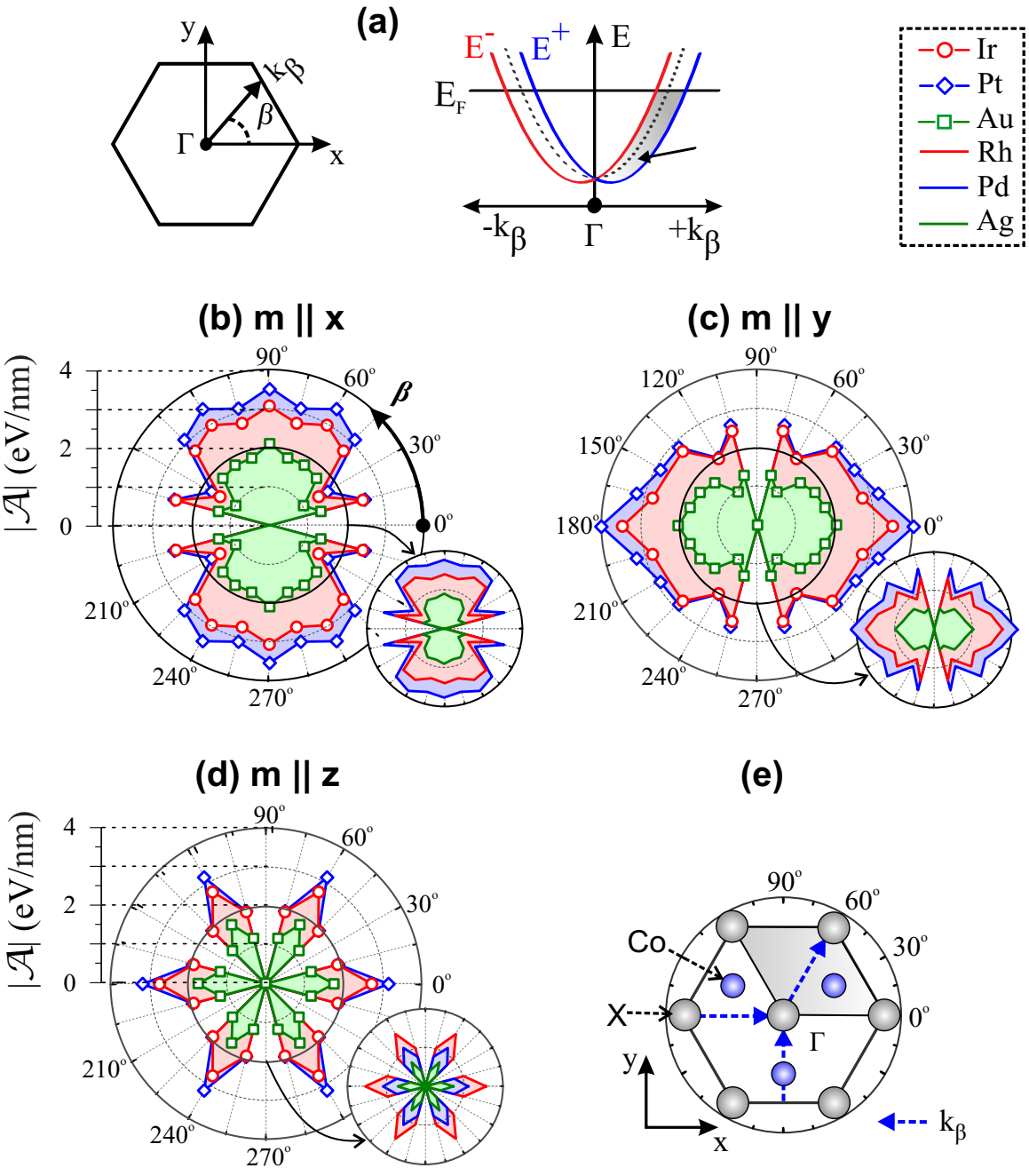

Figure 5.6: (a) Brillouin zone and schematic representation of the odd-in-k splitting along β direction. $\mathcal{A}_n$ is the spanned area; k_β are examples of the electron propagation directions with respect to the crystal structure; (c), (d), and (e) $|\mathcal{A}| = |\mathcal{A}(\beta)|$, for the magnetization along $+\mathbf{x}$, $+\mathbf{y}$, and $+\mathbf{z}$ directions, respectively. Small and large polar coordinates have the same scale and refer to the 4d-metal/Co and 5d-metal/Co interfaces, respectively. (e) (x,y)-projection of the X/Co interface. For the sake of readability, the value of $|\mathcal{A}|$ for Tc, Ru, Os and Re are omitted in this figure.

When the magnetization is applied along $\pm\mathbf{x}$, the band structure calculated along the x-direction in Brillouin zone does not display any spin-splitting, see Fig. 5.4 top panel. Similar results have been obtained for all the substrates considered. When removing the interface, using either an isolated Co or X layer, this asymmetric splitting disappears (not shown).

Evaluating the strength of the odd-in-k spin-splitting has been achieved using various approaches. For instance, Bihlmayer *et al.* [86] directly calculated the potential gradient $\langle \partial_r V/r \rangle$ close to the atom nucleus, Park *et al.* [87] evaluated the linear slope of the band structure close to $k = 0$ (which probably corresponds to the closest definition of the Rashba spin-splitting), while Haney *et al.* [88, 195, 196] calculated the inverse spin galvanic effect arising from odd-in-k spin splitting (which is a more experimentally-relevant quantity). The variety of methods illustrates the difficulty to give a proper account of the strength of spin-orbit coupling-induced spin-splitting in asymmetric systems. In the present work, we adopt an intuitive approach to evaluate the magnitude of the spin-splitting at and below the Fermi level.

Spin-splitting below Fermi level

The area spanned by the band n upon magnetization reversal from $+\mathbf{u}$ to $-\mathbf{u}$ is $\mathcal{A}_n = \int |E_n^+ - E_n^-| dk$ [shaded area in Fig. 5.6(a)], where $E_n^\pm$ is the energy dispersion when the magnetization lies along $\pm\mathbf{u}$. To evaluate the global strength of the spin splitting below the Fermi level, we calculate the total area $\mathcal{A}$ as

$$|\mathcal{A}| = \sum_n^N \sum_i^{N_k} |\Delta E_{ni}| \Delta k_i, \tag{5.1}$$

where the first summation $\sum_n^N$ runs over the band index n, the second summation $\sum_i^{N_k}$ stems from the discretization of the integral in k-space and $\Delta E_{ni} = E_{ni}^+ - E_{ni}^-$. Notice that in Eq. (5.1) only absolute values of the energy shifts enter the calculation.

Indeed, since the sign of the spin-splitting depends on the band index[87] accounting for the relative magnitudes of the shifts rather than for their absolute values would result in cancellations between different bands and might not give a full account of the global spin splitting strength. By calculating the absolute value of $|\mathcal{A}|$, we ensure that we evaluate only the absolute strength of the asymmetric spin-splitting. Therefore $|\mathcal{A}|$ provides an estimation of the spin-splitting asymmetry for all bands below the Fermi energy.

In contrast to systems that have a well-isolated surface state (such as Au (111) surface [64, 65] or Bi/Ag (111) surface alloy [67, 69]), in case of X/Co bilayers the strong interfacial spin-orbit splitting is spread over the continuum of bulk bands. However, since $|\mathcal{A}|$ is determined by the states close to the interface, its magnitude converges quickly as the thickness of the substrate increases, as shown on Figs. 5.7 (a) and (b). To numerically compute $|\mathcal{A}|$, the band structure calculations were repeated for different directions β in the Brillouin zone [see Fig. 5.6(a)], as well as for three different magnetization directions (along $\mathbf{x}$, $\mathbf{y}$ and $\mathbf{z}$ axes). The spanned absolute areas $|\mathcal{A}|$ calculated for various β directions in the Brillouin zone and when the magnetization lies along $\mathbf{x}$, $\mathbf{y}$ and $\mathbf{z}$ axes are shown on Fig. 5.6 (c), (d) and (e), respectively. Several features are worth noticing.

First, while the global angular dependence of $|\mathcal{A}|$ depends on the magnetization direction and displays different symmetries in the different cases, their shapes do not depend on the substrate. Second, when the magnetization lies in the interface plane ($\mathbf{x}$, $\mathbf{y}$), $|\mathcal{A}|$ reaches its maximum when the $\mathbf{m}\perp\mathbf{k}$ ($\beta = \pm 90^\circ$ when $\mathbf{m}||\mathbf{x}$ and $\beta = 0^\circ$ when $\mathbf{m}||\mathbf{y}$) and vanishes when $\mathbf{m}\|\mathbf{k}$ ($\beta = 0^\circ$ when $\mathbf{m}||\mathbf{x}$ and $\beta = \pm 90^\circ$ when $\mathbf{m}||\mathbf{y}$). These two features partially validate a standard Rashba model described by the Hamiltonian $H_{\mathrm{R}} = \alpha(\boldsymbol{\sigma} \times \mathbf{k}) \cdot \mathbf{z} \propto \sin\beta$. Fig. 5.7(a) compares the angular dependence of the magnitude of $|\mathcal{A}|$ extracted from the first principle calculations (from both VASP and FLEUR codes) reported on Fig. 5.6(c) and the $\sin\beta$

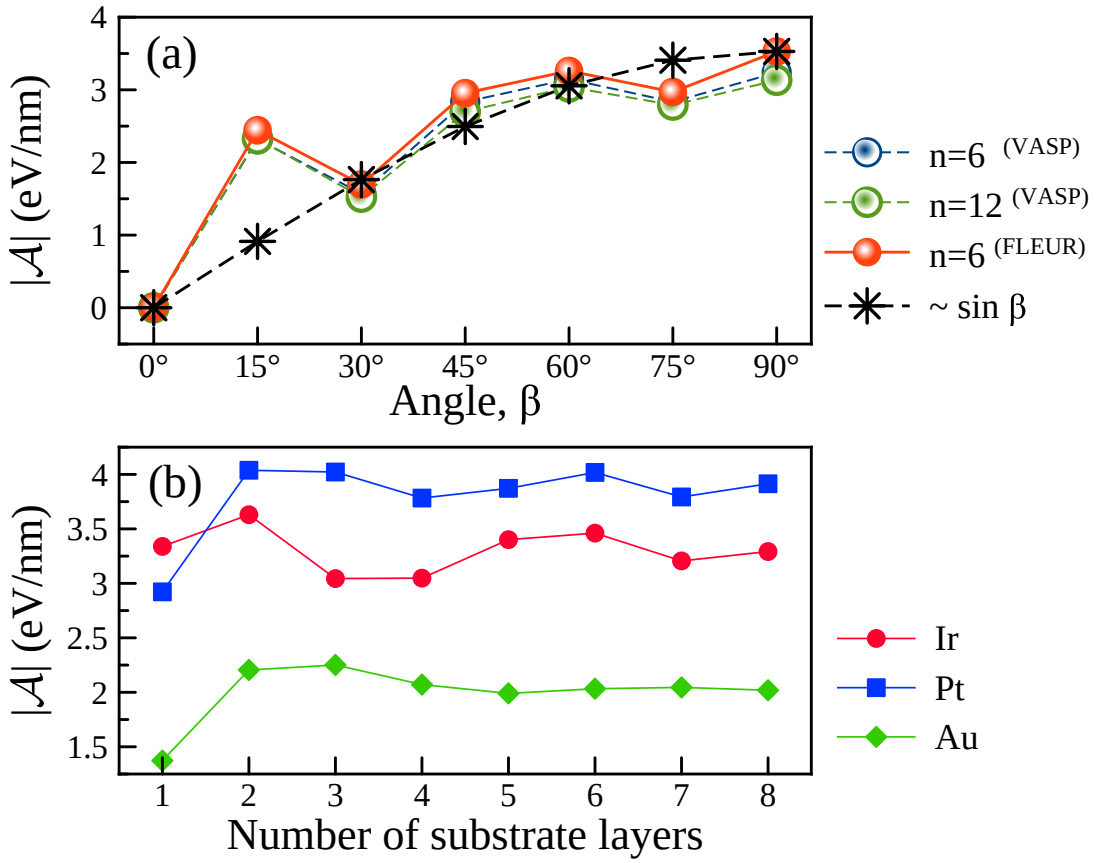

Figure 5.7: (a) Angular dependence of the total band splitting $|\mathcal{A}(\beta)|$ calculated by first principles (VASP and FLEUR) and by the standard Rashba model ($H_{\mathrm{R}} \propto \sin\beta$ - see main text) for the Pt_n/Co interfaces (n is a number of Pt layers). Magnetization is along $\mathbf{x}$. (b) Dependence of $|\mathcal{A}(\beta = 0°)|$ on the number of substrate layers for Ir, Pt, and Au. Magnetization is along $\mathbf{y}$.

dependence expected from the Rashba model. Deviations from the sine shape are clearly visible in Fig. 5.7(a) at β=15°, 45°, and 75°. These angles correspond to points where the in-plane crystalline symmetry is broken, see Fig. 5.6(b). Notice that these calculations have been reproduced for a thicker substrate thickness [n=12 layers, green symbols in Fig. 5.7(a)] with only minor variations, showing that $|\mathcal{A}|$ is a robust quantity to characterize the total band splitting below the Fermi level. Third, a spin-splitting is observed when the magnetization lies out of the plane of the interface [see Fig. 5.6(e)]. In fact, the spin-splitting in this case displays a 6-fold symmetry which is a reminiscence of the crystal structure [see Fig. 5.6(c)]. The van-

ishing splitting at $\beta = 30° + m \times 60°$, $m \in \mathbb{Z}$, corresponds to high symmetry points in Brillouin zone while the maxima at $\beta = m \times 60°$ corresponds to low symmetry points [see Fig. 5.6(b)]. Of course, in a system with cylindrical symmetry around **z** like in a two-dimensional free electron gas with Rashba spin-orbit coupling, no splitting is observed when the magnetization lies along **z**.

Finally, one can notice that the magnitude of $|\mathcal{A}|$ also depends strongly on the substrate as reported on Fig. 5.8(a). Generally, $4d$ substrates display weaker spin splitting than $5d$ substrates, which is a direct consequence of their weaker spin-orbit coupling strength. However, the spin splitting magnitude also depends on the band filling and within a same class of materials (either $4d$ or $5d$) shows a maximum for n$[ds]^{10}$ materials (i.e. Pd and Pt), see Fig. 5.1. As mentioned in the introduction, Bihlmayer *et al.* [86] and more recently Krasovskii [213] have noticed that, in contrast with the conventional phenomenology of Rashba spin-orbit coupling, the interfacial symmetry breaking leaves the atomic spin-orbit coupling unaffected while it strongly distorts the wave function itself. The interplay between this distorted wave function and the spherically symmetric spin-orbit coupling produces the asymmetric spin splitting of the band structure. The distortion of the wave function at the interface between the substrate and the Co monolayer is associated with a charge transfer from the substrate to the Co layer, which is reported on Fig. 5.8(a) for d-orbitals. A qualitative correlation is obtained between the spin splitting parameter $|\mathcal{A}|$ and the charge transfer, both displaying a maximum for Pd and Pt.

Spin splitting at the Fermi level

Let us now turn our attention towards the properties of the Fermi surface, displayed in Fig. 5.4, central panel, for Ir/Co. While the Fermi surface is very far from circular, it displays a shift along the y-direction when changing the magnetization direction from +**x** (red) to -**x** (blue), confirming the intuition given by the Rashba model.

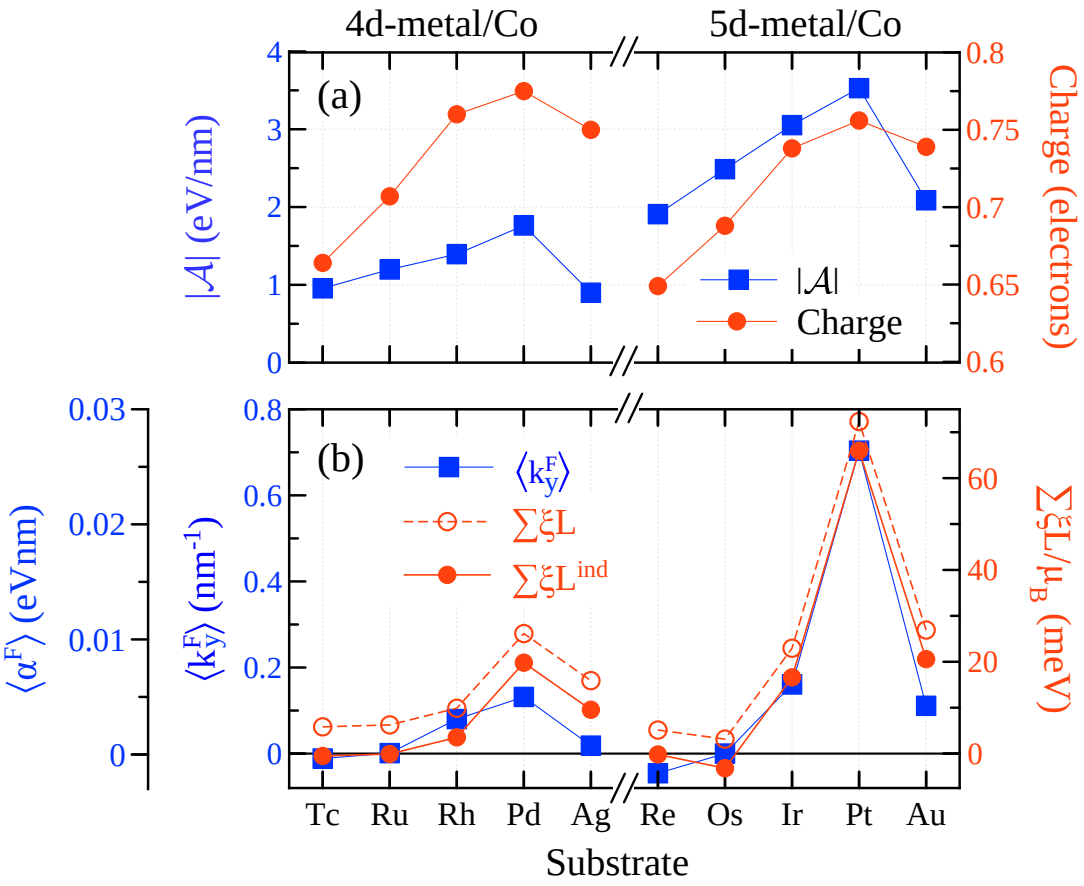

Figure 5.8: Correlation between odd-in-k spin splitting and interfacial electronics properties as a function of substrate: (a) spanned area $|\mathcal{A}|$ (blue symbols) and charge transfer from the d-orbitals of substrate to the d-orbitals of Co (red symbols); (b) effective momentum shift $\langle k_y^{\mathrm{F}} \rangle$ (blue symbols) and summation of the induced orbital moments of each atom weighted by their spin-orbit coupling constant, $\sum_i \xi_i L_i^{ind}$ (red symbols).

To evaluate the strength of the spin splitting at the Fermi level, we compute the k-averaged Fermi wave vector $\langle \mathbf{k}^F \rangle$ defined

$$\langle \mathbf{k}^F \rangle = \sum_n^{N_b} \mathbf{k}_n^F = \sum_n^{N_b} \frac{1}{N_k} \sum_i^{N_k} \mathbf{k}_{in}^F, \tag{5.2}$$

where the first summation $\sum_n^{N_b}$ runs over the band index n and second one $\sum_i^{N_k}$ stems from the discretization of the integral in k-space. If there is no spin splitting, $\langle \mathbf{k}^F \rangle = 0$. In the present case, the magnetization is along $\pm\mathbf{x}$ so that $\langle \mathbf{k}^F \rangle = \langle k_y^F \rangle \mathbf{y}$, as in Fig. 5.4. The physics behind this term is quite subtle. The velocity operator

is $\mathbf{v} = \partial_{\mathbf{k}} H/\hbar$, which reduces to $\mathbf{v} = \mathbf{k}/m$ in the free electron model in the *absence* of spin-orbit coupling. Therefore, $\langle k_y^{\mathrm{F}} \rangle$ is a partial measure of the spin galvanic effect induced by the symmetry breaking revealed when the magnetization lies away from a high symmetry direction. Notice that $\langle k_y^{\mathrm{F}} \rangle$ is *not* the total spin galvanic effect, which should contain the anomalous velocity term (proportional to the non-equilibrium spin density) and vanishes at equilibrium. The calculated $\langle k_y^{\mathrm{F}} \rangle$ is reported on Fig. 5.8(b) for different substrates. While it is quite small in the case of $4d$ metals, it is much larger for $5d$ metals. In both cases maximum is reached for $[ds]^{10}$ configurations, that corresponds to Pd and Pt substrates.

Since the electronic states at the Fermi level are delocalized, they are more likely to be affected by the interfacial potential gradient $\nabla_z V$ due to the charge transfer. The charge transfer scales with the strength of the orbital hybridization, and results in an enhancement of the orbital angular momentum on the substrate as reported on Fig. 5.3(b). Park *et al.* [85] proposed that at a surface, the local orbital momentum in the presence of surface normal electric field (due to inversion symmetry breaking) results in Rashba-type splitting. Following this idea, we assume that the strength of the band splitting for the X/Co bilayers should be proportional to $\sum_i \xi_i L_i$, where L_i and ξ_i, are atomic orbital moment [Fig. 5.3(b)] and spin-orbit coupling constant [Fig. 5.1(b)], respectively, in each layer i. The quantity $\sum_i \xi_i L_i$ for the X/Co interfaces is displayed on Fig. 5.8(b) (open red symbols) and shows good correlation with $\langle k_y^{\mathrm{F}} \rangle$. However, $\sum_i \xi_i L_i$ is shifted with respect to $\langle k_y^{\mathrm{F}} \rangle$ and is always positive while $\langle k_y^{\mathrm{F}} \rangle$ reaches negative values for some of the X/Co interfaces. We find that this shift can be eliminated by replacing the total orbital moment L_i by the *induced* orbital moment $L_i^{ind} = L_i - L_i^{bulk}$, where L_i^{bulk} is the value of the orbital momentum in the bulk of layer i (either bulk X or bulk Co). Quantity $\sum_i \xi_i L_i^{ind}$ is displays on Fig. 5.8(b) (filled red symbols) and shows an excellent correlation with $\langle k_y^{\mathrm{F}} \rangle$, i.e. $\langle k_y^{\mathrm{F}} \rangle \approx \eta \sum_i \xi_i L_i^{\mathrm{ind}}$, where $\eta\mu_B \approx 10.7$ $(\mathrm{eVnm})^{-1}$ (calculated in this work). Thus, the presence of the

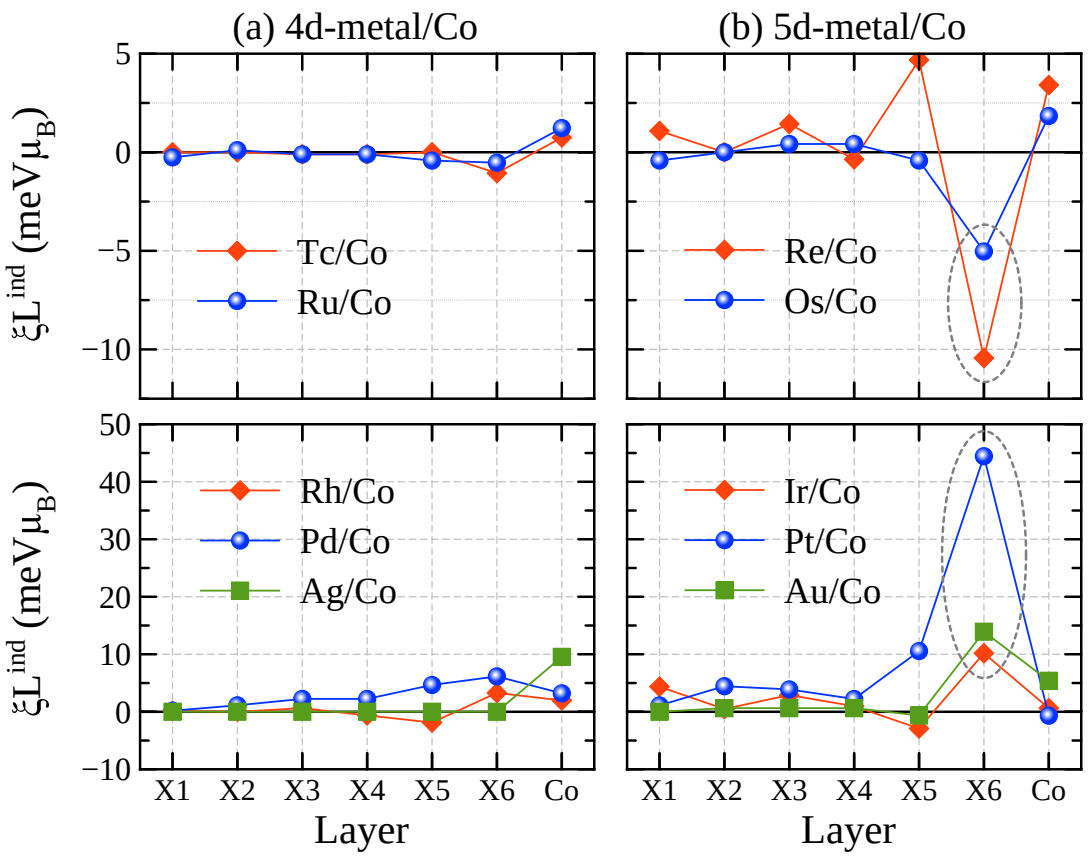

Figure 5.9: Induced orbital moment weighted by spin-orbit coupling for: (a) 5*d*-metal/Co and (b) 4*d*-metal/Co interfaces. Induced orbital moment for each i is $L_i^{ind} = L_i^{X/Co} - L_i^{bulk}$.

induced orbital moment is a necessary condition for the onset of k-asymmetric band splitting.

In order to complete our description of the physics involved, we present the layer contribution of $\xi_i L_i^{\rm ind}$ in Fig. 5.9. First we note that the substrate contribution to the band splitting is large in the case of 5*d*-metals while in the case of 4*d*-metals it is comparable with Co contribution. For instance, at the Ag/Co interface, Ag is not magnetized ($L_{Ag}^{ind} = 0$) thus the main contribution comes from Co. At the Pd/Co interface in contrast, the induced orbital momentum of Pd does not vanish away from the interface [see Fig. 5.3(b)]. Thus Pd/Co interface has the largest strength of the band splitting among other 4*d*-metal/Co interfaces [see Fig. 5.8(b)]. Regarding 5*d*-metal/Co interfaces, the largest $\xi_i L_i^{\rm ind}$ is observed at the Pt/Co interface, associated

with a large induced orbital momentum [see Fig. 5.3(b)]. Moreover, one can see from Fig. 5.9, that the induced orbital momentum of $[ds]^{7-8}$ substrates (Tc, Ru, Re, and Os) is negative while it is positive in the case of $[ds]^{8-10}$ substrates (Rh, Pd, Ag, Ir, Pt, and Au). This nicely correlated with the sign of $\langle k_y^{\mathrm{F}} \rangle$ for the X/Co interfaces reported in Fig. 5.8(b).

We conclude this study by evaluating the effective Rashba parameter resulting from the k-asymmetric band splitting. Although the band structure of X/Co bilayers is much more complex than the free electron model, the Rashba parameter is commonly used in experiments to quantify non-equilibrium properties related to interfacial spin-orbit coupling such as inverse spin galvanic effect. The Rashba parameter at Fermi energy $\langle \alpha^F \rangle$ can be connected with the parameter $\langle k^F \rangle$ defined in Eq. (5.2),

$$\langle \alpha^F \rangle = \frac{\hbar^2}{2} \sum_n^{N_b} \frac{1}{N_k} \sum_i^{N_k} \frac{k_{ni}^F}{m_{ni}^*} \approx \frac{\hbar^2}{2m_e} \langle k^F \rangle. \tag{5.3}$$

The result is shown on Fig. 5.8(b), assuming the same free electron effective mass $m^* = m_e$ for all systems. The largest Rashba parameter is obtained for Pt/Co ($\langle \alpha^F \rangle_{\mathrm{Pt}} \approx 25 \times 10^{-3}$ eV nm) while Ir/Co, Au/Co and Pd/Co have a much smaller parameter ($\approx 5 \times 10^{-3}$ eV nm). These values are smaller than the one reported in Ref. [87] for Pt/Co ($\approx 100 \times 10^{-3}$ eV nm). These estimations must be handled with sane skepticism (in realistic metals, $m^* \ll m_e$, and lattice distortions are disregarded in our calculations) but can be compared with the effective parameters extracted experimentally from current-driven field measurements, i.e. 100 $\times 10^{-3}$ eV nm for Pt/Co [18, 19, 197], and 36 $\times 10^{-3}$ eV nm for Pd/Co/Pd asymmetric interfaces [76, 200–204].

5.4 Discussion and Conclusion

In this work, we systematically studied the band splitting originating from spatial inversion symmetry breaking in the presence of spin-orbit coupling in transition metal bilayers involving $4d$ (Tc, Ru, Rh, Pd, and Ag) and $5d$ (Re, Os, Ir, Pt, and Au) heavy metals, capped by a monolayer of Co. Our results emphasize the limits of the Rashba scenario at crystalline interfaces involving strong interfacial orbital overlaps. Indeed, the k-asymmetric spin splitting is in general *not linear* in k and depends on the band index, and spin splitting is also obtained when the magnetization lies perpendicular to the interface, due to in-plane crystalline symmetry breaking [Fig. 5.6(d)]. Notwithstanding the crystalline symmetries, the overall angular variation of the k-asymmetric spin splitting displays remarkable similarities with what is expected from the much simpler Rashba model (Fig. 5.7). Finally, our study reveals the crucial role of interfacial orbital overlap in the onset of k-asymmetric spin splitting and a phenomenological correlation between the splitting strength and the spin-orbit coupling-weighted induced orbital momentum as well as d-orbital charge transfer (Fig. 5.8).

Chapter 6

Impact of Lattice Mismatch on the Rashba Band Splitting

In this section we study the impact of lattice mismatch on the Rashba band splitting at an Au/Co interface with non-parabolic band structure by first principles calculations. We first address a coherent interface, which is the standard computational approach because of its low computational costs. However, this model loses accuracy in the case of large lattice mismatch. We therefore also study an incoherent interface with Moiré pattern, which provides a much more accurate description but requires a computationally demanding treatment of a large supercell. It turns out that the realistic incoherent model yields a strongly reduced Rashba band splitting. In addition, a comparison of the two models is used to demonstrate proportionality to the orbital moment of Co. Both models show Rashba band splitting also for out-of-plane magnetization. However, for the incoherent model this effect is largely compensated by the presence of the Moiré pattern.

6.1 Introduction

Interfaces play a key role in todays world of nanotechnology that constantly demands higher speed (in data recording and transmission, for example), lower energy

consumption, and reduced size, heating, and material degradation. These demands make it more and more important to account for quantum effects, which show up regularly at surfaces and interfaces, giving rise to an incredible variety of novel physical phenomena. At the nanoscale the properties of interfaces dominate those of the bulk compounds and therefore affect the performance of materials in multiple ways. An illustrative example are interfaces between heavy metals and transition metal ferromagnets, where broken inversion symmetry in combination with the large spin-orbit coupling of the heavy metals can result in spin splitting of an electron gas, a phenomenon called Rashba effect [15, 61]. The spin splitting enables the accumulation and therefore manipulation of the electron spins via small electric fields, which has great potential in logic [62] and memory [27] devices.

Traditionally, the Rashba effect is attributed to materials with free electrons, being characterised by a linear shift of the energy bands in k space [15],

$$E^{\pm} = \frac{\hbar^2 k^2}{2m} \pm \alpha_R k, \tag{6.1}$$

where α_R is the Rashba parameter (describing the magnitude of the spin-orbit splitting) and $\pm$ denotes the spin direction. The Rashba parameter is given by

$$\alpha_R = \frac{\Delta E}{2k} = \frac{\hbar^2}{2m^*}\Delta k, \tag{6.2}$$

where $\Delta E = E^+ - E^-$ and m^* is an effective mass. For parabolic bands with $m^* = \hbar^2(\frac{d^2E}{dk^2})^{-1}$ the band shift is $\Delta k = k^+ - k^- = 2m^*\alpha_R = constant$. Such a splitting has been confirmed experimentally for semiconductors [74–78] and a number of metallic surfaces [64, 66, 67, 79–84].

Significant insights in the Rashba effect have been obtained by first principles calculations. For instance, it has been shown that α_R is proportional, simultaneously, to the spin-orbit coupling and gradient of the surface potential [63]. The electric field

normal to the surface interacts with the electric dipole created by the orbital moment, to yield Rashba band splitting [85]. The role of the asymmetry of the wavefunction has been highlighted in Ref. [86]. While first principles calculations do provide insight in materials with largely free electrons and well isolated surface/interface states (such as the Au(111) [64] and Ir(111) [84] surfaces and the Bi/Ag(111) interface [80]), many metallic surfaces and interfaces have non-parabolic bands and their states hybridize with bulk states, see for example Ref. [81, 87]. In addition, the value and sign of the Rashba parameter can vary from band to band due to band-specific chiral ordering of the orbital moment [87, 88].

Another serious problem for computational studies of the Rashba effect at metallic interfaces is the typically large lattice mismatch, which amounts for the Au/Co and Pt/Co interfaces, for example, to 16% and 13%, respectively. Nevertheless, the state-of-the-art methodology is the coherent model that neglects the lattice mismatch [63, 85–88]. We study in this context the Rashba effect at the Au/Co interface, which is characterized by a complex electronic structure. To quantify the Rashba band splitting, we use a computational approach that takes into account the interfacial lattice mismatch.

6.2 Interface models and computational details

We build coherent (5×5)Au/(5×5)Co and incoherent (5×5)Au/(6×6)Co supercells, see Fig. 6.1. Both models have 25 Au atoms per layer but the Co density is different (25 versus 36 Co atoms per layer). The incoherent model (Moiré pattern) has a small lattice mismatch of only 1.3%, as compared to 16.5% in the case of the coherent model. First principles calculations are performed using the linearized augmented plane wave pseudopotential method [132] and the generalized gradient approximation [103]. Scalar and fully relativistic calculations, respectively, are employed to optimize

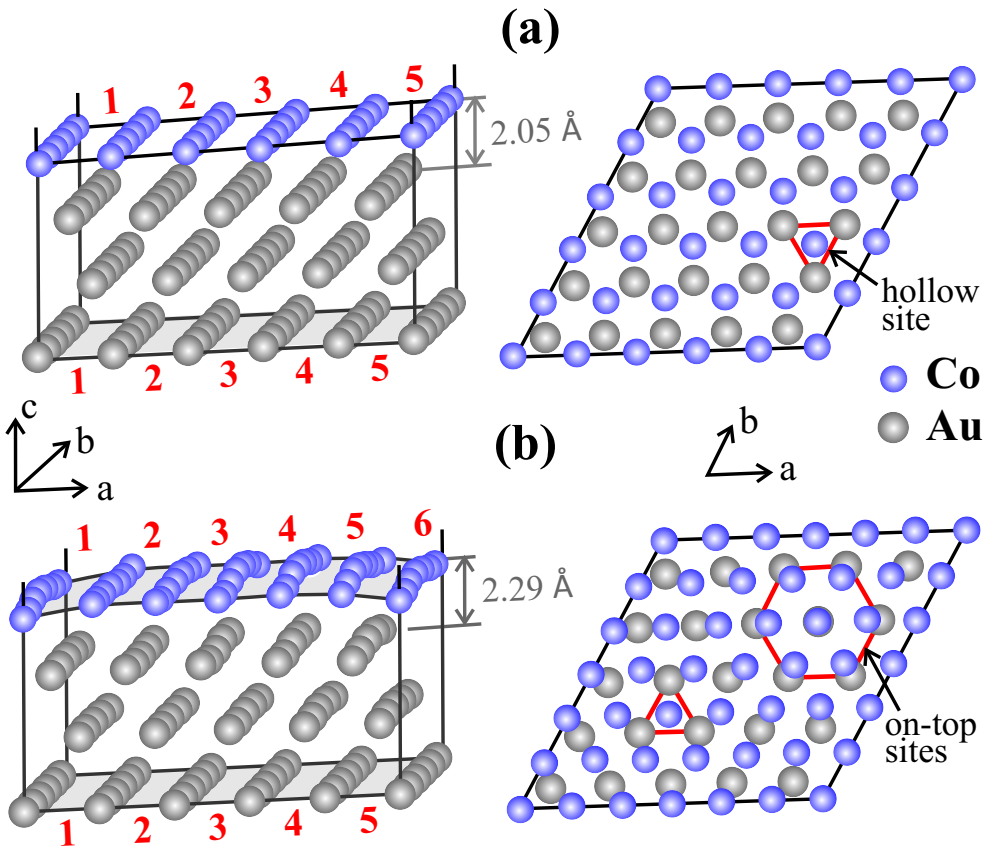

Figure 6.1: Side (left) and top (right) views of the (a) coherent and (b) incoherent models of the Au/Co interface. The distances given in the figure are average distances between the atomic layers forming the interface. Red numbers count the Au and Co unit cells.

the interface geometry and to determine the electronic structure, using k-meshes of $2\times2\times2$ and $4\times4\times1$ points. To study the Rashba band splitting with higher resolution the k-mesh is refined to comprises 32 points in each direction of the Brillouin zone. The plane wave cutoff energy is set to 400 eV.

6.3 Rashba band splitting for coherent and realistic interfaces.

6.3.1 Complex electronic structure and computational approach

To highlight the difficulties of studying the Rashba effect at 5d/3d metal interfaces, we plot in Fig. 6.2 the electronic band structure of the (5×5)Au/(5×5)Co interface. We first note that the bands are not parabolic so that Eq. 6.2 cannot be used to calculate α_R. Moreover, ΔE and Δk change their signs frequently as a result of the complex band structure. Therefore, we search for correlations between quantities related to the Rashba effect (such as the orbital moment, potential gradient, and spin-orbit coupling [63, 85]) and the band splitting by considering the absolute values $|\Delta E|$ and $|\Delta k|$. More specifically, for direction β in the Brillouin zone, see Fig. 6.3 (a), we evaluate the area enclosed by split occupied bands, see Fig. 6.3 (b),

$$|\mathcal{A}(\beta)| = \sum_b \sum_i |\Delta E_{bi}(\beta)| \Delta k_{bi}(\beta) \tag{6.3}$$

and the band shift at the Fermi level, see Fig. 6.3 (c),

$$|\Delta k^F(\beta)| = \sum_b \sum_i |\Delta k^F_{bi}(\beta)|. \tag{6.4}$$

The first summation runs over the band index b and the second over equidistant points from Γ to the boundary of the Brillouin zone in direction β. Both $|\mathcal{A}(\beta)|$ and $|\Delta k^F(\beta)|$ equal zero if there is no band splitting.

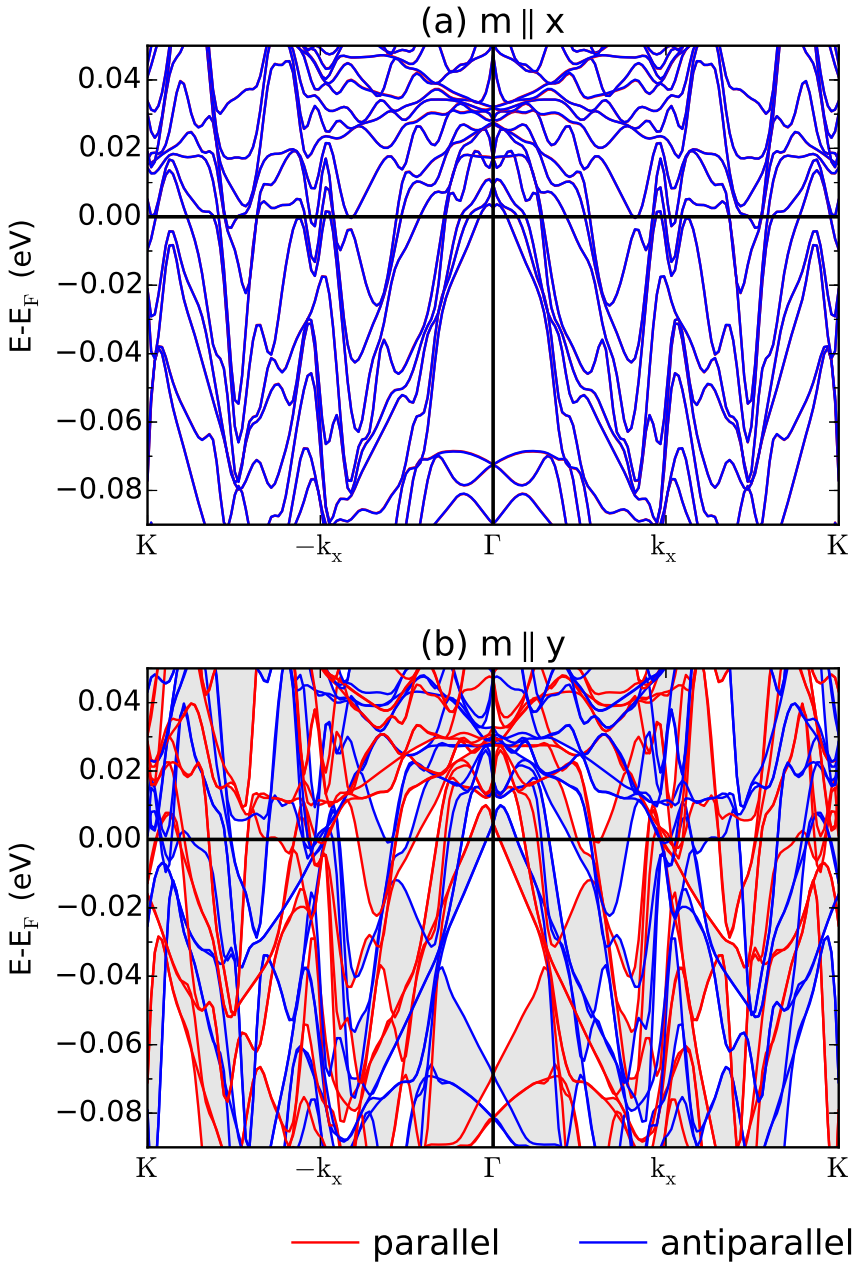

Figure 6.2: Band structure of the (5×5)Au/(5×5)Co interface for magnetization along the (a) $\pm x$ axis and (b) $\pm y$ axis. Grey shades highlight the area enclosed by split bands.

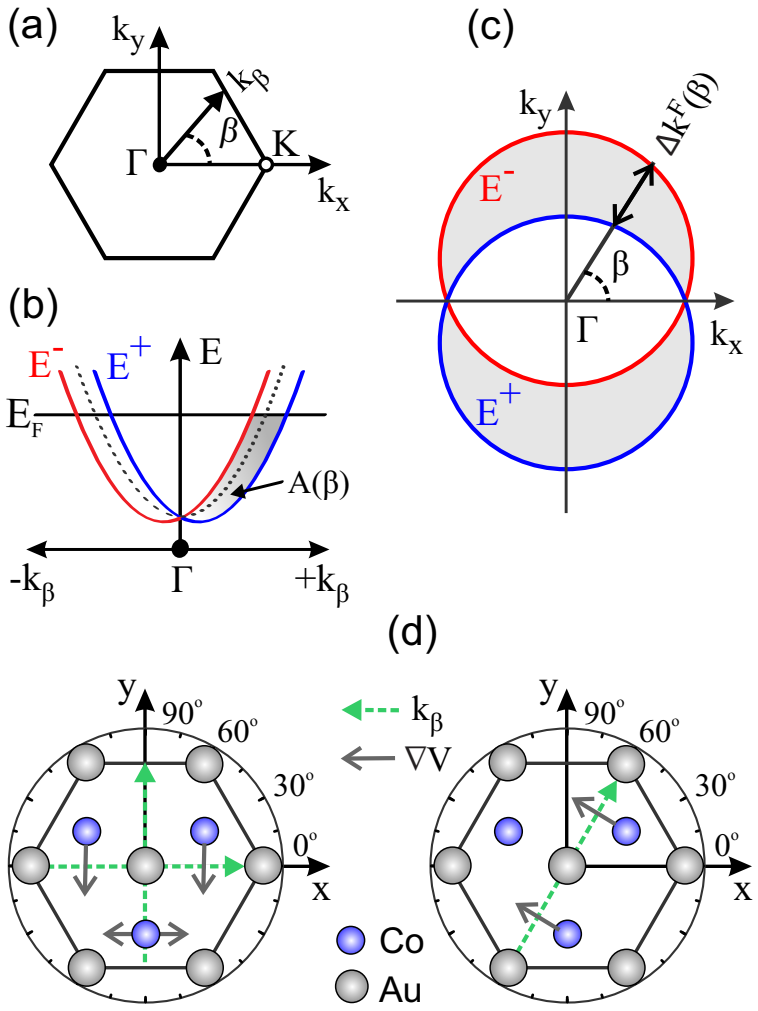

Figure 6.3: (a) Brillouin zone, (b) band splitting, and (c) band shift. Blue and red color has the same meaning as in Fig. 6.2. (d) In-plane projection of the Au/Co interface. The electron propagation (k_β) and potential gradient (∇V) are orthogonal.

6.3.2 Rashba band splitting as a function of the magnetization and electron propagation directions

The angular dependences of $|\mathcal{A}(\beta)|$ and $|\Delta k^F(\beta)|$ are shown in Figs. 6.4 (a) and (b) for (left) in-plane and (right) out-of-plane magnetization. We first note that the results for the coherent and incoherent models are qualitatively similar but the band splitting is much smaller for the latter, which we will explain below. For both magnetization directions the findings for $|\mathcal{A}(\beta)|$ and $|\Delta k^F(\beta)|$ resemble the standard Rashba picture with maximal (zero) band splitting when the electron propagation

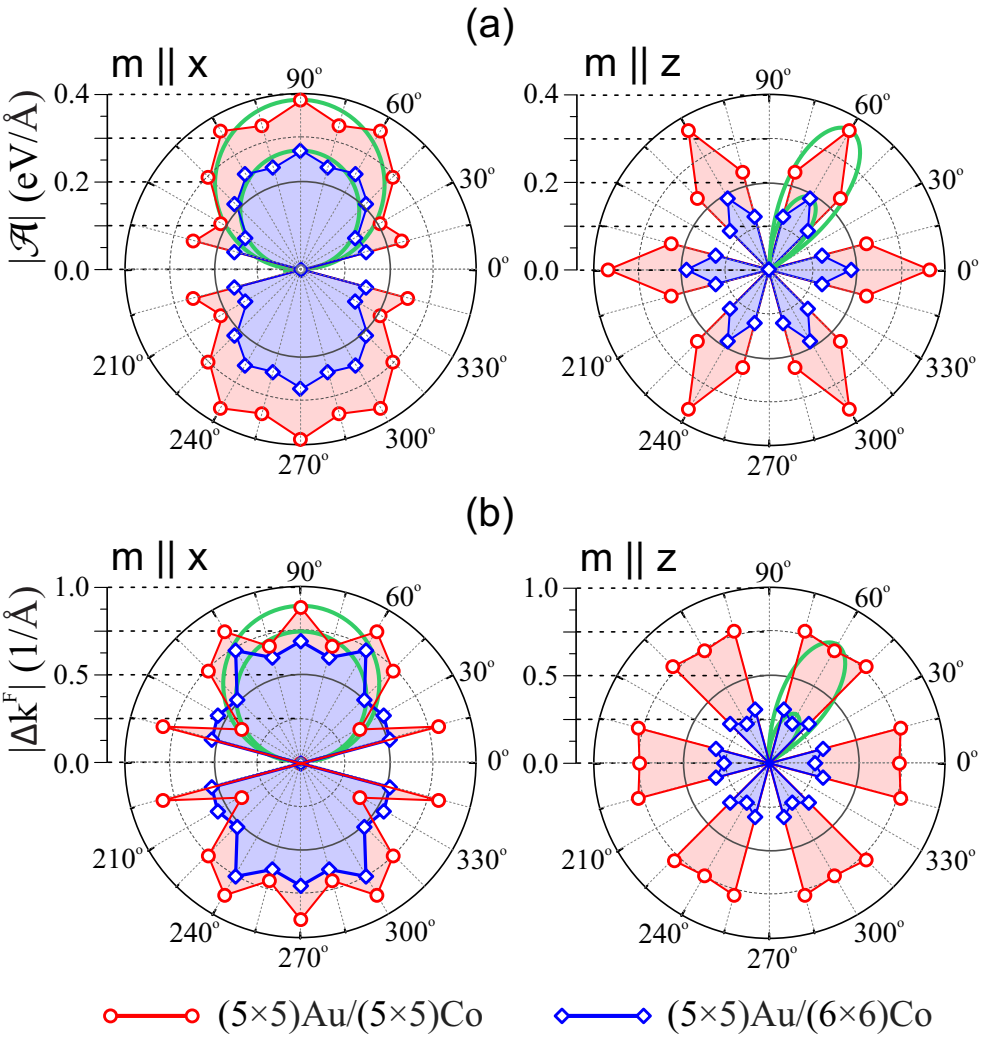

Figure 6.4: (a) $|\mathcal{A}(\beta)|$ and (b) $|\Delta k(\beta)|$ for magnetization along the x (left) and z (right) axis. Green lines represent the standard Rashba splitting $|\mathcal{A}(\beta)| \propto \sin(n\beta+\gamma)$ and $|\Delta k^F(\beta)| \propto \sin(n\beta+\gamma)$, where $n = 1$ ($n = 3$) and $\gamma = 0°$ ($\gamma = 90°$) for in-plane (out-of-plane) magnetization.

is normal (collinear) to the magnetization and (or) electric field. For in-plane magnetization we have $|\mathcal{A}(\beta)|$, $|\Delta k^F(\beta)| \propto \sin(\beta)$, see the left panels of Figs. 6.4 (a) and (b). On the other hand, for out-of-plane magnetization there are strong effects of the crystal symmetry, see Fig. 6.3 (d). When the electron moves in a symmetric direction ($\beta = 30°, 90°, ...$) there is no band splitting, whereas the band splitting is large when the in-plane component of the electric field normal to its propagation is high ($\beta = 0°, 60°, ...$). Therefore, we have for out-of-plane magnetization $|\mathcal{A}(\beta)|$, $|\Delta k^F(\beta)| \propto \sin(3\beta + 90°)$, see the right panels of Figs. 6.4 (a) and (b). In general, $|\mathcal{A}(\beta)|$ shows a better correspondence to the standard Rashba model than $|\Delta k^F(\beta)|$.

6.3.3 Rashba band splitting and magnetism as a functions of Co density

In Ref. [85] it was shown that the orbital moment yields an electric dipole, which interacts with the surface electric field and results in Rashba band splitting. One thus may assume that the Rashba band splitting is proportional to the orbital moment. In order to check this hypothesis, we address in Fig. 6.5 the interdependence between the Rashba band splitting ($|\mathcal{A}(\beta)|$ and $|\Delta k^F(\beta)|$) and the Co orbital moment L_{Co} as a function of the Co density. We find indeed an excellent correlation of both $|\mathcal{A}(\beta)|$ and $|\Delta k^F(\beta)|$ with L_{Co} for both in-plane and out-of-plane magnetization, whereas we do not observe any correlation with the Au orbital moment L_{Au}, as it is much smaller than L_{Co} (for the coherent model we have $L_{\mathrm{Au}} = 0.02\ \mu_B$ and $L_{\mathrm{Co}} = 0.18\ \mu_B$) and hardly depends on the Co concentration (changes only by 2% between the two models) in contrast to $|\mathcal{A}(\beta)|$ and L_{Co}, see Fig. 6.5.

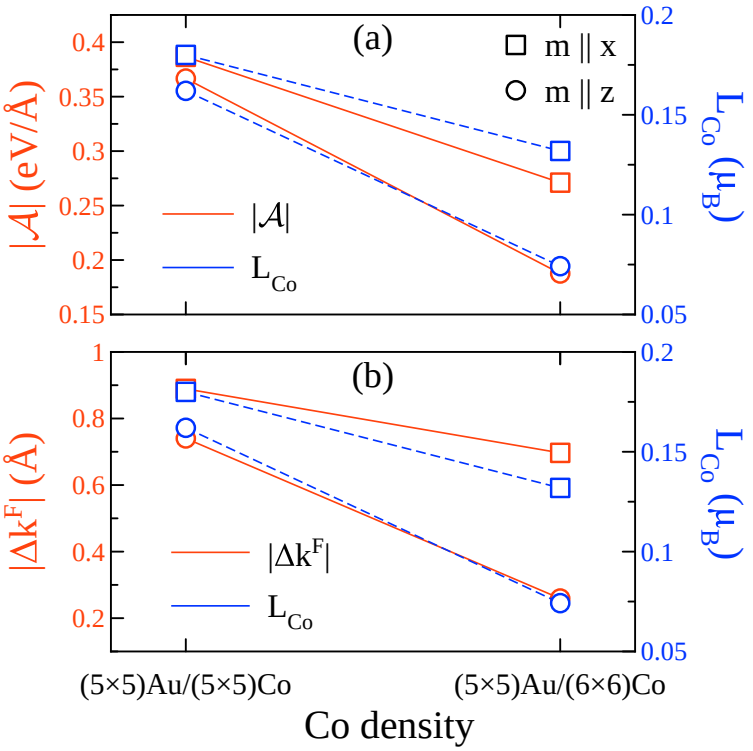

Figure 6.5: Interdependences between (a) $|\mathcal{A}(\beta)|$ and L_{Co}, (b) $|\Delta k^F(\beta)|$ and L_{Co} as functions of the Co density (coherent or incoherent model), for in-plane and out-of-plane magnetization.

6.3.4 Sign of the Rashba band splitting

Since also the sign of the band splitting is important for the Fermi electrons, the dependence of $\Delta k^F(\beta) = \sum_b \sum_i \Delta k^F_{bi}(\beta)$ on the directions of the electron propagation and magnetization is addressed in Fig. 6.6. Because of the complex band structure, the effective electron mass m^* varies throughout the Brillouin zone in absolute value and even sign. This requires an angular dependence of $\Delta k^F(\beta)$ that is not proportional to $\sin(\beta)$, in contrast to $|\mathcal{A}(\beta)|$ and $|\Delta k^F(\beta)|$. Sign changes of the band splitting lead to a compensation of $|\Delta k^F(\beta)|/\Delta k^F(\beta) \approx 5$ (by comparison of Figs. 6.4 and 6.6; zero compensation would correspond to a ratio of 1 and is ideal for applications). It is interesting to note that for out-of-plane magnetization the sign of $\Delta k^F(\beta)$ can be opposite for symmetric directions, see Fig. 6.6 (b), for example, $\Delta k^F(0°) = -\Delta k^F(60°)$ and $\Delta k^F(15°) = -\Delta k^F(45°)$. This fact is understood by the in-plane projection of

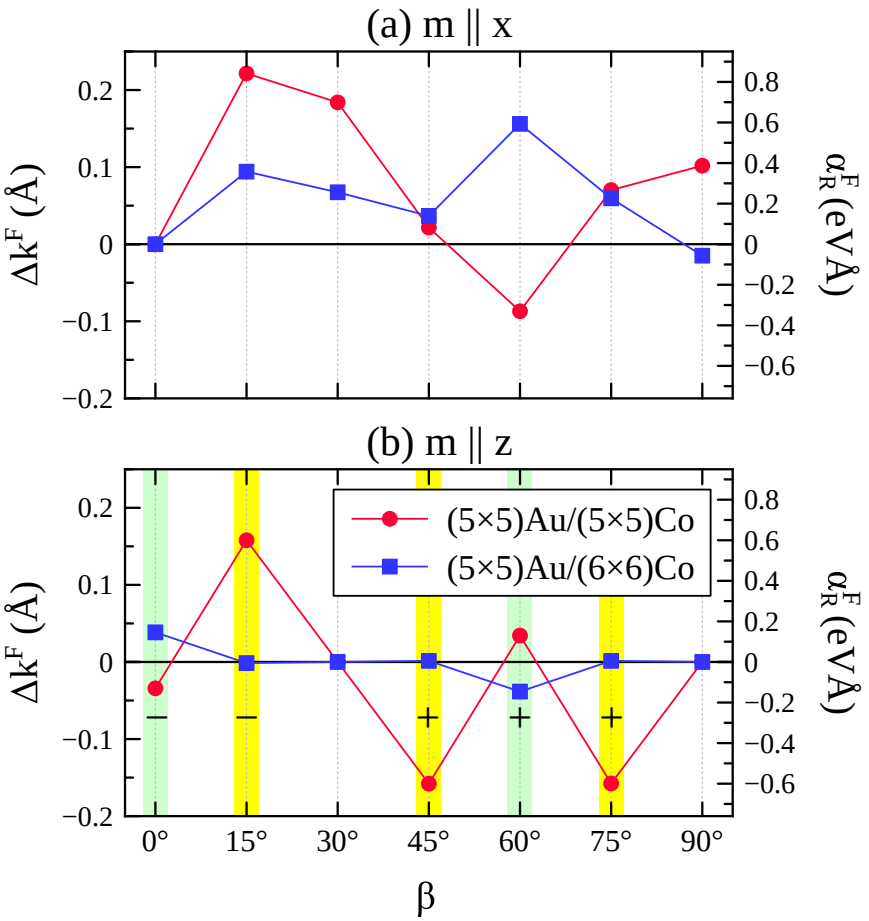

Figure 6.6: $\Delta k^F(\beta)$ for the coherent and incoherent models for magnetization along the (a) x and (b) z axis. The symbols $\pm$ in (b) indicate a positive/negative potential gradient normal to the electron propagation and the magnetization. Colored areas represent structurally equivalent directions: $\Delta k^F(0°) = -\Delta k^F(60°)$, $\Delta k^F(15°) = -\Delta k^F(45°) = -\Delta k^F(75°)$, and $\Delta k^F(30°) = \Delta k^F(90°) = 0$.

the electric field component (created between the Au and Co atoms) normal to the electron propagation, see Fig. 6.3 (d), which vanishes on average in the case of the incoherent model due to the Moiré pattern, so that $\Delta k^F(\beta)$ also vanishes. Using the free electron mass m_e in Eq. 6.2, we obtain a lower bound for the Rashba parameter of the Fermi electrons,

$$\alpha_R^F(\beta) = \frac{\hbar^2}{2m_e} \sum_b \sum_i \Delta k_{bi}^F(\beta) \quad . \tag{6.5}$$

The right axes in Figs. 6.6 show results for the coherent and incoherent models. For in-plane (out-of-plane) magnetization α_R^F changes from 0.8 (0.6) to -0.4 (-0.1) eVÅ, which is a realistic range, since for the Au(111) surface experiments give $\alpha_R = 0.3$ eVÅ [65].

6.4 Summary

In conclusion, we have studied the Rashba band splitting for two models of the Au/Co interface: 1) The popular coherent model that does not take into account the large lattice mismatch of 16% and 2) the incoherent model that is based on a Moiré pattern and thus resolves the issue of the lattice mismatch but is computationally very costly due to the large size of the required supercell. We have analysed the bands below and at the Fermi level and have shown that the incoherent model results in a strongly reduced Rashba band splitting. From the methodological point of view, this is very important, because it demonstrates that the coherent model does not describe the physical properties of the interface correctly. In addition, comparison of the coherent (lower Co density) and incoherent (higher Co density) models allows us to conclude that a reduction of the Co density at the interface due to Co defects is an effective method for enhancing the Rashba band splitting.

It turns out that the complex band structure of the Au/Co interface results in a strong compensation of the Rashba band splitting. For out-of-plane magnetization the latter almost vanishes for the incoherent model, because the average in-plane component of the electric field from the potential gradient between the Au and Co atoms is small in the presence of a Moiré pattern. The dependence of the Rashba band splitting on the electron propagation and magnetization directions is similar for the two models (below and at the Fermi level). For in-plane and out-of-plane magnetization the Rashba band splitting is proportional to $\sin(\beta)$ and $\sin(3\beta + 90°)$,

respectively, which agrees with the standard Rashba model (β being the angle between the electron propagation and magnetization in the first case and that between the electron propagation and in-plane component of the electric field in the second case). Importantly, our results demonstrate that the Rashba band splitting is proportional to the orbital moment of Co, which substantiates previous speculations.

Chapter 7

Conclusion and Outlook

Rapid development of devices and applications requires new materials allowing higher speed (in data recording and transmission, for example), lower energy consumption, and reduced size, heating, and material degradation. Magnetic interfaces are vital components for the next generation of spintronic memory and logic devices. Incredible variety of quantum phenomena show up at the magnetic interfaces allowing combined control of the electron and spin currents by applying an electric field that consumes less energy and can be implemented in much smaller dimensions compare to the traditional semiconductor devices. For example, studied in this work interfaces between transition metal ferromagnets and heavy metals display spin Hall [13] and Rashba [15] effects, which in presence of very small electrical current can switch magnetization in ferromagnets due to spin-orbit torque [8, 10, 11, 16]. Also, those interfaces reveal domain wall motion [19, 26] due to antisymmetric exchange (Dzyaloshinskii-Moriya interaction), which enables new concepts for memory and logic devices [27]. Spin galvanic and inverse spin galvanic effects allow charge-to-spin and spin-to-charge conversions, respectively [214]. Second type of the magnetic interfaces presented in this thesis, AFM/FM interfaces, show perpendicular exchange bias [123], a phenomena that found a great implication for ultra-high density perpendicular recording media [215].

Despite the many appealing characteristic properties of these materials, funda-

mental understating of their microscopic properties and related phenomena need to be thoroughly investigated and established. In this work we have shown that large lattice mismatch between interface compounds modifies the structure and magnetic properties of an interface significantly, demonstrating that the coherent model will not give valid results. The same applies to the standard supercell approach with constant atomic density. We therefore propose a model based on a Moire pattern that includes a transition layer at the interface and demonstrate that it gives results very close to the experimental situation.

For the CoO/Ni interface, the large lattice mismatch has been addressed to the large supercell with 5×5 CoO and 6×6 Ni unit cells. Assuming that the interface Ni atoms and Ni atoms in the next layer occupy at least one hollow site, we have classified the possible configurations of the interface structure. The calculated values of the binding energy and the work of adhesion show that the interface is most stable if there are 5×5 Ni atoms in contact with 5×5 O atoms, instead of the 6×6 atoms as expected from the bulk. The next Ni layer is a transition layer which interpolates between layers of 5×5 and 6×6 Ni atoms and enhances the stability of the interface if it partially reflects the structures of both these layers. The transition layer is found to optimally comprise 31 Ni atoms. The obtained electronic structures show that the interface Ni atoms become more and more metallic and their magnetic moments decrease when the number of Ni atoms at the interface grows from 25 to 36. The experimental evidence that the interface Ni atoms are oxidized is consistent with our result that there are only 25 Ni atoms in the interface. Moreover, if Co instead of O terminates the CoO, the next layer can be expected to be a transition layer with 31 Ni atoms. Our results for the prototypical CoO(111)/Ni(111) interface demonstrate the possible effects of a varying atomic density, i.e., of the optimization of the chemical bonding, at interfaces between solids with significant lattice mismatch. In real interfaces there is in addition the possibility to have defects, which can modify

the picture.

Also, a supercell containing different numbers of CoO and Py unit cells and a transition layer of intermediate atomic density is reasonable to correctly describe the bulk-like regions of the CoO/Py interface. However, when one approaches the interface itself the experimental and calculated values of the magnetization deviate considerably. For instance, while experiment demonstrates the bulk-like Py region magnetization of 700 emu/cm^3 increases to 800 emu/cm^3 at the interface with CoO Ref. [39] and 90% of its Co atoms are coupled ferromagnetically to Py atoms, our calculations show that bulk-like Py region magnetization of 848 emu/cm^3 decreases to 320 ± 66 emu/cm^3 at the O-terminated interface due to the AFM coupling, and increases to 1189 $\pm$31 emu/cm^3 due to ferromagnetic coupling at the Co-terminated interface. This discrepancy indicates the presence of O-vacancies and interface intermixing as to be expected for finite temperature. The above-mentioned magnetizations for two interfaces (O- and Co-terminated) clearly show that the increasing of the O-vacancies will increase interface magnetization from -320 to 1189 ± 31 emu/cm^3. At the same time, our result indicates a small probability of the O diffusion into bulk-like Py region, but high chances for the Fe atoms to be localized at the interface. Understanding of the thermal processes leading to the interface disorder would be welcome and could be realized by molecular dynamics simulations. However, this approach requires an enormous amount of computational resources due to the significant lattice mismatch that needs to be taken into account.

For the Pt/Co and Au/Co interfaces we find that depending on the substrate and thickness of the Co film, the Co atomic density near the interface is different. While the atomic density and surface roughness for a single Co layer on top of Au are found to be large, due to the weak Au-Co and strong Co-Co interaction, additional Co layers result in lower atomic density and surface roughness. Very similar thickness dependence is observed for Pt/Co, for which an increasing thickness additionally

causes the formation of a transition layer. In this layer, the atoms partially occupy energetically favorable sites of both the neighboring Pt and Co layers. Formation of a transition layer in Au/Co results only in a small stability gain, since the Au-Co interaction is weaker than the Co-Co interaction. As the interface magnetic properties depend substantially on the employed model, our result demonstrates that a careful selection is critical. The proposed Moiré supercell with transition layer turns out to give excellent results.

After understanding the structural, electric and magnetic properties of the interfaces and impact of lattice mismatch on them we turn our attention toward spin-orbit magnetic phenomena, such as magnetic anisotropy and Rashba band splitting, which are of great interest for spintronic applications. First we study factors that determine the magnetization direction and its absolute value at Au/Co interfaces. Coherent models ignoring the lattice mismatch between Au and Co are found to result in a too small MAE due to the reduced Co density, in contrast to a more realistic structure with Moiré pattern. Increasing the Co thickness from 1 to 2 layers switches the magnetization from in-plane to out-of-plane for both the coherent and incoherent models. Au-Co intermixing leads to out-of-plane orbital moments of the Co atoms in the mixed atomic layers, which start to dominate over the in-plane orbital moments at about 50% intermixing. When 75% of the Co hollow sites at the surface are occupied by O atoms, the magnetic anisotropy is maximal with in-plane easy axis. For further oxidation superexchange results in antiferromagnetic coupling that reduces the total spin, so that the MAE finally vanishes. In general, the magnetic anisotropy and even the magnetization direction depend strongly on structural details. For instance, if a second Co layer occupies fcc instead of hcp hollow sites (which is energetically only slightly less favorable) we obtain in-plane instead of out-of-plane magnetization.

Also, we systematically studied the band splitting originating from spatial inversion symmetry breaking in the presence of spin-orbit coupling in transition metal

bilayers involving 4*d* (Tc, Ru, Rh, Pd, and Ag) and 5*d* (Re, Os, Ir, Pt, and Au) heavy metals, capped by a monolayer of Co. Our results emphasize the limits of the Rashba scenario at crystalline interfaces involving strong interfacial orbital overlaps. Indeed, the k-asymmetric spin splitting is in general *not linear* in k and depends on the band index, and spin splitting is also obtained when the magnetization lies perpendicular to the interface, due to in-plane crystalline symmetry breaking [Fig. 5.6(d)]. Notwithstanding the crystalline symmetries, the overall angular variation of the k-asymmetric spin splitting displays remarkable similarities with what is expected from the much simpler Rashba model (Fig. 5.7). Finally, our study reveals the crucial role of interfacial orbital overlap in the onset of k-asymmetric spin splitting and a phenomenological correlation between the splitting strength and the spin-orbit coupling-weighted by induced orbital momentum as well as d-orbital charge transfer (Fig. 5.8).

In order to understand the impact of lattice mismatch on Rashba band splitting we have studied two models of the Au/Co interface: 1) The popular coherent model that does not take into account the large lattice mismatch of 16% and 2) the incoherent model that is based on a Moiré pattern and thus resolves the issue of the lattice mismatch but is computationally very costly due to the large size of the required supercell. We have analysed the bands below and at the Fermi level and have shown that the incoherent model results in a strongly reduced Rashba band splitting. From the methodological point of view, this is very important, because it demonstrates that the coherent model does not describe the physical properties of the interface correctly. In addition, comparison of the coherent (lower Co density) and incoherent (higher Co density) models allows us to conclude that a reduction of the Co density at the interface due to Co defects is an effective method for enhancing the Rashba band splitting.

It turns out that the complex band structure of the Au/Co interface results in a strong compensation of the Rashba band splitting. For out-of-plane magnetization

the latter almost vanishes for the incoherent model, because the average in-plane component of the electric field from the potential gradient between the Au and Co atoms is small in the presence of a Moiré pattern. The dependence of the Rashba band splitting on the electron propagation and magnetization directions is similar for the two models (below and at the Fermi level). For in-plane and out-of-plane magnetization the Rashba band splitting is proportional to $\sin(\beta)$ and $\sin(3\beta + 90°)$, respectively, which agrees with the standard Rashba model (β being the angle between the electron propagation and magnetization in the first case and that between the electron propagation and in-plane component of the electric field in the second case). Importantly, our results demonstrate that the Rashba band splitting is proportional to the orbital moment of Co, which substantiates previous speculations.

The work accomplished in this thesis can be extended in different aspects:

1. We have demonstrated above, that the interface details such as intermixing, surface oxidation, and thin film thickness have very strong impact on magnetic properties of the interfaces. Thus Rashba band splitting most likely is also strongly modified by those factors and such investigation will have a great interest for both applications and when theoretical results are compared with the experimental.

2. In chapter 5 we have demonstrated the correlation between the Rashba band splitting and induced orbital moment weighted by spin orbit coupling. However, many works show that the Rashba band splitting is proportional to the electric field as well [87, 216–218]. In chapter 6 we have seen compensation of the Rashba band splitting due to sign variation of the in-plane component of the electric field. Thus, understanding of the crystal field contribution to the sign and size of the band splitting at the X/Co interfaces will allow to design new materials, which give smaller compensation of the Rashba band splitting and thus allow to accumulate a higher spin density.

3. So far we have studied Rashba band splitting only for the interfaces between transition metal ferromagnets and heavy metals. However, there are many another magnetic interfaces which are expected to have large Rashba band splitting. Among them can be multiferroics: BiFeO/Pt, BiFeO/Cu, and BiFeO/Al because SOC of Bi is large.

   Interfaces between heavy metals and antiferromagnets, such as Pt/CoO or Pt/NiO might be good candidates as well, because the resulting zero net magnetic moment makes spintronic devices invisible on the outside and the information stored in antiferromagnet would be insensitive to the external magnetic fields. More details about the antiferromagnetic spintronics can be found in Ref. [219]. Also, systems where heavy metal is AFM, such as PtMn/Co/Ni multilayer, Mn_2Au/Co MnIr/Co, PtMn/Al and PtMn/Cu interfaces have a good potential for the application as well [220–222], because the AFM can exert an internal effective field on the adjacent FM through the exchange-bias and easy axis is out-of-plane [35].

   Also, it would of great interest to study the Rashba band splitting for the Antiferromagnetic/Ferroelectric interfaces. For instance, recently it has been demonstrated that the magnetization of the antiferromagnetic FeRh can be controlled by an electric field in FeRh/BaTiO3 heterostructures [223].

4. Electric control of the magnetization in magnetic layers is currently among the most dynamic areas in spintronics due to its potential for memory, logic and data-storage applications [224]. As was demonstrated in Ref. [8] magnetization in ferromagnet can be manipulated due to the spin torque induced by the Rashba spin-orbit and the ferromagnetic exchange interactions. In this work we have studied the Rashba splitting for the X/Co interfaces (where X is 4d or 5d metal) thus it will be of great interest from the application point of view to

calculate the spin-orbit torque for these interfaces as well.

5. Another intriguing phenomena arising from the spin-orbit coupling at the magnetic interfaces is antisymmetric exchange or Dzyaloshinskii-Moriya (DM) interaction [169, 170]. It converts a uniform ferromagnetic ground state to spiral and skyrmion phases. The skyrmion phase is the topological spin texture and it is a good candidate for spintronic devices [225]. Also, DM interaction creates a chiral effective field that can be used for the manipulation of domain walls in ultrathin magnetic films [180]. Recent studies of the domain wall structures indicates a strong DM interaction in ultrathin magnetic films with perpendicular anisotropy [178]. Also, in Ref. [226] it was demonstrated that the DM interaction is large for materials revealing Raahba band splitting and it increases with the spin-orbit coupling strength, but decreases with the spin-polarization of the conduction electrons. Studied in this work X/Co (X = $4d$ or $5d$-metal) interfaces display both large Rashba SOC and out-of-plane magnetization. However, magnetic moment of Co is large and in order to enhance the DM interaction it can be replaced, by elements with smaller magnetic moment, for example, Ni or NiO. The DM interaction can be studied by first principles in combination with the generalized Bloch theorem [227–229].

REFERENCES

[1] M. N. Baibich, J. M. Broto, A. Fert, F. N. Van Dau, F. Petroff, P. Etienne, G. Creuzet, A. Friederich, and J. Chazelas, "Giant Magnetoresistance of (001)Fe/(001)Cr Magnetic Superlattices," Physical Review Letters **61**, 2472 (1988).

[2] G. Binasch, P. Grünberg, F. Saurenbach, and W. Zinn, "Enhanced magnetoresistance in layered magnetic structures with antiferromagnetic interlayer exchange," Physical Review B **39**, 4828 (1989).

[3] J. C. Slonczewski, "Conductance and exchange coupling of two ferromagnets separated by a tunneling barrier," Physical Review B **39**, 6995 (1989).

[4] J. Nogués and I. K. Schuller, "Exchange bias," Journal of Magnetism and Magnetic Materials **192**, 203 (1999).

[5] H. Yoda, T. Kishi, T. Nagase, M. Yoshikawa, K. Nishiyama, E. Kitagawa, T. Daibou, M. Amano, N. Shimomura, S. Takahashi, T. Kai, M. Nakayama, H. Aikawa, S. Ikegawa, M. Nagamine, J. Ozeki, S. Mizukami, M. Oogane, Y. Ando, S. Yuasa, K. Yakushiji, H. Kubota, Y. Suzuki, Y. Nakatani, T. Miyazaki, and K. Ando, "High efficient spin transfer torque writing on perpendicular magnetic tunnel junctions for high density MRAMs," Current Applied Physics **10**, e87 (2010).

[6] D. Weller, Y. Wu, J. Stöhr, M. G. Samant, B. D. Hermsmeier, and C. Chappert, "Orbital magnetic moments of Co in multilayers with perpendicular magnetic anisotropy," Physical Review B **49**, 12888 (1994).

[7] S. Monso, B. Rodmacq, S. Auffret, G. Casali, F. Fettar, B. Gilles, B. Dieny, and P. Boyer, "Crossover from in-plane to perpendicular anisotropy in Pt/CoFe/AlO x sandwiches as a function of Al oxidation: A very accurate control of the oxidation of tunnel barriers," Applied Physics Letters **80**, 4157 (2002).

[8] A. Manchon and S. Zhang, "Theory of spin torque due to spin-orbit coupling," Physical Review B **79**, 094422 (2009).

[9] S. Ikeda, K. Miura, H. Yamamoto, K. Mizunuma, H. D. Gan, M. Endo, S. Kanai, J. Hayakawa, F. Matsukura, and H. Ohno, "A perpendicular-anisotropy CoFeB-MgO magnetic tunnel junction." Nature materials **9**, 721 (2010).

[10] J. C. Slonczewski, "Current-driven excitation of magnetic multilayers," Journal of Magnetism and Magnetic Materials **159**, L1 (1996).

[11] L. Berger, "Emission of spin waves by a magnetic multilayer traversed by a current," Phys. Review B **54**, 9353 (1996).

[12] J. E. Hirsch, "Spin Hall Effect," Physical Review Letters **83**, 1834 (1999), arXiv:0602330 [cond-mat] .

[13] M. I. Dyakonov and V. I. Perel, "Current-induced spin orientation of electrons in semiconductors," Physics Letters A **35**, 459 (1971).

[14] V. M. Edelstein, "Spin polarization of conduction electrons induced by electric current in two-dimensional asymmetric electron systems," Solid State Communications **73**, 233 (1990).

[15] Y. A. Bychkov and E. I. Rashba, "Oscillatory effects and the magnetic susceptibility of carriers in inversion layers," Journal of Physics C: Solid State Physics **17**, 6039 (1984).

[16] L. Liu, C. Pai, Y. Li, H. W. Tseng, D. C. Ralph, and R. A. Buhrman, "Spin-Torque Switching with the Giant Spin Hall Effect of Tantalum," Science **336**, 555 (2012), arXiv:1203.2875 .

[17] V. E. Demidov, S. Urazhdin, H. Ulrichs, V. Tiberkevich, A. Slavin, D. Baither, G. Schmitz, and S. O. Demokritov, "Magnetic nano-oscillator driven by pure spin current," (2012).

[18] I. M. Miron, G. Gaudin, S. Auffret, B. Rodmacq, A. Schuhl, S. Pizzini, J. Vogel, and P. Gambardella, "Current-driven spin torque induced by the Rashba effect in a ferromagnetic metal layer." Nature materials **9**, 230 (2010).

[19] I. M. Miron, T. Moore, H. Szambolics, L. D. Buda-Prejbeanu, S. Auffret, B. Rodmacq, S. Pizzini, J. Vogel, M. Bonfim, A. Schuhl, and G. Gaudin, "Fast current-induced domain-wall motion controlled by the Rashba effect." Nature materials **10**, 419 (2011).

[20] N. Nagaosa and Y. Tokura, "Topological properties and dynamics of magnetic skyrmions," Nature Nanotechnology **8**, 899 (2013).

[21] U. K. Rössler, A. N. Bogdanov, and C. Pfleiderer, "Spontaneous skyrmion ground states in magnetic metals." Nature **442**, 797 (2006), arXiv:0603104 [cond-mat] .

[22] S. Mühlbauer, B. Binz, F. Jonietz, C. Pfleiderer, A. Rosch, A. Neubauer, R. Georgii, and P. Böni, "Skyrmion lattice in a chiral magnet," Science **323**, 915 (2009), http://science.sciencemag.org/content/323/5916/915.full.pdf .

[23] N. Romming, A. Kubetzka, C. Hanneken, K. von Bergmann, and R. Wiesendanger, "Field-dependent size and shape of single magnetic skyrmions," Phys. Rev. Lett. **114**, 177203 (2015).

[24] M. Bode, M. Heide, K. von Bergmann, P. Ferriani, S. Heinze, G. Bihlmayer, a. Kubetzka, O. Pietzsch, S. Blügel, and R. Wiesendanger, "Chiral magnetic order at surfaces driven by inversion asymmetry." Nature **447**, 190 (2007).

[25] S. V. Grigoriev, D. Chernyshov, V. A. Dyadkin, V. Dmitriev, S. V. Maleyev, E. V. Moskvin, D. Menzel, J. Schoenes, and H. Eckerlebe, "Crystal handedness and spin helix chirality in $fe_{1-x}co_xSi$," Phys. Rev. Lett. **102**, 037204 (2009).

[26] K. Ryu, S. Yang, L. Thomas, and S. S. P. Parkin, "Chiral spin torque arising from proximity-induced magnetization." Nature communications **5**, 3910 (2014).

[27] S. S. P. Parkin, M. Hayashi, and L. Thomas, "Magnetic domain-wall racetrack memory," Science **320**, 190 (2008).

[28] S. Emori, U. Bauer, S. Ahn, E. Martinez, and G. S. D. Beach, "Current-driven dynamics of chiral ferromagnetic domain walls," Nature Materials **12**, 611 (2013).

[29] R. H. Liu, W. L. Lim, and S. Urazhdin, "Control of current-induced spin-orbit effects in a ferromagnetic heterostructure by electric field," Physical Review B **89**, 220409 (2014).

[30] J. Yang, H. Li, T. Wu, W. Zhang, L. Chen, and J. Yang, "Evaluation of Half-Heusler Compounds as Thermoelectric Materials Based on the Calculated Electrical Transport Properties," Advanced Functional Materials **18**, 2880 (2008).

[31] H. Kurebayashi, O. Dzyapko, V. E. Demidov, D. Fang, A. J. Ferguson, and S. O. Demokritov, "Controlled enhancement of spin-current emission by three-magnon splitting." Nature materials **10**, 660 (2011).

[32] M. Ohkoshi, K. Tamari, S. Honda, and T. Kusuda, "Microstructure and exchange anisotropy of Co-CoO films with perpendicular magnetization," Journal of Applied Physics **57**, 4034 (1985).

[33] C. Tsang and R. Fontana, "Fabrication and wafer testing of barber-pole and exchange-biased narrow-track MR sensors," IEEE Transactions on Magnetics **18**, 1149 (1982).

[34] B. Dieny, V. S. Speriosu, S. S. P. Parkin, B. A. Gurney, D. R. Wilhoit, and D. Mauri, "Giant magnetoresistive in soft ferromagnetic multilayers," Physical Review B **43**, 1297 (1991).

[35] W. H. Meiklejohn and C. P. Bean, "New magnetic anisotropy," Physical Review **105**, 904 (1957).

[36] H. Kishi, Y. Kitade, Y. Miyake, A. Tanaka, and K. Kobayashi, "Study of exchange-coupled bias field in Ni-Fe/Pd-Pt-Mn thin films," Magnetics, IEEE Transactions on **32**, 3380 (1996).

[37] J. Nogués, D. Lederman, T. J. Moran, I. K. Schuller, and K. V. Rao, "Large exchange bias and its connection to interface structure in FeF2 Fe bilayers," Applied Physics Letters **68**, 3186 (1996).

[38] T. J. Moran, J. Nogués, D. Lederman, and I. K. Schuller, "Perpendicular coupling at Fe-FeF2 interfaces," Applied Physics Letters **72**, 617 (1998).

[39] S. Roy, C. Sanchez-Hanke, S. Park, M. Fitzsimmons, Y. Tang, J. Hong, D. Smith, B. Taylor, X. Liu, M. Maple, A. Berkowitz, C. C. Kao, and S. Sinha, "Evidence of modified ferromagnetism at a buried Permalloy/CoO interface at room temperature," Physical Review B **75**, 014442 (2007).

[40] E. Blackburn, C. Sanchez-Hanke, S. Roy, D. Smith, J. I. Hong, K. Chan, A. Berkowitz, and S. Sinha, "Pinned Co moments in a polycrystalline permalloy/CoO exchange-biased bilayer," Physical Review B **78**, 180408 (2008).

[41] L. Thomas, G. Jan, J. Zhu, H. Liu, Y. J. Lee, S. Le, R. Y. Tong, K. Pi, Y. J. Wang, D. Shen, R. He, J. Haq, J. Teng, V. Lam, K. Huang, T. Zhong, T. Torng, and P. K. Wang, "Perpendicular spin transfer torque magnetic random access memories with high spin torque efficiency and thermal stability for embedded applications (invited)," Journal of Applied Physics **115** (2014), 10.1063/1.4870917.

[42] A. D. Kent and D. C. Worledge, "A new spin on magnetic memories," Nature Nanotechnology **10**, 187 (2015).

[43] T. Cren, S. Rusponi, N. Weiss, M. Epple, and H. Brune, "Oxidation Induced Enhanced Magnetic Susceptibility of Co Islands on Pt(111)," The Journal of Physical Chemistry B **108**, 14685 (2004).

[44] U. Pustogowa, J. Zabloudil, C. Uiberacker, C. Blaas, P. Weinberger, L. Szunyogh, and C. Sommers, "Magnetic properties of thin films of Co and of (CoPt) superstructures on Pt(100) and Pt(111)," Physical Review B **60**, 414 (1999).

[45] M. Björck, G. Andersson, B. Sanyal, M. Hedlund, and A. Wildes, "Segregation and interdiffusion in (Fe,Co)/Pt superlattices," Physical Review B **79**, 085428 (2009).

[46] A. Lehnert, S. Dennler, P. Błoński, S. Rusponi, M. Etzkorn, G. Moulas, P. Bencok, P. Gambardella, H. Brune, and J. Hafner, "Magnetic anisotropy of Fe and Co ultrathin films deposited on Rh(111) and Pt(111) substrates: An experimental and first-principles investigation," Physical Review B **82**, 094409 (2010).

[47] G. Moulas, A. Lehnert, S. Rusponi, J. Zabloudil, C. Etz, S. Ouazi, M. Etzkorn, P. Bencok, P. Gambardella, P. Weinberger, and H. Brune, "High magnetic moments and anisotropies for FexCo1x monolayers on Pt(111)," Physical Review B **78**, 214424 (2008).

[48] L. Meng, R. Wu, L. Zhang, L. Li, S. Du, Y. Wang, and H. J. Gao, "Multi-oriented moiré superstructures of graphene on Ir(111): experimental observations and theoretical models," Journal of physics. Condensed matter : an Institute of Physics journal **24**, 314214 (2012).

[49] R. Decker, J. Brede, N. Atodiresei, V. Caciuc, S. Blügel, and R. Wiesendanger, "Atomic-scale magnetism of cobalt-intercalated graphene," Physical Review B **87**, 041403 (2013).

[50] L. Cagnon, A. Gundel, and T. Devolder, "Anion effect in Co/Au (111) electrodeposition: structure and magnetic behavior," Applied Surface Science **164**, 22 (2000).

[51] L. Cagnon, T. Devolder, R. Cortes, A. Morrone, J. Schmidt, C. Chappert, and P. Allongue, "Enhanced interface perpendicular magnetic anisotropy in electrodeposited Co/Au(111) layers," Physical Review B **63**, 104419 (2001).

[52] P. Grütter and U. Dürig, "Growth of vapor-deposited cobalt films on Pt (111) studied by scanning tunneling microscopy," Physical Review B **49** (1994).

[53] S. H. Shaikhutdinov, R. Meyer, D. Lahav, M. Bäumer, T. Klüner, and H. J. Freund, "Determination of Atomic Structure of the Metal-Oxide Interface: Pd Nanodeposits on an FeO(111) Film," Physical Review Letters **91**, 076102 (2003).

[54] M. Ritter, W. Ranke, and W. Weiss, "Growth and structure of ultrathin FeO films on Pt(111) studied by STM and LEED," Physical Review B **57**, 7240 (1998).

[55] G. X. Miao, J. Y. Chang, M. J. Veenhuizen, K. Thiel, M. Seibt, G. Eilers, M. Münzenberg, and J. S. Moodera, "Epitaxial growth of MgO and Fe/MgO/Fe magnetic tunnel junctions on (100)-Si by molecular beam epitaxy," Applied Physics Letters **93**, 142511 (2008).

[56] B. Újfalussy, L. Szunyogh, P. Bruno, and P. Weinberger, "First-Principles Calculation of the Anomalous Perpendicular Anisotropy in a Co Monolayer on Au(111)," Physical Review Letters **77**, 1805 (1996).

[57] C. Chappert and P. Bruno, "Magnetic anisotropy in metallic ultrathin films and related experiments on cobalt films (invited)," Journal of Applied Physics **64**, 5736 (1988).

[58] P. Beauvillain, A. Bounouh, C. Chappert, R. Mégy, S. Ould-Mahfoud, J. P. Renard, P. Veillet, D. Weller, and J. Corno, "Effect of submonolayer coverage on magnetic anisotropy of ultrathin cobalt films M/Co/Au(111) with M = Au, Cu, Pd," Journal of Applied Physics **76**, 6078 (1994).

[59] P. Bruno and J. P. Renard, "Magnetic surface anisotropy of transition metal ultrathin films," Applied Physics A **506**, 499 (1989).

[60] N. Bhattarai, G. Casillas, S. Khanal, D. Bahena, J. J. Velazquez-Salazar, S. Mejia, A. Ponce, V. P. Dravid, R. L. Whetten, M. M. Mariscal, and M. Jose-Yacaman, "Structure and composition of au/co magneto-plasmonic nanoparticles," MRS Communications **3**, 177 (2013).

[61] E. Rashba, "Properties of semiconductors with an extremum loop .1. cyclotron and combinational resonance in a magnetic field perpendicular to the plane of the loop," Soviet Physics-Solid State **2**, 1109 (1960).

[62] D. A. Allwood, "Magnetic Domain-Wall Logic," Science **309**, 1688 (2005).

[63] L. Petersen and P. Hedegård, "A simple tight-binding model of spinorbit splitting of sp-derived surface states," Surface Science **459**, 49 (2000).

[64] S. LaShell, B. McDougall, and E. Jensen, "Spin Splitting of an Au(111) Surface State Band Observed with Angle Resolved Photoelectron Spectroscopy," Physical Review Letters **77**, 3419 (1996).

[65] H. Cercellier, C. Didiot, Y. Fagot-Revurat, B. Kierren, L. Moreau, D. Malterre, and F. Reinert, "Interplay between structural, chemical, and spectroscopic properties of AgAu(111) epitaxial ultrathin films: A way to tune the rashba coupling," Physical Review B **73**, 195413 (2006).

[66] O. Krupin, G. Bihlmayer, K. Starke, S. Gorovikov, J. Prieto, K. Döbrich, S. Blügel, and G. Kaindl, "Rashba effect at magnetic metal surfaces," Physical Review B **71**, 201403 (2005).

[67] C. Ast, J. Henk, A. Ernst, L. Moreschini, M. Falub, D. Pacilé, P. Bruno, K. Kern, and M. Grioni, "Giant Spin Splitting through Surface Alloying," Physical Review Letters **98**, 186807 (2007).

[68] I. Gierz, B. Stadtmüller, J. Vuorinen, M. Lindroos, F. Meier, J. H. Dil, K. Kern, and C. R. Ast, "Structural influence on the rashba-type spin splitting in surface alloys," Physical Review B **81**, 245430 (2010).

[69] A. Takayama, T. Sato, S. Souma, and T. Takahashi, "Giant out-of-plane spin component and the asymmetry of spin polarization in surface rashba states of bismuth thin film," Physical Review Letters **106**, 7 (2011).

[70] D. Hsieh, D. Qian, L. Wray, Y. Xia, Y. S. Hor, R. J. Cava, and M. Z. Hasan, "A topological Dirac insulator in a quantum spin Hall phase," Nature **452**, 970 (2008).

[71] Y. L. Chen, J. G. Analytis, J. H. Chu, Z. K. Liu, S. K. Mo, X. L. Qi, H. J. Zhang, D. H. Lu, X. Dai, Z. Fang, S. C. Zhang, I. R. Fisher, Z. Hussain, and Z. X. Shen, "Experimental Realization of a Three-Dimensional Topological Insulator, Bi2Te3," Science **325**, 178 (2009).

[72] G. Dresselhaus, "Spin-Orbit Coupling Effects in Zinc Blende Structures," Phys. Rev. **100**, 580 (1955).

[73] H. Nakamura, T. Koga, and T. Kimura, "Experimental Evidence of Cubic Rashba Effect in an Inversion-Symmetric Oxide," Physical Review Letters **108**, 206601 (2012).

[74] D. Stein, K. v. Klitzing, and G. Weimann, "Electron spin resonance on $GaAs - al_xga_{1-x}As$ heterostructures," Physical Review Letters **51**, 130 (1983).

[75] H. Stormer, Z. Schlesinger, A. Chang, D. Tsui, A. Gossard, and W. Wiegmann, "Energy Structure and Quantized Hall Effect of Two-Dimensional Holes," Physical Review Letters **51**, 126 (1983).

[76] D. Fang, H. Kurebayashi, J. Wunderlich, K. Výborný, L. P. Zârbo, R. P. Campion, A. Casiraghi, B. L. Gallagher, T. Jungwirth, and A. J. Ferguson, "Spinorbit-driven ferromagnetic resonance," Nature Nanotechnology **6**, 413 (2011).

[77] K. Ishizaka, M. S. Bahramy, H. Murakawa, M. Sakano, T. Shimojima, T. Sonobe, K. Koizumi, S. Shin, H. Miyahara, A. Kimura, K. Miyamoto, T. Okuda, H. Namatame, M. Taniguchi, R. Arita, N. Nagaosa, K. Kobayashi, Y. Murakami, R. Kumai, Y. Kaneko, Y. Onose, and Y. Tokura, "Giant Rashba-type spin splitting in bulk BiTeI," Nature Materials **10**, 521 (2011).

[78] D. Di Sante, P. Barone, R. Bertacco, and S. Picozzi, "Electric control of the giant Rashba effect in bulk GeTe." Advanced materials (Deerfield Beach, Fla.) **25**, 509 (2013).

[79] M. Hoesch, M. Muntwiler, V. N. Petrov, M. Hengsberger, L. Patthey, M. Shi, M. Falub, T. Greber, and J. Osterwalder, "Spin structure of the shockley surface state on Au(111)," Physical Review B **69**, 241401 (2004).

[80] C. Ast, D. Pacilé, L. Moreschini, M. Falub, M. Papagno, K. Kern, M. Grioni, J. Henk, A. Ernst, S. Ostanin, and P. Bruno, "Spin-orbit split two-dimensional

electron gas with tunable Rashba and Fermi energy," Physical Review B **77**, 081407 (2008).

[81] D. Popović, F. Reinert, S. Hüfner, V. G. Grigoryan, M. Springborg, H. Cercellier, Y. Fagot-Revurat, B. Kierren, and D. Malterre, "High-resolution photoemission on Ag/Au(111): Spin-orbit splitting and electronic localization of the surface state," Physical Review B **72**, 045419 (2005).

[82] G. Nicolay, F. Reinert, S. Hüfner, and P. Blaha, "Spin-orbit splitting of the L-gap surface state on Au(111) and Ag(111)," Physical Review B **65**, 033407 (2001).

[83] Y. U. Koroteev, G. Bihlmayer, J. Gayone, E. Chulkov, S. Blügel, P. Echenique, and P. H. Hofmann, "Strong Spin-Orbit Splitting on Bi Surfaces," Physical Review Letters **93**, 046403 (2004).

[84] A. Varykhalov, D. Marchenko, M. R. Scholz, E. D. L. Rienks, T. K. Kim, G. Bihlmayer, J. Sánchez-Barriga, and O. Rader, "Ir(111) surface state with giant Rashba splitting persists under graphene in air," Physical Review Letters **108**, 1 (2012).

[85] S. R. Park, C. H. Kim, J. Yu, J. H. Han, and C. Kim, "Orbital-Angular-Momentum Based Origin of Rashba-Type Surface Band Splitting," Physical Review Letters **107**, 156803 (2011).

[86] G. Bihlmayer, Y. M. Koroteev, P. M. Echenique, E. V. Chulkov, and S. Blügel, "The Rashba-effect at metallic surfaces," Surface Science **600**, 3888 (2006).

[87] J. Park, C. H. Kim, H. Lee, and J. H. Han, "Orbital chirality and Rashba interaction in magnetic bands," Physical Review B **87**, 041301 (2013).

[88] P. M. Haney, H. Lee, K. Lee, A. Manchon, and M. D. Stiles, "Current-induced torques and interfacial spin-orbit coupling," Physical Review B **88**, 214417 (2013).

[89] M. Born and R. Oppenheimer, "Zur quantentheorie der molekeln," Annalen der Physik **389**, 457 (1927).

[90] P. Geerlings, F. D. Proft, and W. Langenaeker, "Conceptual density functional theory," Chemical Reviews **103**, 1793 (2003).

[91] U. von Barth, "Basic density-functional theoryan overview," Physica Scripta **2004**, 9 (2004).

[92] R. O. Jones, "Density functional theory: Its origins, rise to prominence, and future," Rev. Mod. Phys. **87**, 897 (2015).

[93] C. Fiolhais, F. Nogueira, and M. Marques, eds., *A Primer in Density Functional Theory*, Lecture Notes in Physics, Berlin Springer Verlag, Vol. 620 (2003).

[94] R. M. Martin, *Electronic structure : basic theory and practical methods* (Cambridge University Press, Cambridge, New York, 2004).

[95] D. S. Sholl and J. A. Steckel, *Density functional theory: a practical introduction* (Wiley, 2009).

[96] L. H. Thomas, "The calculation of atomic fields," Mathematical Proceedings of the Cambridge Philosophical Society **23**, 542 (1927).

[97] E. Fermi, "Un metodo statistico per la determinazione di alcune priorieta dell atome," Rend. Accad. Naz. Lincei **6**, 32 (1927).

[98] P. Hohenberg and W. Kohn, "Inhomogeneous electron gas," Phys. Rev. **136**, B864 (1964).

[99] W. Kohn and L. J. Sham, "Self-consistent equations including exchange and correlation effects," Phys. Rev. **140**, A1133 (1965).

[100] P. A. M. Dirac, "Note on exchange phenomena in the thomas atom," Proceedings of the Cambridge Philosophical Society **26**, 376 (1930).

[101] D. M. Ceperley and B. J. Alder, "Ground state of the electron gas by a stochastic method," Physical Review Letters **45**, 566 (1980).

[102] J. P. Perdew and Y. Wang, "Accurate and simple analytic representation of the electron-gas correlation energy," Physical Review B **45**, 13244 (1992).

[103] J. P. Perdew, K. Burke, and M. Ernzerhof, "Generalized gradient approximation made simple," Physical Review Letters **77**, 3865 (1996).

[104] T. Bredow and A. Gerson, "Effect of exchange and correlation on bulk properties of MgO, NiO, and CoO," Physical Review B **61**, 5194 (2000).

[105] V. I. Anisimov, F. Aryasetiawan, and A. I. Lichtenstein, "First-principles calculations of the electronic structure and spectra of strongly correlated systems: the LDA+U method," Journal of Physics: Condensed Matter **9**, 767 (1997).

[106] J. Hubbard, "Electron correlations in narrow energy bands. iv. the atomic representation," Proceedings of the Royal Society of London A: Mathematical, Physical and Engineering Sciences **285**, 542 (1965).

[107] U. Bath and L. Hedin, "A local exchange-correlation potential for the spin polarized case." Journal of Physics C: Solid State Physics **5**, 1629 (1972).

[108] O. Gunnarsson and B. I. Lundqvist, "Exchange and correlation in atoms, molecules, and solids by the spin-density-functional formalism," Physical Review B **13**, 4274 (1976).

[109] C. R. Jacob and M. Reiher, "Spin in density-functional theory," International Journal of Quantum Chemistry **112**, 3661 (2012).

[110] J. van Vleck, "On the Anisotropy of Cubic Ferromagnetic Crystals," Physical Review **52**, 1178 (1937).

[111] F. Nogueira, M. Marques, and C. Fiolhais, *A primer in density functional theory*, Lecture Notes in Physics (Springer, Berlin, 2003).

[112] R. M. Martin, *Electronic structure : basic theory and practical methods* (Cambridge University Press, Cambridge, New York, 2004).

[113] X. Gonze and C. Lee, "Dynamical matrices, born effective charges, dielectric permittivity tensors, and interatomic force constants from density-functional perturbation theory," Physical Review B **55**, 10355 (1997).

[114] L. Fernandez-Seivane, M. A. Oliveira, S. Sanvito, and J. Ferrer, "On-site approximation for spinorbit coupling in linear combination of atomic orbitals density functional methods," Journal of Physics: Condensed Matter **18**, 7999 (2006).

[115] D. C. Ralph and M. D. Stiles, "Spin transfer torques," Journal of Magnetism and Magnetic Materials **320**, 1190 (2008).

[116] Y. Fukuma, L. Wang, H. Idzuchi, S. Takahashi, S. Maekawa, and Y. Otani, "Giant enhancement of spin accumulation and long-distance spin precession in metallic lateral spin valves." Nature materials **10**, 527 (2011).

[117] S. Wang and H. Ye, "Theoretical studies of solid - solid interfaces," Current Opinion in Solid State and Materials Science **10**, 26 (2006).

[118] R. Benedek, D. N. Seidman, M. Minkoff, L. H. Yang, and A. Alavi, "Atomic and electronic structure and interatomic potentials at a polar ceramic/metal interface:{222} MgO/Cu," Physical Review B **60**, 94 (1999).

[119] R. Benedek, A. Alavi, D. N. Seidman, L. H. Yang, D. Muller, and C. Woodward, "First Principles Simulation of a Ceramic /Metal Interface with Misfit," Physical Review Letters **84**, 3362 (2000).

[120] X. Wang and J. Smith, "Si/Cu Interface Structure and Adhesion," Physical Review Letters **95**, 156102 (2005).

[121] S. Grytsyuk, F. Cossu, and U. Schwingenschlögl, "Magnetic exchange at realistic CoO/Ni interfaces," The European Physical Journal B **85**, 254 (2012).

[122] T. J. Moran, J. M. Gallego, and I. K. Schuller, "Increased exchange anisotropy due to disorder at permalloy/CoO interfaces," Journal of Applied Physics **78**, 1887 (1995).

[123] T. J. Moran and I. K. Schuller, "Effects of cooling field strength on exchange anisotropy at permalloy/CoO interfaces," Journal of Applied Physics **79**, 5109 (1996).

[124] K. Takano, R. H. Kodama, A. E. Berkowitz, S. Diego, and L. Jolla, "Interfacial Uncompensated Antiferromagnetic Spins : Role in Unidirectional Anisotropy in Polycrystalline $Ni_{81}Fe_{19}$/CoO Bilayers," Physical Review Letters **79**, 1130 (1997).

[125] K. Takano, R. H. Kodama, A. E. Berkowitz, W. Cao, and G. Thomas, "Role of interfacial uncompensated antiferromagnetic spins in unidirectional anisotropy in $Ni_{81}Fe_{19}$/CoO bilayers (invited)," Journal of Applied Physics **83**, 6888 (1998).

[126] N. Gökemeijer, R. Penn, D. Veblen, and C. Chien, "Exchange coupling in epitaxial CoO/NiFe bilayers with compensated and uncompensated interfacial spin structures," Physical Review B **63**, 174422 (2001).

[127] S. M. Zhou, S. J. Yuan, and L. Sun, "Intrinsic perpendicular anisotropy and exchange biasing in CoO/permalloy multilayers," in *Journal of Magnetism and Magnetic Materials*, Vol. 286 (2005) pp. 211–215.

[128] K. W. Lin, F. T. Lin, Y. M. Tzeng, and Z. Y. Guo, "Structural and magnetic properties of ion-beam deposited NiFe/Co-oxide bilayers," European Physical Journal B **45**, 237 (2005).

[129] J. van Lierop, B. W. Southern, K.-W. Lin, Z.-Y. Guo, C. L. Harland, R. A. Rosenberg, and J. W. Freeland, "Exchange bias in a columnar nanocrystalline $ni_{80}fe_{20}$CoO thin film," Physical Review B **76**, 224432 (2007).

[130] G. Kresse and J. Hafner, "Ab initio molecular dynamics for liquid metals," Physical Review B **47**, 558 (1993).

[131] G. Kresse and J. Furthmüller, "Efficiency of ab-initio total energy calculations for metals and semiconductors using a plane-wave basis set," Computational Materials Science **6**, 15 (1996), arXiv:0927-0256(96)00008 [10.1016] .

[132] G. Kresse and D. Joubert, "From ultrasoft pseudopotentials to the projector augmented-wave method," Physical Review B **59**, 11 (1999).

[133] P. E. Blöchl, "Projector augmented-wave method," Physical Review B **50**, 953 (1994).

[134] V. I. Anisimov, J. Zaanen, and O. K. Andersen, "Band theory and Mott insulators: Hubbard U instead of Stoner I," Physical Review B **44**, 943 (1991).

[135] V. I. Anisimov, I. V. Solovyev, and M. A. Korotin, "Density-functional theory and NiO photoemission spectra," Physical Review B **48**, 929 (1993).

[136] S. L. Dudarev, G. A. Botton, and S. Y. Savrasov, "Electron-energy-loss spectra and the structural stability of nickel oxide: An LSDA+ U study," Physical Review B **57**, 1505 (1998).

[137] F. Tran, P. Blaha, K. Schwarz, and P. Novák, "Hybrid exchange-correlation energy functionals for strongly correlated electrons: Applications to transition-metal monoxides," Physical Review B **74**, 155108 (2006).

[138] W. Jauch and M. Reehuis, "Electron density distribution in paramagnetic and antiferromagnetic CoO: A γ-ray diffraction study," Physical Review B **65**, 125111 (2002).

[139] W. Jauch, M. Reehuis, H. Bleif, F. Kubanek, and P. Pattison, "Crystallographic symmetry and magnetic structure of CoO," Physical Review B **64**, 052102 (2001).

[140] W. H. Meiklejohn and C. P. Bean, "New magnetic anisotropy," Physical Review **102**, 1413 (1956).

[141] S. Grytsyuk, M. V. Peskov, and U. Schwingenschlögl, "First-principles modeling of interfaces between solids with large lattice mismatch: The prototypical CoO(111)/Ni(111) interface," Physical Review B **86**, 174115 (2012).

[142] G. Kresse and J. Furthmüller, "Efficient iterative schemes for ab initio total-energy calculations using a plane-wave basis set," Physical Review B **54**, 169 (1996).

[143] O. Bengone, M. Alouani, P. Blöchl, and J. Hugel, "Implementation of the projector augmented-wave LDA+ U method: Application to the electronic structure of NiO," Physical Review B **62**, 392 (2000).

[144] N. J. Mosey, P. Liao, and E. A. Carter, "Rotationally invariant ab initio evaluation of Coulomb and exchange parameters for DFT+U calculations." The Journal of chemical physics **129**, 014103 (2008).

[145] U. Wdowik and K. Parlinski, "Lattice dynamics of cobalt-deficient CoO from first principles," Physical Review B **78**, 224114 (2008).

[146] S. Kwon and B. Min, "Unquenched large orbital magnetic moment in NiO," Physical Review B **62**, 73 (2000).

[147] S. A. Gramsch, "Structure, metal-insulator transitions, and magnetic properties of FeO at high pressures," American Mineralogist **88**, 257 (2003).

[148] P. Xu, K. Xia, C. Gu, L. Tang, H. Yang, and J. Li, "An all-metallic logic gate based on current-driven domain wall motion." Nature nanotechnology **3**, 97 (2008).

[149] S. Sao-Joao, S. Giorgio, J. M. Penisson, C. Chapon, S. Bourgeois, and C. Henry, "Structure and deformations of Pd-Ni core-shell nanoparticles," Journal of Physical Chemistry B **109**, 342 (2005).

[150] J. Zhang, F. H. B. Lima, M. H. Shao, K. Sasaki, J. X. Wang, J. Hanson, and R. R. Adzic, "Platinum monolayer on nonnoble metal-noble metal core-shell nanoparticle electrocatalysts for O 2 reduction," Journal of Physical Chemistry B **109**, 22701 (2005).

[151] Z. Xu, Y. Hou, and S. Sun, "Magnetic core/shell Fe_3O_4/Au and Fe_3O_4/Au/Ag nanoparticles with tunable plasmonic properties," Journal of the American Chemical Society **129**, 8698 (2007).

[152] F. Bao, J. F. Li, B. Ren, J. L. Yao, R. A. Gu, and Z. Q. Tian, "Synthesis and Characterization of Au/Co and Au/Ni Core-Shell Nanoparticles and Their Applications in Surface-Enhanced Raman Spectroscopy," Journal of Physical Chemistry C **112**, 345 (2008).

[153] E. Lundgren, B. Stanka, M. Schmid, and P. Varga, "Thin films of Co on Pt(111): Strain relaxation and growth," Physical Review B **62**, 2843 (2000).

[154] F. Meier, K. von Bergmann, P. Ferriani, J. Wiebe, M. Bode, K. Hashimoto, S. Heinze, and R. Wiesendanger, "Spin-dependent electronic and magnetic properties of co nanostructures on Pt(111) studied by spin-resolved scanning tunneling spectroscopy," Physical Review B **74**, 195411 (2006).

[155] S. Grytsyuk and U. Schwingenschlögl, "First-principles modeling of magnetic misfit interfaces," Physical Review B **88**, 165414 (2013).

[156] M. Ayadi, R. Belhi, N. Mliki, K. Abdelmoula, J. Ferré, and J. P. Jamet, "Face centered cubic cobalt layer on Au(111): a magneto-optical study," Journal of Magnetism and Magnetic Materials **247**, 215 (2002).

[157] J. Tersoff, "Surface-confined alloy formation in immiscible systems," Physical Review Letters **74**, 434 (1995).

[158] G. H. O. Daalderop, P. J. Kelly, and M. F. H. Schuurmans, "First-principles calculation of the magnetocrystalline anisotropy energy of iron, cobalt, and nickel," Physical Review B **41**, 11919 (1990).

[159] G. H. O. Daalderop, P. J. Kelly, and M. F. H. Schuurmans, "Magnetocrystalline anisotropy and orbital moments in transition-metal compounds," Physical Review B **44**, 54 (1991).

[160] G. H. O. Daalderop, P. J. Kelly, and M. F. H. Schuurmans, "Magnetic anisotropy of a free-standing Co monolayer and of multilayers which contain Co monolayers," Physical Review B **50**, 9989 (1994).

[161] J. Stöhr, "Exploring the microscopic origin of magnetic anisotropies with X-ray magnetic circular dichroism (XMCD) spectroscopy," Journal of Magnetism and Magnetic Materials **200**, 470 (1999).

[162] D. S. Wang, R. Wu, and A. J. Freeman, "Magnetocrystalline anisotropy of interfaces: first-principles theory for Co-Cu interface and interpretation by an effective ligand interaction model," Journal of Magnetism and Magnetic Materials **129**, 237 (1994).

[163] D. Weller, J. Stöhr, R. Nakajima, A. Carl, M. Samant, C. Chappert, R. Mégy, P. Beauvillain, P. Veillet, and G. Held, "Microscopic Origin of Magnetic Anisotropy in Au/Co/Au Probed with X-Ray Magnetic Circular Dichroism," Physical Review Letters **75**, 3752 (1995).

[164] T. Seki, S. Mitani, K. Yakushiji, and K. Takanashi, "Spin-polarized current-induced magnetization reversal in perpendicularly magnetized L10-FePt layers," Applied Physics Letters **88**, 22 (2006).

[165] B. Rodmacq, A. Manchon, C. Ducruet, S. Auffret, and B. Dieny, "Influence of thermal annealing on the perpendicular magnetic anisotropy of Pt/Co/AlOx trilayers," Physical Review B - Condensed Matter and Materials Physics **79**, 1 (2009).

[166] J. M. Shaw, H. T. Nembach, and T. J. Silva, "Measurement of orbital asymmetry and strain in $Co_{90}Fe_{10}$/Ni multilayers and alloys: Origins of perpendicular anisotropy," Physical Review B **87**, 054416 (2013).

[167] A. Manchon, H. C. Koo, J. Nitta, S. M. Frolov, and R. A. Duine, "New perspectives for Rashba spin-orbit coupling," Nature Materials **14**, 871 (2015).

[168] N. Nakajima, T. Koide, T. Shidara, H. Miyauchi, H. Fukutani, A. Fujimori, K. Iio, T. Katayama, M. Nývlt, and Y. Suzuki, "Perpendicular magnetic anisotropy caused by interfacial hybridization via enhanced orbital moment in Co/Pt multilayers: Magnetic circular x-ray dichroism study," Physical Review Letters **81**, 5229 (1998).

[169] I. E. Dzyaloshinskii, "Thermodynamic Theory of "Weak" Ferromagnetism In Antiferromagnetic Substances," Sov. Phys. JETP **5**, 1259 (1957).

[170] T. Moriya, "Theory of magnetism of NiF2," Physical Review **117**, 635 (1960).

[171] M. Bode, E. Y. Vedmedenko, von B. K., A. Kubetzka, P. Ferriani, S. Heinze, and R. Wiesendanger, "Atomic spin structure of antiferromagnetic domain walls," Nature Materials **5**, 477 (2006).

[172] M. Bode, S. Krause, L. Berbil-Bautista, S. Heinze, and R. Wiesendanger, "On the preparation and electronic properties of clean W(110) surfaces," Surface Science **601**, 3308 (2007).

[173] P. Ferriani, K. von Bergmann, E. Y. Vedmedenko, S. Heinze, M. Bode, M. Heide, G. Bihlmayer, S. Blügel, and R. Wiesendanger, "Atomic-Scale Spin Spiral with a Unique Rotational Sense: Mn Monolayer on W(001)," Physical Review Letters **101**, 027201 (2008).

[174] M. Heide, G. Bihlmayer, and S. Blügel, "Dzyaloshinskii-moriya interaction accounting for the orientation of magnetic domains in ultrathin films: Fe/w(110)," Physical Review B **78**, 140403 (2008).

[175] F. Schubert, Y. Mokrousov, P. Ferriani, and S. Heinze, "Noncollinear magnetism in freestanding and supported monatomic mn chains," Physical Review B **83**, 165442 (2011).

[176] S. Heinze, von B. K., M. Menzel, J. Brede, A. Kubetzka, R. Wiesendanger, G. Bihlmayer, and S. Blugel, "Spontaneous atomic-scale magnetic skyrmion lattice in two dimensions," Nature Physics **7**, 713 (2011).

[177] G. Chen, J. Zhu, A. Quesada, J. Li, A. T. N'Diaye, Y. Huo, T. P. Ma, Y. Chen, H. Y. Kwon, C. Won, Z. Q. Qiu, A. K. Schmid, and Y. Z. Wu, "Novel chiral magnetic domain wall structure in Fe/Ni/Cu(001) Films," Physical Review Letters **110**, 1 (2013).

[178] G. Chen, T. Ma, A. T. NDiaye, H. Kwon, C. Won, Y. Wu, and A. K. Schmid, "Tailoring the chirality of magnetic domain walls by interface engineering," Nature Communications **4** (2013).

[179] A. Thiaville, S. Rohart, É. Jué, V. Cros, and A. Fert, "Dynamics of Dzyaloshinskii domain walls in ultrathin magnetic films," Europhysics Letters **100**, 57002 (2012).

[180] K. Ryu, L. Thomas, S. Yang, and S. Parkin, "Chiral spin torque at magnetic domain walls," Nature Nanotechnology **8**, 527 (2013).

[181] A. Brataas and K. M. D. Hals, "Spin-orbit torques in action," Nature Nanotechnology **9**, 86 (2014).

[182] A. Manchon, "Spin-orbitronics: A new moment for Berry," Nature Physics **10**, 340 (2014).

[183] B. A. Bernevig and O. Vafek, "Piezo-magnetoelectric effects in p-doped semiconductors," Physical Review B **72**, 033203 (2005).

[184] K. Obata and G. Tatara, "Current-induced domain wall motion in rashba spin-orbit system," Physical Review B **77**, 214429 (2008).

[185] A. Manchon and S. Zhang, "Theory of nonequilibrium intrinsic spin torque in a single nanomagnet," Physical Review B **78**, 212405 (2008).

[186] I. Garate and A. H. MacDonald, "Influence of a transport current on magnetic anisotropy in gyrotropic ferromagnets," Physical Review B **80**, 134403 (2009).

[187] X. Wang and A. Manchon, "Diffusive spin dynamics in ferromagnetic thin films with a rashba interaction," Physical Review Letters **108**, 117201 (2012).

[188] E. Bijl and R. A. Duine, "Current-induced torques in textured rashba ferromagnets," Physical Review B **86**, 094406 (2012).

[189] K. Kim, S. Seo, J. Ryu, K. Lee, and H. W. Lee, "Magnetization dynamics induced by in-plane currents in ultrathin magnetic nanostructures with rashba spin-orbit coupling," Physical Review B **85**, 180404 (2012).

[190] D. A. Pesin and A. H. MacDonald, "Quantum kinetic theory of current-induced torques in rashba ferromagnets," Physical Review B **86**, 014416 (2012).

[191] K. M. D. Hals and A. Brataas, "Phenomenology of current-induced spin-orbit torques," Physical Review B **88**, 085423 (2013).

[192] P. C. Ortiz, X. Wang, M. Chshiev, and A. Manchon, "Angular dependence and symmetry of Rashba spin torque in ferromagnetic heterostructures," Applied Physics Letters **102**, 252403 (2013).

[193] D. Li, A. Smogunov, and C. Barreteau, "Magnetocrystalline anisotropy energy of Fe (001) and Fe (110) slabs and nanoclusters: A detailed local analysis within a tight-binding model," Physical Review B **88**, 214413 (2013).

[194] P. M. Haney, H. Lee, K. Lee, A. Manchon, and M. D. Stiles, "Current induced torques and interfacial spin-orbit coupling: Semiclassical modeling," Physical Review B **87**, 174411 (2013).

[195] F. Freimuth, S. Blügel, and Y. Mokrousov, "Spin-orbit torques in Co/Pt(111) and Mn/W(001) magnetic bilayers from first principles," Physical Review B **90**, 174423 (2014).

[196] G. Géranton, F. Freimuth, S. Blügel, and Y. Mokrousov, "Spin-orbit torques in $l1_0 - \mathrm{FePt/Pt}$ thin films driven by electrical and thermal currents," Physical Review B **91**, 014417 (2015).

[197] I. M. Miron, K. Garello, G. Gaudin, P. Zermatten, M. V. Costache, S. Auffret, S. Bandiera, B. Rodmacq, A. Schuhl, and P. Gambardella, "Perpendicular switching of a single ferromagnetic layer induced by in-plane current injection," Nature **476**, 189 (2011).

[198] L. Liu, O. J. Lee, T. J. Gudmundsen, D. C. Ralph, and R. A. Buhrman, "Current-induced switching of perpendicularly magnetized magnetic layers using spin torque from the spin hall effect," Physical Review Letters **109**, 096602 (2012).

[199] L. Liu, T. Moriyama, D. C. Ralph, and R. A. Buhrman, "Spin-torque ferromagnetic resonance induced by the spin hall effect," Physical Review Letters **106**, 036601 (2011).

[200] M. Jamali, K. Narayanapillai, X. Qiu, L. M. Loong, A. Manchon, and H. Yang, "Spin-orbit torques in co/pd multilayer nanowires," Physical Review Letters **111**, 246602 (2013).

[201] J. Kim, J. Sinha, M. Hayashi, M. Yamanouchi, S. Fukami, T. Suzuki, S. Mitani, and H. Ohno, "Layer thickness dependence of the current-induced effective field vector in Ta—CoFeB—MgO," Nature Materials **12**, 240 (2013).

[202] X. Fan, J. Wu, Y. Chen, M. J. Jerry, H. Zhang, and J. Q. Xiao, "Observation of the nonlocal spin-orbital effective field," Nature Communications **4**, 1799 (2013).

[203] K. Garello, I. M. Miron, C. O. Avci, F. Freimuth, Y. Mokrousov, S. Blugel, S. Auffret, O. Boulle, G. Gaudin, and P. Gambardella, "Symmetry and magnitude of spin-orbit torques in ferromagnetic heterostructures," Nature Nanotechnology **8**, 587 (2013).

[204] H. Kurebayashi, J. Sinova, D. Fang, A. C. Irvine, T. D. Skinner, J. Wunderlich, V. Novak, R. P. Campion, B. L. Gallagher, E. K. Vehstedt, L. P. Zarbo,

K. Vyborny, F. A. J., and T. Jungwirth, "An antidamping spin-orbit torque originating from the Berry curvature," Nature Nanotechnology **9**, 211 (2014).

[205] A. R. Mellnik, J. S. Lee, A. Richardella, J. L. Grab, P. J. Mintun, M. H. Fischer, A. Vaezi, A. Manchon, E. A. Kim, N. Samarth, and D. C. Ralph, "Spin-transfer torque generated by a topological insulator," Nature **511**, 449 (2014).

[206] Y. Fan, P. Upadhyaya, X. Kou, M. Lang, S. Takei, Z. Wang, J. Tang, L. He, L. Chang, M. Montazeri, G. Yu, W. Jiang, T. Nie, R. N. Schwartz, Y. Tserkovnyak, and K. L. Wang, "Magnetization switching through giant spinorbit torque in a magnetically doped topological insulator heterostructure," Nature Materials **13**, 699 (2014).

[207] G. Bihlmayer, S. Blügel, and E. Chulkov, "Enhanced Rashba spin-orbit splitting in BiAg(111) and PbAg(111) surface alloys from first principles," Physical Review B **75**, 195414 (2007).

[208] H. Bentmann, T. Kuzumaki, G. Bihlmayer, S. Blügel, E. V. Chulkov, F. Reinert, and K. Sakamoto, "Spin orientation and sign of the Rashba splitting in Bi/Cu(111)," Physical Review B **84**, 115426 (2011).

[209] M. Montalti, A. Credi, L. Prodi, and M. Gandolfi, *Handbook of Photochemistry, Third Edition* (CRC Press, 2006).

[210] S. Bornemann, O. Šipr, S. Mankovsky, S. Polesya, J. B. Staunton, W. Wurth, H. Ebert, and J. Minár, "Trends in the magnetic properties of Fe, Co, and Ni clusters and monolayers on Ir(111), Pt(111), and Au(111)," Physical Review B **86**, 104436 (2012).

[211] O. Šipr, S. Bornemann, H. Ebert, S. Mankovsky, J. Vacká, and J. Minár, "Co monolayers and adatoms on Pd(100), Pd(111), and Pd(110): Anisotropy of magnetic properties," Physical Review B - Condensed Matter and Materials Physics **88**, 1 (2013).

[212] L. Szunyogh, B. Újfalussy, P. Bruno, and P. W., "Anomalous perpendicular magnetic anisotropy in a Co monolayer on Au(111)," Journal of Magnetism and Magnetic Materials **165**, 254 (1997), symposium E: Magnetic Ultrathin Films, Multilayers and Surfaces.

[213] E. E. Krasovskii, "Microscopic origin of the relativistic splitting of surface states," Physical Review B **90**, 115434 (2014), arXiv:arXiv:1310.6893v2 .

[214] J. C. R. Sánchez, L. Vila, G. Desfonds, S. Gambarelli, J. P. Attané, J. M. De Teresa, C. Magén, and A. Fert, "Spin-to-charge conversion using Rashba coupling at the interface between non-magnetic materials." Nature communications **4**, 2944 (2013).

[215] H. Meng, V. B. Naik, and R. Sbiaa, "Tuning of perpendicular exchange bias for magnetic memory applications," physica status solidi (a) **210**, 391 (2013).

[216] K. . Shanavas and S. Satpathy, "Electric Field Tuning of the Rashba Effect in the Polar Perovskite Structures," Physical Review Letters **112**, 086802 (2014).

[217] S. J. Gong, C. G. Duan, Y. Zhu, Z. Q. Zhu, and J. H. Chu, "Controlling Rashba spin splitting in Au(111) surface states through electric field," Physical Review B - Condensed Matter and Materials Physics **87**, 3 (2013).

[218] S. E. Barnes, J. Ieda, and S. Maekawa, "Rashba spin-orbit anisotropy and the electric field control of magnetism." Scientific reports **4**, 4105 (2014), arXiv:arXiv:1312.1021 .

[219] X. Marti, I. Fina, and T. Jungwirth, "Prospect for Antiferromagnetic Spintronics," Magnetics, IEEE Transactions on **51**, 1 (2015).

[220] A. B. Shick, S. Khmelevskyi, O. N. Mryasov, J. Wunderlich, and T. Jungwirth, "Spin-orbit coupling induced anisotropy effects in bimetallic antiferromagnets: A route towards antiferromagnetic spintronics," Physical Review B **81**, 212409 (2010).

[221] T. Jungwirth, X. Marti, P. Wadley, and J. Wunderlich, "Antiferromagnetic spintronics," arXiv , 1 (2015), arXiv:arXiv:1509.05296v1 .

[222] S. Fukami, C. Zhang, S. DuttaGupta, and H. Ohno, "Magnetization switching by spin-orbit torque in an antiferromagnet/ferromagnet bilayer system," Arxiv (2015), arXiv:1507.00888 .

[223] R. O. Cherifi, V. Ivanovskaya, L. C. Phillips, A. Zobelli, I. C. Infante, E. Jacquet, V. Garcia, S. Fusil, P. R. Briddon, N. Guiblin, A. Mougin, A. A. Ünal, F. Kronast, S. Valencia, B. Dkhil, A. Barthélémy, and M. Bibes, "Electric-field control of magnetic order above room temperature," Nature Materials **13**, 345 (2014).

[224] C. Chappert, A. Fert, and F. N. Van Dau, "The emergence of spin electronics in data storage." Nature materials **6**, 813 (2007).

[225] J. Iwasaki, M. Mochizuki, and N. Nagaosa, "Universal current-velocity relation of skyrmion motion in chiral magnets," Nature Communications **4**, 1463 (2013).

[226] A. Kundu and S. Zhang, "Dzyaloshinskii-moriya interaction mediated by spin-polarized band with rashba spin-orbit coupling," Physical Review B **92**, 094434 (2015).

[227] C. Herring and J. H. Van Vleck, "Exchange interactions among itinerant electrons," Physics Today **20**, 75 (1967).

[228] L. M. Sandratskii, "Energy Band Structure Calculations for Crystals with Spiral Magnetic Structure," Physica Status Solidi B **136**, 167 (1986).

[229] L. M. Sandratskii, "Symmetry analysis of electronic states for crystals with spiral magnetic order. I. General properties," Journal of Physics: Condensed Matter **3**, 8565 (1991).

Papers Published, Submitted, and Under Preparation

- **S. Grytsyuk**, F. Cossu, and U. Schwingenschlögl, "Magnetic exchange at realistic CoO/Ni interfaces," The European Physical Journal B **85**, 254 (2012).
- **S. Grytsyuk**, M. V. Peskov, and U. Schwingenschlögl, "First-principles modeling of interfaces between solids with large lattice mismatch: The prototypical CoO(111)/Ni(111) interface," Physical Review B **86**, 174115 (2012).
- **S. Grytsyuk** and U. Schwingenschlögl, "First-principles modeling of magnetic misfit interfaces," Physical Review B **88**, 165414 (2013).
- **S. Grytsyuk** and U. Schwingenschlögl, "Mechanism of magnetization enhancement at CoO/permalloy interfaces," Applied Physics Letters **103**, 071603 (2013).
- **S. Grytsyuk**, A, Belabbes, P. M. Haney, H.-W. Lee, K.-J. Lee, M. D. Stiles, U. Schwingenschlögl, A. Manchon, "k-asymmetric spin-splitting at the interface between transition metal ferromagnets and heavy metals," *Submitted to Physical Review B.*
- **S. Grytsyuk** and U. Schwingenschlögl, "Magnetic anisotropy of the Au/Co interface," *Submitted to Physical Review B.*
- **S. Grytsyuk** and U. Schwingenschlögl, "Impact of lattice mismatch on the Rashba band splitting," *Submitted to New Journal of Physics.*

- **S. Grytsyuk** and U. Schwingenschlögl, "Impact of the interface potential on the Rashba band splitting," *To be submitted*.